



HAL
open science

Hybrid colloidal molecules from self-assembly of viral rod-like particles

Cheng Wu

► **To cite this version:**

Cheng Wu. Hybrid colloidal molecules from self-assembly of viral rod-like particles. Other [cond-mat.other]. Université de Bordeaux, 2018. English. NNT : 2018BORD0133 . tel-02938555

HAL Id: tel-02938555

<https://theses.hal.science/tel-02938555>

Submitted on 15 Sep 2020

HAL is a multi-disciplinary open access archive for the deposit and dissemination of scientific research documents, whether they are published or not. The documents may come from teaching and research institutions in France or abroad, or from public or private research centers.

L'archive ouverte pluridisciplinaire **HAL**, est destinée au dépôt et à la diffusion de documents scientifiques de niveau recherche, publiés ou non, émanant des établissements d'enseignement et de recherche français ou étrangers, des laboratoires publics ou privés.

Thèse présentée pour obtenir le grade de

Docteur de l'Université de Bordeaux

École Doctorale des Science Physique et de l'Ingénieur

Spécialité : Lasers, matière et nanosciences

Hybrid colloidal molecules from self-assembly of
viral rod-like particles

Par Cheng WU

Sous la direction de : Eric GRELET

Soutenue le 06 Septembre 2018

Membres du jury :

Président du jury : Cécile ZAKRI

M. Bertrand DONNIO
M. Clément NIZAK
M. Etienne DUGUET
Mme. Cécile ZAKRI

Directeur de Recherche, CNRS-IPCMS
Chargé de Recherche, CNRS-LBC
Professeur, Université de Bordeaux
Professeur, Université de Bordeaux

Rapporteur
Rapporteur
Examinateur
Examinateur

Centre de Recherche Paul Pascal (CRPP)

UMR5031, CNRS&Université de Bordeaux

115 Avenue du Dr Albert Schweitzer, 33600, PESSAC, France

Acknowledgments

It's been four whole years since I arrived in Bordeaux. When I got off the plane in Mérignac airport, I have no idea how it would be. I never expect that a PhD would challenge me so much, and neither would I image the self-fulfillment afterwards. As every candidate could experience, at a certain period of the PhD project, you could feel it is boring, tedious and full of difficulties, which of course also happened to me. Fortunately, there are wonderful persons around me who offer me a lot of help in my life and research. Also, I have met a lot of good friends to whom I can share my joy or sadness. Otherwise I could experience three times more difficulties and frustrations during these four years. Therefore I appreciate the help and accomplishment from all these persons, and special thanks to the following ones.

First, I'd like to thank my supervisor Eric Grelet for your invaluable guidance during these four years. I am very grateful for all the time and effort that you have dedicated to me and for all what you have taught scientifically. Without your feedback and help, this PhD would not have been possible. Once again thanks a lot to you. Even though I won't continue the academic research after the PhD, the methodology to obtain knowledge that I have lent from you are extreme useful in my future career. I wish you could not only achieve a great accomplishment in the soft matter field, but also cultivate large amount of talented young scientists

I sincerely thank my thesis committee Bertrand Donnio, Clément Nizak, Etienne Duguet and Cécile Zakri for your feedback and discussion before, during and after my defense. You have been critical and helpful, and I felt very comfortable sharing my research with all of you.

Also, I would like to thank the director, Cécile Zakri (again), and all the administrative staff in the CRPP, including Béatrice Dupin, Elizabeth Hortolland and Corinne Amengual and Nathalie Touzé. You have made all kinds of complicated paperwork well organized, which is very helpful for all the PhD candidates to focus on their research. Besides, thank you for being so nice and patient to me, a non-French spoken person.

During my research time in the lab, I got plenty of helps from my team. From the beginning, I understood almost nothing in the soft matter fields, Marie and Alexis shared with me their time and knowledge, which is especially important for me to begin the research in a

Acknowledgments

new field. Thanks also to those I work with—Laura, Andrii, Hanna, Baeckkyoung, and Lachlan—I really enjoy the time when we share the knowledge with each other. Hope you continuously enjoy your theoretical, experimental and coding study in the future.

I also thank those permanents who help me technically in my PhD research, Frédéric, Ahmed, Pascal, Sabrina, Joanna, Eric, Isabelle, and Sébastien. Especial thanks to Frédéric and Ahmed who help me a lot on finding chemicals or fixing the problems of experimental instruments (especially TEM), even though sometimes yourselves are busy. You are so nice person that are always willing to help others. Frédéric, I owe you so many times that I'm not able pay back completely.

Thanks to the all the Chinese companions in CRPP: 博思, 璇, 小青, 小舟, 晶泓, 等等. 感谢你们的陪伴, 让我在这四年的实验室生活里不孤单. 虽然此刻你们都已远去, 生活在不同的地方从事着不同的事业. 希望在将来我们还能再相遇, 并与彼此分享的新的快乐幸福或是悲伤.

I would like to also thank these friends out of my scientific world, with whom I spent lots of wonderful time. My roommates Yana, Xingyu and Yingying, thank you for enduring my shortcomings and help me to improve myself in the daily life. You are the best roommates forever! Thanks to Zhengyang, Bofang, Wen, Ruihao, Jie, Jinghua, whose I shared my happiness with, wish you always have it in your entire life.

Special thanks to my college roommate Fubao Wang (汪福宝) and “shijie” Yun Yang (杨云). Without your help I'm not even able to go broad. Even though we didn't connect with each other very often, you are always there in my mind. I really want to meet you when I go back to China, to thank your trust personally.

At last, I great thank to my families. To my parents, thanks for raising me up and supporting me all the time. Even though you have no idea what science or a PhD is like, but you love me with no conditions, which allow me to concentrate on my research without worrying about anything else. Thanks to my brother and sister for taking care of our parents for so many years as I'm not at home. I love you forever!

*"Il n'ya qu'un héroïsme au monde : c'est de voir le monde
tel qu'il est et de l'aimer."*

— *Romain Rolland*

Acknowledgments

Résumé

Dans cette thèse, l'auto-assemblage en molécules colloïdales de virus en forme de filament, les bactériophages M13, est étudié. Comme première approche, l'affinité de la streptavidine pour la biotine ou un *Strep-tag* est utilisée et quantitativement comparée. Pour ce faire, des virus modifiés génétiquement, M13-AS, présentant des *Strep-tag* et des virus M13C7C chimiquement bioconjugués par de la biotine ont réagi via leur extrémité proximale avec des nanoparticules fonctionnalisées par de la streptavidine. Il en résulte la formation de molécules colloïdales en étoile, dont la valence ou nombre de virus par structure, peut être simplement contrôlée par l'excès molaire initial. Cependant, la stabilité de ces molécules colloïdales est limitée par la libération progressive et la dégradation de la streptavidine. Nous avons alors développé une seconde approche basée sur l'affinité soufre-métal, qui s'est avérée à la fois pratique expérimentalement et fiable. Grâce aux groupements disulfures présents sur les cystéines de la protéine P3, des nanoparticules métalliques peuvent se lier à l'extrémité des virus. Le caractère générique de cette méthode est vérifié en faisant varier la nature du métal des nanoparticules ainsi que la souche des virus, dont la sauvage. La valence des structures formées est déterminée en fonction de plusieurs paramètres, dont l'excès molaire initial, la taille des nanoparticules et la force ionique. Un modèle rendant compte des résultats expérimentaux a été élaboré, dont les principales variables sont la surface des nanoparticules et le diamètre effectif électrostatique des virus. Cette approche est étendue à la réalisation de diblocs colloïdaux hétéro bifonctionnels, utilisant les virus comme briques constitutives. Comme preuve de concept, des diblocs bicolores à base de virus sont obtenus par auto-assemblage et leur dynamique est étudiée à l'échelle du bloc élémentaire en microscopie optique de fluorescence. Ainsi, nous avons montré dans cette thèse la réalisation par auto-assemblage d'une nouvelle génération de molécules colloïdales, dont l'auto-organisation peut conduire à la formation de superstructures hiérarchiques hybrides de complexité croissante, potentiellement utiles en sciences des matériaux.

Mots clés: Bactériophage, molécule colloïdale, auto-organisation, nanoparticule d'or, cystéine.

Summary

In this thesis, the self-assembly of rod-like viral particles, specifically the M13 bacteriophages, into colloidal molecules is studied. As the first method, the affinity of streptavidin to biotin or Strep-tag is used and quantitatively compared. In this case, both biologically engineered M13-AS displaying Strep-tags and chemically biotinylated M13C7C viruses have reacted with streptavidin activated nanoparticles via their functionalized proximal ends. This results in star-like colloidal molecules, whose valency – or number of viruses per structure – can be solely controlled by tuning the initial molar excess. However, the stability of these colloidal molecules is limited by streptavidin release and degradation. Thus, we develop the second method based on the sulfur—metal interactions, which is more convenient and reliable. Thanks to the exposed disulfide groups located at p3 proteins, metallic nanoparticles are able to bind to proximal ends of the M13 virus. The generic feature of this method is verified by using different metals and two virus strains including wt-M13. Afterwards, the control of the valency is explored by varying the initial molar excess, the nanoparticle size and the ionic strength. A quantitative model is built correspondingly, using the surface area of Au nanobead and the effective electrostatic diameter of the virus as variables, which accounts for the assembly of colloidal molecules with desired valencies. This method is further applied to assemble heterobifunctional diblocks by using filamentous viruses as building units. As a proof-of-concept experiment, bicolored diblocks are produced and tracked by each block simultaneously. Overall, we demonstrate the synthesis of a new generation of hybrid colloidal molecules, whose self-organization could serve as a promising means to create novel hierarchical biologic/inorganic superstructures that may find applications in materials science.

Keywords: Filamentous virus, bacteriophage, colloidal molecule, self-organization, gold nanoparticle, cysteine.

Contents

0	General introduction	1
0.1	Colloid, colloidal atoms and self-assembly/self-organization	2
0.2	Anisotropic colloidal atoms and patchiness	3
0.2.1	Shape-anisotropic colloidal atoms	4
0.2.2	Interaction-anisotropic colloidal atoms: patchy particles.....	5
0.3	From colloidal “atoms” to “molecules”	8
0.3.1	Clustering of isotropic colloidal spheres	8
0.3.2	Enthalpy driven self-assembly of patchy particles	9
0.3.3	Lock and key colloidal particles, driven by entropy	10
0.3.4	Combination of interaction and shape-anisotropy (entropy and enthalpy driven).....	11
0.4	Self-organization of colloidal atoms and molecules	11
0.4.1	Enthalpy driven self-organization.....	11
0.4.2	Entropy driven self-organization	13
0.5	Filamentous phages as a model system of rods	15
0.5.1	Model system for self-organization	16
0.5.2	Templates or scaffolds for nanomaterials synthesis	18
0.5.3	Building blocks for colloidal molecules	22
0.6	Outline of the thesis	22
0.7	References	25
1	Rod-like virus based multiarm colloidal molecules	33
1.1	Rod-like virus based multiarm colloidal molecules	34

2	Reduction of disulfide groups at proximal end of M13C7C viruses by TCEP/iTCEP and labeling with maleimide activated fluorescent dyes..	53
2.1	Introduction	54
2.2	Methods and results	56
2.2.1	TCEP as reductant	56
2.2.2	iTCEP as reductant	61
2.3	Conclusions	64
2.4	References	65
3	Introducing patchiness to the tip of rod-like viruses by grafting metallic nanoparticles.....	67
3.1	Introduction	68
3.2	Materials and Methods.....	69
3.3	Results and Discussion.....	74
3.3.1	Influence of M13 virus strains on the reaction with AuNBs.....	74
3.3.2	Improvement of the binding between M13 viruses and AuNBs by TCEP	77
3.3.3	Influence of metal species on the nanoparticle-M13 reaction.....	78
3.3.4	Roles of capping reagent and ionic strength on the reaction between M13C7C and AuNBs	81
3.3.5	Influence of molar excess on the reaction between M13C7C and AuNBs	87
3.4	Conclusions	88
3.5	References	88
4	Self-assembly of rod-like viruses into colloidal molecules with controlled valency.....	91
4.1	Introduction	92
4.2	Materials and Methods.....	93

4.3	Results and Discussion.....	95
4.3.1	Influence of ionic strength on the valency of self-assembled colloidal molecules.....	95
4.3.2	Influence of AuNB surface area on the valency of self-assembled colloidal molecules	98
4.3.3	Quantitative Model for the valency of colloidal molecules	99
4.3.4	Mass production of AB ₂ type colloidal molecules	103
4.4	Conclusions	105
4.5	References	105
5	Heterobifunctional colloidal diblocks from directional self-assembly of rod-shaped viruses	107
5.1	Introduction	108
5.2	Materials and Methods.....	110
5.2.1	Labeling of M13C7C viruses with red and green fluorescent dyes	110
5.2.2	Preparation of Scepter-like r-M13–AuNB colloidal molecules	111
5.2.3	Self-assembly of bicolored virus based diblocks	113
5.2.4	Diffusion coefficients and angle fluctuation of the diblocks.....	113
5.3	Results and Discussion.....	114
5.4	Conclusions	123
5.5	References	124
	Conclusion and perspectives	127
	Appendix I	135
	Appendix II.....	143

Chapter 0

General introduction

Contents

0.1	Colloid, colloidal atoms and self-assembly/self-organization	2
0.2	Anisotropic colloidal atoms and patchiness	3
0.2.1	Shape-anisotropic colloidal atoms	4
0.2.2	Interaction-anisotropic colloidal atoms: patchy particles	5
0.3	From colloidal “atoms” to “molecules”	8
0.3.1	Clustering of isotropic colloidal spheres	8
0.3.2	Enthalpy driven self-assembly of patchy particles	9
0.3.3	Lock and key colloidal particles, driven by entropy	10
0.3.4	Combination of interaction and shape-anisotropy (entropy and enthalpy driven).....	11
0.4	Self-organization of colloidal atoms and molecules	11
0.4.1	Enthalpy driven self-organization.....	11
0.4.2	Entropy driven self-organization	13
0.5	Filamentous phages as a model system of rods.....	15
0.5.1	Model system for self-organization	16
0.5.2	Templates or scaffolds for nanomaterials synthesis	18
0.5.3	Building blocks for colloidal molecules	22
0.6	Outline of the thesis	23
0.7	References	25

0.1 Colloid, colloidal atoms and self-assembly/self-organization

Colloid is a dispersion of microscopically insoluble particles suspended throughout another substance. The dispersed-phase particles have a diameter of a few nanometers to a few micrometers. Colloidal particles are often regarded as “big atoms” [1], owing to the structural similarities with atomic systems. They can be visualized directly by optical microscopy due to their relative large length scale. Therefore, these colloidal atoms serve as useful model systems for observing the microscopic mechanisms at single particle level. Using these well-characterized, classical particles, condensed matter problems have been investigated, such as dynamics of crystal melting [2], nucleation and growth of crystals [3] and phase transitions [4]–[6]. For example, colloidal rods can display different phases, such as nematic, smectic, columnar, and crystalline [7]–[9], which is the same as found in atomic and molecular systems. These fundamental physics governing that phenomenon can be used in more complex systems.

In addition, just like atoms are bricks of molecules or crystals, colloidal particles can be used to construct various structures, which hold profound technological implications [10], [11]. Bottom-up approach, especially self-assembly and/or self-organization of colloidal particles, is a cheap and convenient method to build hierarchical structures [12]–[20] which may find applications in, for example, photonic/plasmonic devices [16], nanoscale electronics [21], high efficiency energy-conversion/energy-storage [22], and hierarchically structured catalysts [23].

In order to better understand and describe the fabrication of different architectures by assembling colloidal particles, we first define several concepts that will be used in this thesis. In the literature, self-assembly and self-organization have both been used to depict a spontaneous formation process from discrete components to organized structures. In fact, the term self-assembly has been overused in different fields with different flavors. Here we distinguish these two concepts in the field of colloidal science and define them as different processes according to the obtained structures. Since the majority of the assembled colloidal architectures could be classified based on their degree of ordering, including ordered clusters of few colloidal particles which are called colloidal molecules and high ordered superlattices or arrays [24]–[26]. Thus, we define self-assembly for formation of colloidal molecules by elementary units (colloidal “atoms”), and specify self-organization for process to form ordered superlattices (arrays). Here, we also consider anisotropic colloidal particles, other than spheres, such as rods, cubes, triangles,

polyhedra, etc., as “colloidal atoms”, because they can also be used as elementary building blocks for the assembling colloidal molecules or superstructures. Overall, self-assembly is from colloidal atoms to colloidal molecules, while self-organization is for packing of colloidal atoms or colloidal molecules into ordered arrays or superstructures.

The interaction that drives the self-assembly and self-organization can be either “internal” between colloidal particles, like charge bond, hydrogen bond and hydrophobic interaction, or “external” like electronic and/or magnetic fields, templates, and agents. For the latter, it is also called *directed* assembly by Grzelczak [27]. Here we will not elaborate directed assembly, since in this thesis we will not deal with it.

0.2 Anisotropic colloidal atoms and patchiness

The isotropic colloidal spheres have been explored extensively for self-assembly and self-organization. The interests to use spheres in the fields of colloidal and nano-science can be attributed to three main aspects. First, the spheres are relatively easy to synthesize because minimization of the interfacial free energy strongly drives a particle to adopt such a shape [28]. Second, the colloidal spheres are literally big atoms [1], thus they are the ideal models for many condensed matter problems. Third, these colloidal spheres can easily self-organize into long-range ordered crystal lattice, which has promising application in optics, like photonic crystals [16], [29]–[31]. However, in contrast to atomic or molecular building blocks, whose binding is regulated by highly specific and directional interactions, isotropic colloidal spheres interact with each other by highly symmetric potentials (e.g., hard-core interaction, electrostatic interaction and van der Waals force). Therefore, the colloidal spheres can only form phases of simple symmetry, such as face-centered cubic (FCC), hexagonal close-packed (HCP) and body-centered cubic (BCC) [6], [32]–[34]. In this case, adding shape-, interaction-anisotropy or both to colloidal systems extends the possibility to attain more complex assembled architectures [35]–[37]. An enormous amount of works has been devoted to engineer colloidal building blocks with chemical and morphological anisotropy, trying to introduce selective and directional interactions, which will lead to an increase of the self-assembled or -organized architectural complexity.

0.2.1 Shape-anisotropic colloidal atoms

Creating a building block of an anisotropic shape can be achieved through two main routes, either by shaping spherical colloidal particles or by synthesizing directly the colloidal atoms of anisotropic shapes, like rods, cubes, triangles, octahedra, etc.

The lock colloidal particles are good examples of shaping colloidal spheres that can introduce directional interactions. (The mechanism of lock and key colloidal particles will be presented in 0.3.3.) Sacanna [38] et al. first created the lock colloidal particles with one dimple by polymerization reaction. Afterwards, three dimensional lock and key colloids were synthesized by Wang [39], through the hydrolytic removal of silica cluster templates from organo-silica hybrid patchy particles (Figure 1). (Clusters themselves can be considered as colloidal molecules, which will be discussed in Section 0.3.1). The geometry of the cavities stems from the originally assembled cluster templates, displaying well-defined three-dimensional symmetries, ranging from spherical, linear, triangular, tetrahedral, trigonal dipyramidal, octahedral, to pentagonal dipyramidal.

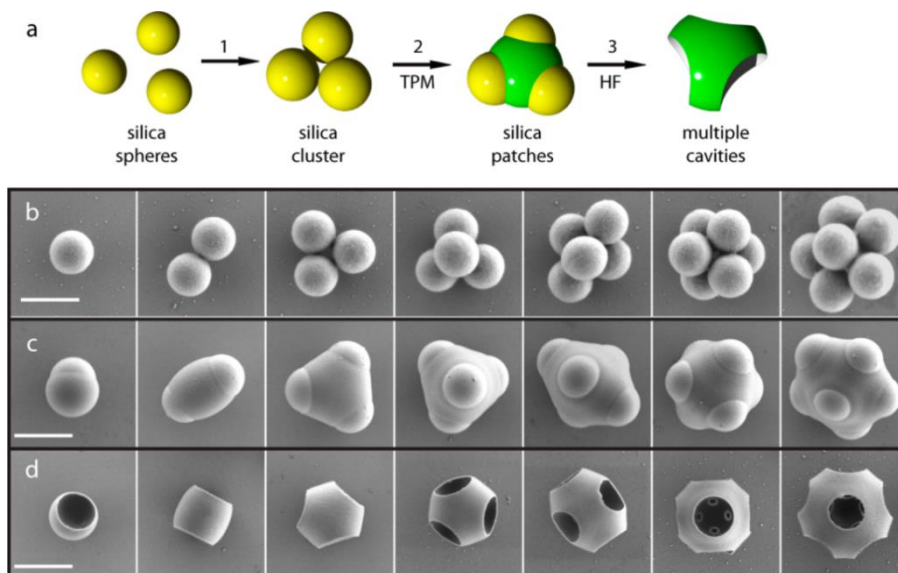


Figure 1: Fabrication of multicavity lock colloids [39]. (a) Scheme of the preparation of colloidal particles with multiple cavities having well-defined symmetries. A three-cavity particle is shown as an example. 1. A cluster of three silica spheres is prepared via an emulsion–encapsulation process. 2. Partial encapsulation of the cluster with 3-(trimethoxysilyl)propyl methacrylate (TPM). 3. Silica clusters are etched out via treatment with hydrofluoric acid. Electron micrographs of (b) silica clusters, (c) silica-TPM patchy particles, and (d) multicavity particles. Scale bars, 1 μm .

Synthesis of non-sphere based shape-anisotropic colloidal particles as another important method to increase the complexity also draws a lot of attractions. The most studied shape-anisotropic colloidal particles are ellipsoids and rods (fibers), since they are easy to synthesize and their assembled structures show great interests [40]–[42]. Different methods and materials have been developed to create rod-like colloidal particles. The most common used systems include silica rods and rod-like viral particles (e.g., tobacco mosaic viruses (TMV) and fd viruses). Numerous studies have reported the synthesis of silica rods at different length scales with various aspect ratios. However, the obtained silica rods normally show a broad size distribution, which hindered their applications. On the contrary, the rod-like viral particles show high monodispersity, because they are created by genetic replication. Therefore, the rod-like viruses have been widely used as a model system for investigating dynamics and phase transitions of colloidal liquid crystals [7], [43]–[47], as well as application in photoelectric materials [21], [48], [49]. There are also drawbacks for the biological system, as they are not colloidally stable in organic solvent and can be denatured at high temperatures.

Other shape-anisotropic colloidal atoms like cubes [50]–[52] and octahedral [53] are also prepared with different techniques. Since they are not the interest in this thesis, we will not introduce more details.

0.2.2 Interaction-anisotropic colloidal atoms: patchy particles

In addition to the shape-anisotropy, introducing interaction-anisotropy also improves the complexity of the assembled or organized colloidal architectures. The introduction of interaction-anisotropy to a colloidal particle is mainly achieved by heterogeneous chemical modification or patterning. The resulted colloidal particles, such as Janus particles, have been generally called patchy particles. Even though some literature include shape-anisotropic colloidal particles as entropically patchy particles [20], we refer patchy particles only to the enthalpically anisotropic ones. In order to have a precise control of the directed interaction between patchy particles to form a specific structure, Chen [54] proposed 5 parameters, including size, number, shape, position of patches, and patch–patch interactions determined by the surface chemical makeup of patches, as shown in Figure 2.

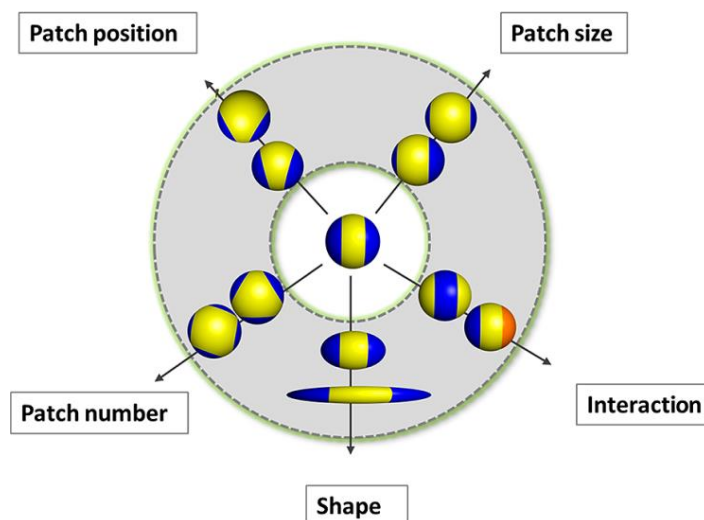


Figure 2: Various parameters to control the self-assembly of patchy colloids: size, number, shape, position of patches, and patch–patch interactions determined by the surface chemical makeup of patches. Illustrated here for spheres, ellipsoids, and needles (oblate spheroids), these parameters also generalize to other shapes such as rods, cubes, and other polyhedra [54].

Several experimental methods have been employed to synthesize sphere based patchy particles. The most commonly used one is vapor deposition onto a close-packed monolayer of colloids. This technique has been widely used to yield Janus particles [55]–[57]. When the vapor deposition is performed at an inclined angle with respect to the plane defined by the monolayer, the technique is called glancing-angle deposition (GLAD) [58]–[60]. In the GLAD technique, particles within the same monolayer act as shadow masks for neighboring particles. Thus, no separation of the shadow mask from the fabricated particles is required at the end of the preparation.

To create sphere based colloidal particles with several patches, the pre-clustered colloidal molecules are often used (Figure 3). The clusters of microspheres (Figure 3b) were first synthesized utilizing emulsion droplets as confined geometries [61], and then patchy particles were formed from the clusters using a two-stage swelling process followed by polymerization [62]. These colloidal particles, composed of amidinated polystyrene and bearing chemically distinct surface patches functionalized with DNA, imitate hybridized atomic orbitals including sp , sp^2 , sp^3 , sp^3d , sp^3d^2 and sp^3d^3 (Figure 3c). At the termini of the DNA are single-strand “sticky” ends, allowing these patchy colloidal atoms to form directional bonds through programmable, specific and reversible DNA interactions.

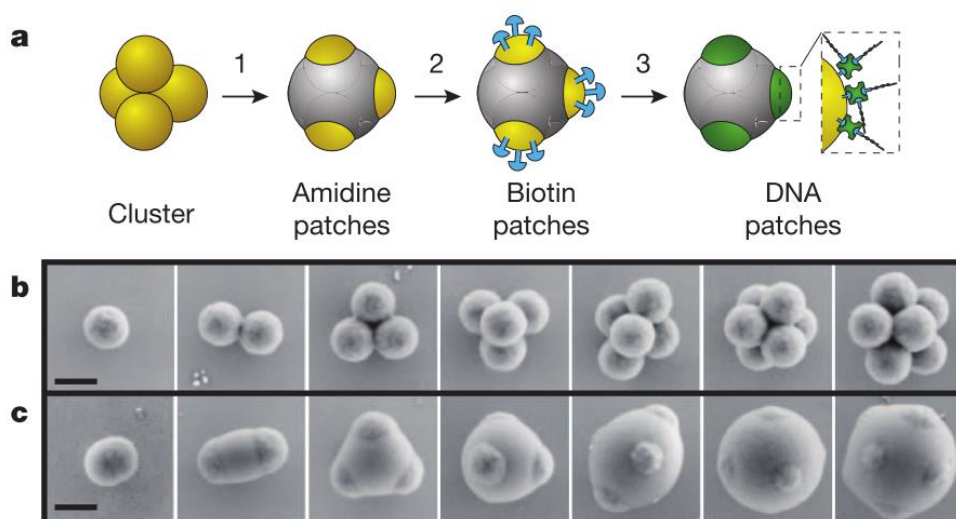


Figure 3: DNA patchy particle fabrication [61]. (a) Preparation of colloidal particles with DNA-functionalized patches having well-defined symmetries. A four-patch particle is shown as an example. (b) Electron micrographs of amidinated colloidal clusters, showing the particle configurations for clusters of $n = 1-7$ microspheres. (c) Electron micrographs of amidinated patchy particles after encapsulation. The patches inherit the symmetries of their parent clusters. Scale bars, 500 nm.

Compared to the large amount of works on sphere based colloidal patchy particles, less studies have focused on the non-sphere based patchy particles. Chaudhary [63] prepared matchstick-like patchy silica rods by coating their tips with a gold layer, as shown in Figure 4. To selectively coat only the rod tips, the particles were first vertically aligned and hexagonally close-packed by means of an electric field, followed by electron-beam coating of the exposed tips with a gold layer.

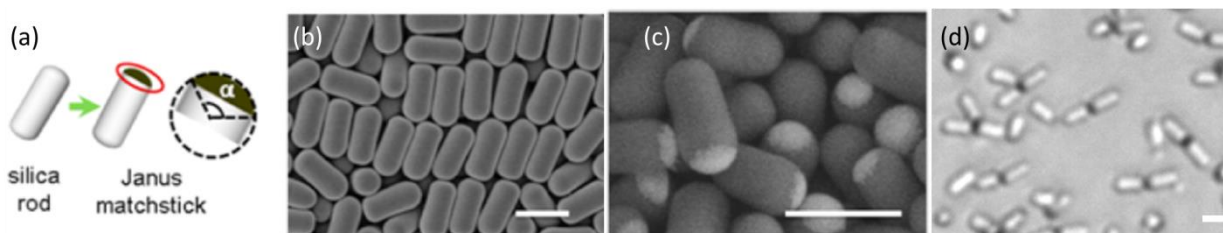


Figure 4: Schematic (a) and scanning electron microscopy (SEM) images of non-functionalized (b) and gold-tip-coated (c) silica rods. These tip coated rods can serve as patchy atoms and assemble into colloidal molecules (d) [63]. Scale bars, 2 μm .

Another example of rod-like patchy particle can be achieved by filamentous viruses. The exposed disulfide groups at one end of the viral particle can be employed to regio-selectively

conjugate with maleimide activated functional groups or metals. Like this, the reactive groups, like biotin, DNA, and metallic nanoparticles can be easily introduced to the end of viruses and serve as the patchiness. We will discuss more details in Section 0.5.

0.3 From colloidal “atoms” to “molecules”

Colloidal molecules as analogy of the small molecules have drawn a lot attentions [17], [25], [26], [34], [38], [64]–[68]. One of the most common and convenient way to create colloidal molecules is by clustering of colloidal spheres, as already mentioned in the previous section. In addition to the clustering of colloidal spheres, another important pathway is self-assembling either enthalpically patchy particles or entropically lock and key particles with directional interactions.

0.3.1 Clustering of isotropic colloidal spheres

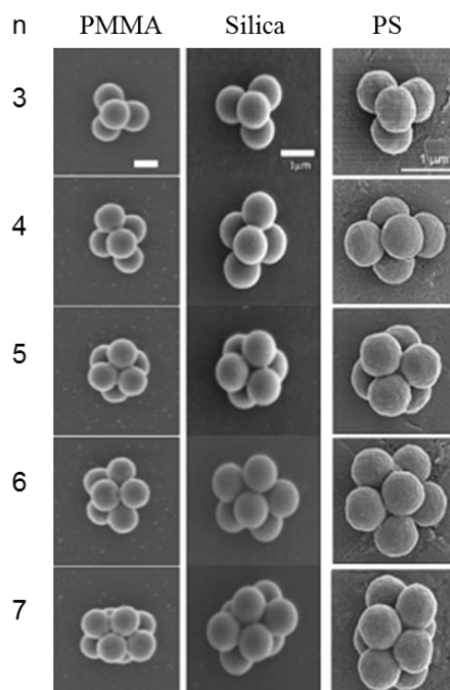


Figure 5: SEM images of poly(methyl methacrylate) (PMMA), silica and polystyrene (PS) colloidal clusters obtained via emulsion-evaporation method [69]. Numbers of spheres involved in the clusters are tuned by controlling the size of emulsion droplets. Scale bars, 1 μm .

Clustering of the colloidal spheres can be synthesized by introducing attractive interactions between colloidal spheres [70], [71]. Several kinds of assisted interactions have been reported,

such as van der Waals force, electrostatic interaction and chemical bonding [72]. In order to better control the number of spheres involved in the clusters, confinements are often used. For example, Manoharan et al. [62], [69] used emulsion droplets as confined geometries to contain polymer microspheres. The subsequent controlled removal of the liquid from the droplets generated compressive forces that draw the particles together. Therefore, clusters consisting of two to several polymer or silica colloidal particles have been achieved (Figure 5). But, the obtained clusters normally show a broad distribution of sphere number in the clusters, which often impeded the further application. Thus, a following centrifugation in a density gradient is often performed to separate the clusters with different sizes.

0.3.2 Enthalpy driven self-assembly of patchy particles

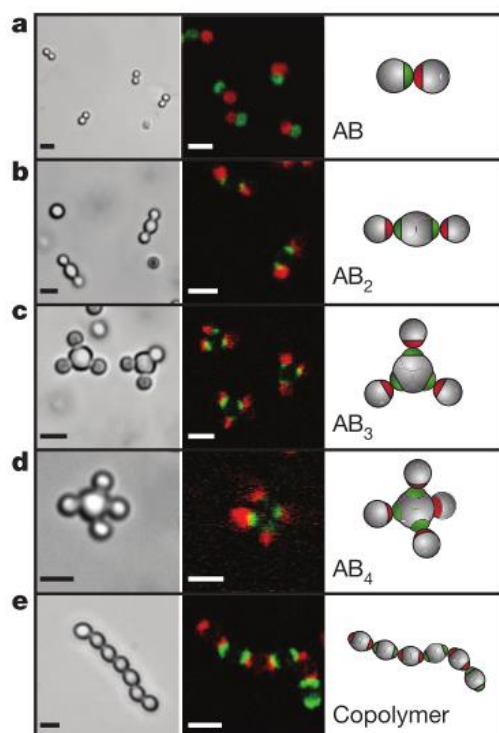


Figure 6: Specific directional bonding between colloidal atoms observed with optical microscopes [61]. (a)–(e) Bright-field (left panels), confocal fluorescent (middle panels), and schematic images (right panels), show colloidal molecules self-assembled from patchy particles. Scale bars, 2 μm .

Patchy particles with controlled directional interaction are employed increasingly as building units for assembling colloidal molecules. The enthalpy driven interactions between patchy particles can result into highly specific structures. Thus, design and assembly of patchy

particles are considered to be the most promising method for programmable fabrication of hierarchical architectures. For instance, colloidal particles with fixed number of patches (Figure 3) can be considered as colloidal atoms with a given valency. By adding these multivalent particles to a suspension of monovalent particles with a complementary DNA sequence, colloidal molecules of various valencies, including AB, AB₂, AB₃ and AB₄ types were formed, as shown in Figure 6a-d [61]. Colloidal copolymer was also prepared when complementary divalent particles were mixed (Figure 6e).

When the patchy rods are used as building blocks, colloidal molecules are assembled via their patchy tips. For example, the silica matchstick particles can assemble into multipod structures such as bipods, tripods and tetrapods via the van der Waals interaction between their gold coated tips (Figure 4d) [63].

0.3.3 Lock and key colloidal particles, driven by entropy

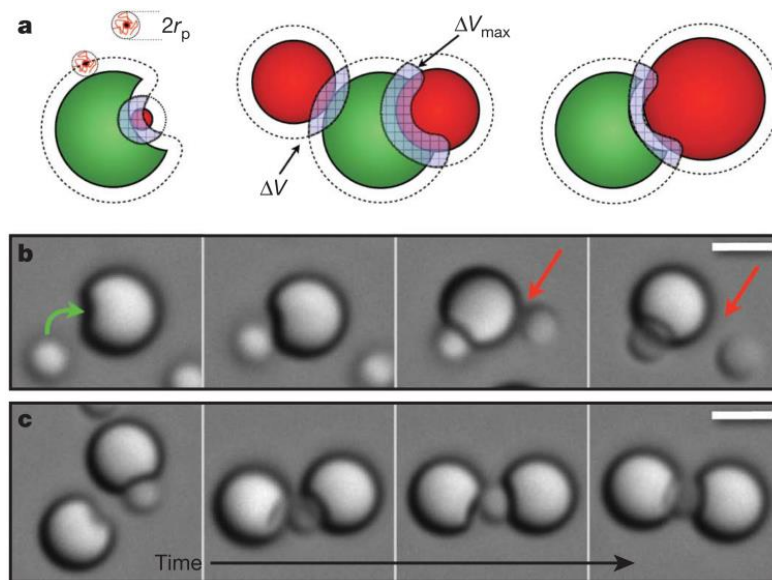


Figure 7: Lock–key interactions [38]. The depletion attraction potential between lock and key is proportional to the overlapping excluded volume ΔV , which attains a maximum ΔV_{max} for the configuration in which the key particle, by virtue of its size and position, precisely fits into the spherical cavity of a lock particle. For all other configurations, $\Delta V < \Delta V_{max}$. Because the depletion interaction is also proportional to the density of the polymer depletant, n_p , in solution, the interaction can be tuned by adjusting n_p so that it is sufficiently strong to bind two particles only for the lock–key–lock configuration.

In addition to assembling patchy particles, another way to fabricate colloidal molecules is matching shape-complementary colloidal particles by introducing entropy driven depletion attraction [73], [74]. Because the depletion interaction potential is proportional to the overlapping excluded volume between the particles, non-spherical colloids will experience different depletion forces depending on their mutual orientation. As shown in Figure 7, this feature was conveniently exploited to program the assembly of shape-complementary colloidal building blocks into ‘lock and key’ configuration that maximizes overlap volume ΔV [38]. The lack of covalent chemical bonds between the individual building blocks in the assembled clusters accounts for flexible junctions, mixed compositions and reversible interactions that can be conveniently controlled by changing the depletant concentration or, if a thermo-responsive depletant is used, by temperature.

0.3.4 Combination of interaction and shape-anisotropy (entropy and enthalpy driven)

Recent numerical studies have highlighted the potential interest of more sophisticated patchy particles in order to create new systems. In fact, combining both enthalpic and entropic patchiness provides opportunities for enhancing particular desired colloidal molecules of high complexity [20]. Hubert et al. [75] recently reported the synthesis of multivalent silica nanoparticles combining both enthalpic and entropic patchiness that could be used as promising building blocks to fabricate new supracolloids.

0.4 Self-organization of colloidal atoms and molecules

As we have defined, the self-organization refers to spontaneously formation of ordered superlattice or arrays. Both entropy and enthalpy can be used to drive colloidal particles (“atoms”) and colloidal molecules into these highly ordered arrays or hierarchical structures.

0.4.1 Enthalpy driven self-organization

Self-organization driven by enthalpy has been investigated by using patchy particles. Chen et al. [76] utilized triblock Janus particles (hydrophobic domains at the two poles) to self-organize into a complex colloidal kagome lattice, thanks to the electrostatic repulsion in the middle and the hydrophobic attraction at the poles (Figure 8a). When two different patches are

introduced to two poles of the colloidal spheres, more hierarchical structures can be formed through a two-step fabrication combining self-assembly and self-organization [17], [77] (Figure 8b). The patchy particles were first self-assembled into colloidal molecules as intermediates and then self-organized into a hierarchical network by stepwise change of the ionic strength of the medium.

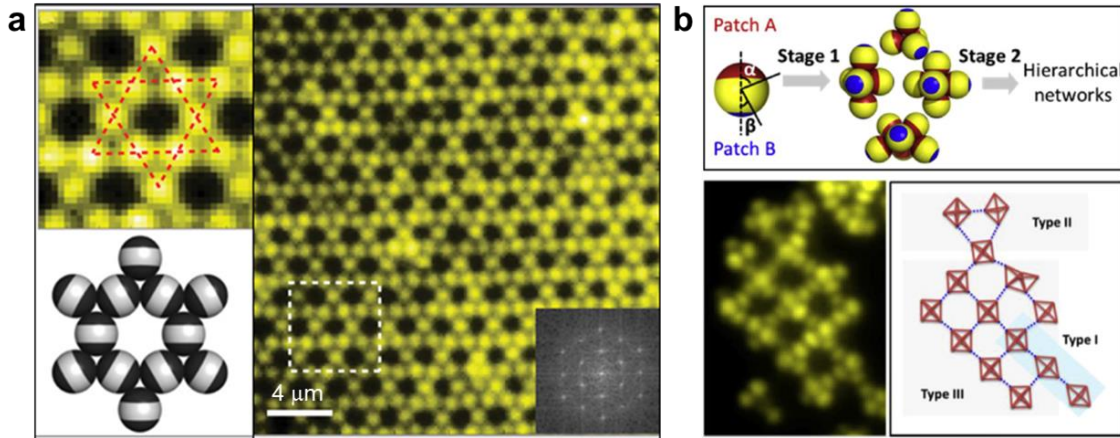


Figure 8: (a) Fluorescence image and a schematic illustration of a colloidal kagome lattice. Inserted on the bottom right is the fast Fourier transform image [76]. (b) On the top: Schematics of the staged self-assembly of triblock spheres with two different patches; On the Bottom: fluorescence image and schematics of a network of clusters comprising three types of bonds [77].

Hierarchical structures can also be obtained by enthalpic organization of patchy rods. Qiu et al. [78], [79] explored the synthesis and organization of amphiphilic cylindrical polar–hydrophobic–polar (P–H–P) or hydrophobic–polar–hydrophobic (H–P–H) triblocks (illustrations shown in Figure 9). A wide variety of superstructures are obtained through organization of the triblocks side by side or end to end in different solvents due to the hydrophobic or hydrophilic interaction. It offers opportunities to develop functional and robust micrometer-scale architectures with potential applications in various areas such as sensing, biomedicine, optoelectronics and photonic crystals.

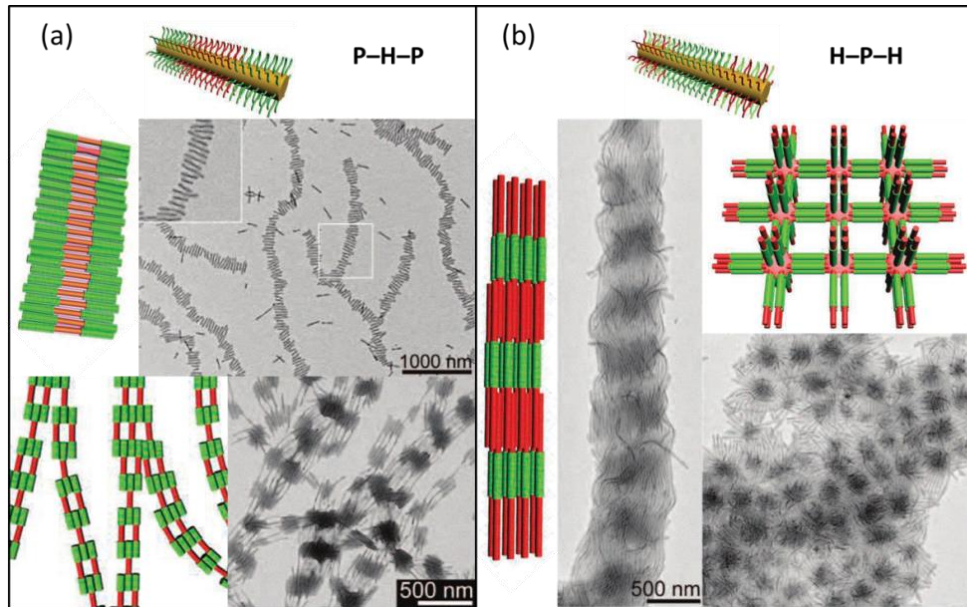


Figure 9: Illustrations and TEM images of self-organized amphiphilic triblock rods [78], [79]. Various hierarchical structures composing of polar–hydrophobic–polar (P–H–P) (a) or hydrophobic–polar–hydrophobic (H–P–H) triblocks (b) can be obtained by controlling the nature of the solvent.

Like-charge attraction induced by adding opposite charged multivalent ions into polyelectrolytes suspension, such as DNA segments and filamentous viruses, is another pathway to achieve enthalpic self-organization [80]–[86]. Prior studies have reported the cholesteric liquid crystalline phase formed by precipitating DNA fragments with spermine or spermidine [87]–[90]. Besides, filamentous viruses were also precipitated by like-charge attraction [91], [92], yet only bundle like structures were obtained.

0.4.2 Entropy driven self-organization

The entropy driven organization of isotropic or anisotropic colloidal particles is normally achieved by maximize the excluded volume in dense packing state. Monodisperse colloidal spheres in a suspension can spontaneously form close-packed colloidal crystal arrays if their concentration is restricted below a certain level [5], [6]. In order to obtain other more complex symmetry, the self-organizations of anisotropic colloidal atoms are investigated both theoretically and experimentally. Glotzer and her coworkers made predictions on packing of various anisotropic colloidal particles [20], [93], [94]. Meanwhile, they succeeded to self-organize polyhedra, such as rhombic dodecahedra, truncated cubes, octahedra and

tetrahexahedra, into superlattices with positional and orientational order in solution. Through entropy maximization, the shape-anisotropy of the building blocks can be exploited to program and regulate their organization: the shape of the particle determines the crystallographic symmetry of the resulting superlattice.

Colloidal rods as another class of anisotropic particles have drawn lots of attentions. They can self-organize into different liquid crystalline phases, like nematic, smectic and columnar [7], [40], [95], by increasing their volume fractions, as shown in Figure 10. This process is driven only by entropy.

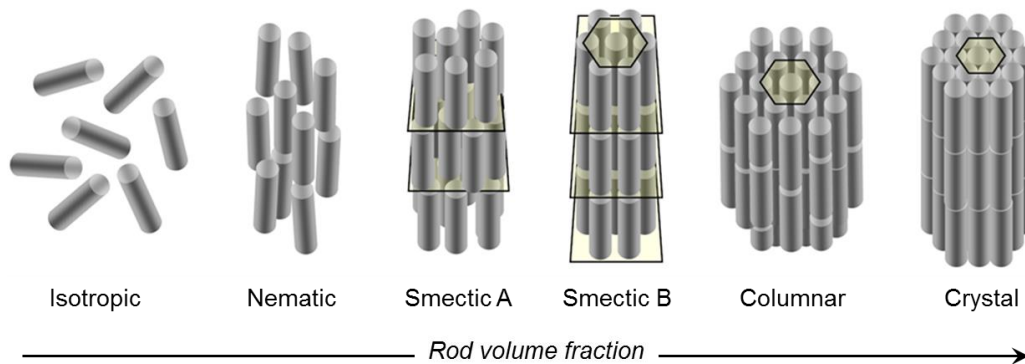


Figure 10: Schematic illustration of entropy driven self-organization of monodisperse colloidal rods into different phases. The nematic, smectic, columnar and crystalline phases can be formed by increasing the particle volume fraction from isotropic liquid phase.

Different packing symmetries can be achieved with more complex rods. For example, Yang et al. [96] synthesized monodisperse bent silica rods (BSRs) by controlled perturbation of emulsion-templated growth. The BSRs behave like banana-shaped molecules and can assemble into typical smectic phase when they are dense packed, as a result of the specific bent shape. Therefore, these BSRs could serve as a new visual model for understanding the physics in the phase behavior of banana-shaped liquid crystals.

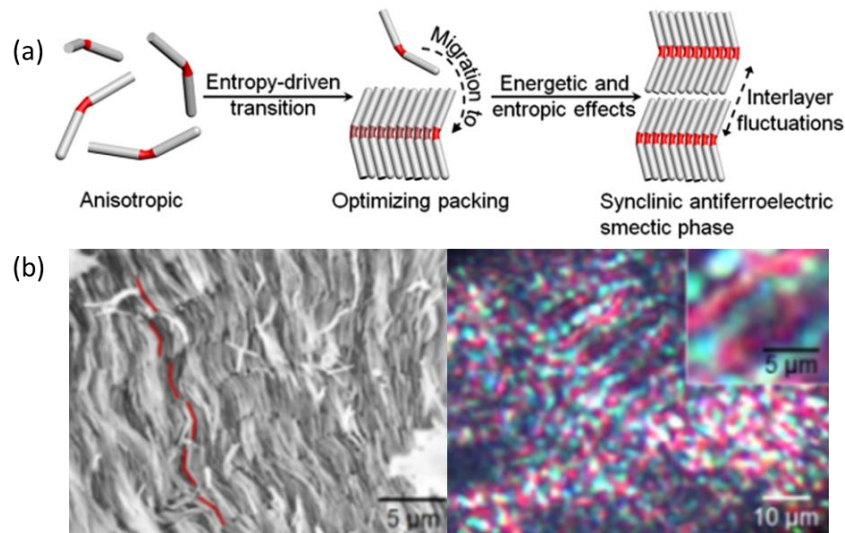


Figure 11: Assembly of bent silica rods (BSRs) into smectic phase. (a) Scheme of the BSRs self-organizing into smectic phase. (b) Scanning electron microscopy (SEM, left) and polarizing optical microscopy (POM, right) images of BSRs packed in smectic phase [96].

0.5 Filamentous phages as a model system of rods

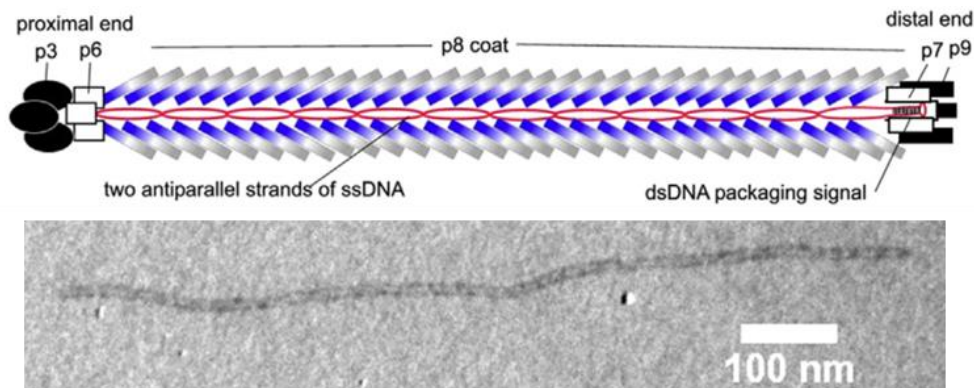


Figure 12: Up, Schematic representation of filamentous phage. Filamentous phage ($\sim 1 \mu\text{m}$ in length and $\sim 7 \text{ nm}$ in diameter) is a nanofiber-like virus composed of ~ 2700 highly ordered copies of major coat protein (p8) and 5 copies of the minor coat proteins (p3, p6, p7, and p9) surrounding a single-stranded circular DNA, which encodes all the coat proteins. The proximal p3/p6 adsorption complex is on the left of the scheme and the distal p7/p9 complex is on the right [97]. Down, TEM image of a fd virus after staining with uranyl acetate. The proximal and distal ends are not distinguishable in this TEM image.

Filamentous phage, a virus that specifically infects and replicates within bacterium *Escherichia coli*, is a rod-like biosupramacromolecule composed of a single-stranded circular

DNA molecule that is encapsulated in a long cylindrical protein coat [97]–[99]. The protein coat is composed of about 2800 copies of the major coat proteins (p8), and at both termini there are five copies of each of the two minor coat proteins: p7 and p9 at one end (distal), p3 and p6 at the other end (proximal), as shown in Figure 12.

The bacteriophage particles are about 7 nm in diameter and 1 μm in length. Two closely related stains, fd and M13, are genetically almost identical with coat proteins differing by only a single amino acid: negatively charged aspartate in fd (asp12) corresponding to neutral asparagine in M13 (asn12) [100]. As a result of this difference, M13 has one negative charge less per subunit than fd at physiological pH, corresponding to about 30% reduction in surface charge density. Besides, a mutant of M13, called M13C7C, fused with disulfide contained peptide at N-terminal of p3 protein has been used as template, scaffold and building block in different fields.

In the following sections, we present the main applications of the filamentous viruses in colloidal and materials science.

0.5.1 Model system for self-organization

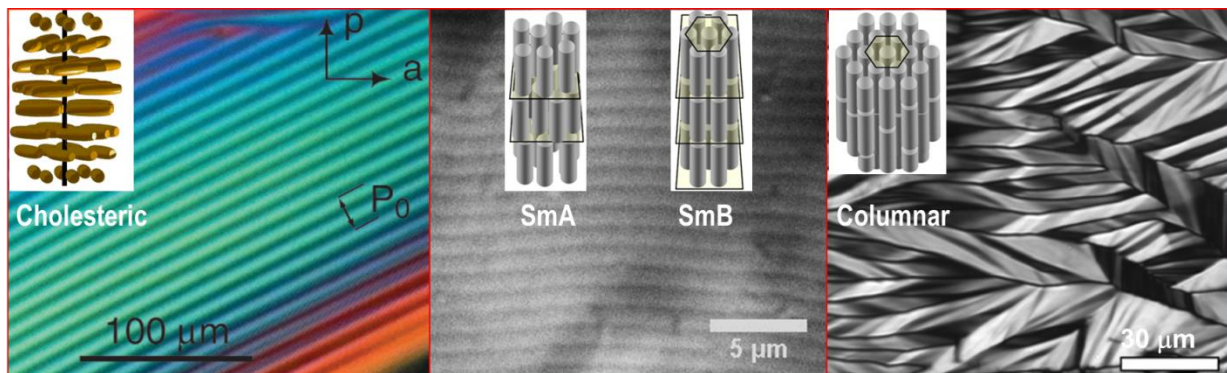


Figure 13: Left, polarizing microscopy image of a cholesteric liquid crystalline phase formed by fd viruses [101]. Middle, differential interference contrast (DIC) microscopy image of a smectic phase formed by M13 viruses. The smectic A (SmA) phase has liquid-like order within the layers while smectic B (SmB) phase shows hexagonal positional order. Right, optical texture of the columnar phase observed by polarizing microscopy [7]. Inserts are schematic representations.

The filamentous fd/M13 phages are widely used as model system of hard rods in colloidal liquid crystal science, due to three main features: first, the length of these viruses is about one

micron, which allows for their direct observation at the single particle level by optical microscopy; second, even though the viruses are highly charged (fd: $10 \text{ e}^-/\text{nm}$; M13: $7 \text{ e}^-/\text{nm}$), they can be approximated as hard rods with an effective diameter of viruses in an ionic aqueous solution; third, the viruses are created by replication, so the resulting viruses are identical in size and shape. Therefore, these highly monodisperse viruses self-organize into various liquid crystal phases in water, such as chiral nematic (cholesteric, Figure 13 left), smectic (including smectic A (SmA) and smectic B (SmB), Figure 13 middle), and columnar (Figure 13 right), driven only by entropy [7], [101]–[104].

Specifically, both SmA and SmB phases show the lamellar structure by optical microscopy, with particles normal to the layers. The order within the smectic layers is different between SmA and SmB phases: SmA has liquid-like order within the layers while SmB shows hexagonal positional order. Moreover, a hopping-like behavior of particles between the layers is observed in SmA phase [105], [106], using the technique of single particle tracking by fluorescence labeling, as presented in Figure 14. It demonstrates that the diffusion throughout the smectic layers takes place in quasiquantized steps of one rod length. In addition, dynamics of viral particles in nematic and columnar phase, as well as the guest-host system have also been also studied thanks to the particle tracking by fluorescence microscopy [43], [107], [108]. Detailed method of fluorescence labeling will be discussed in Section 0.5.2b.

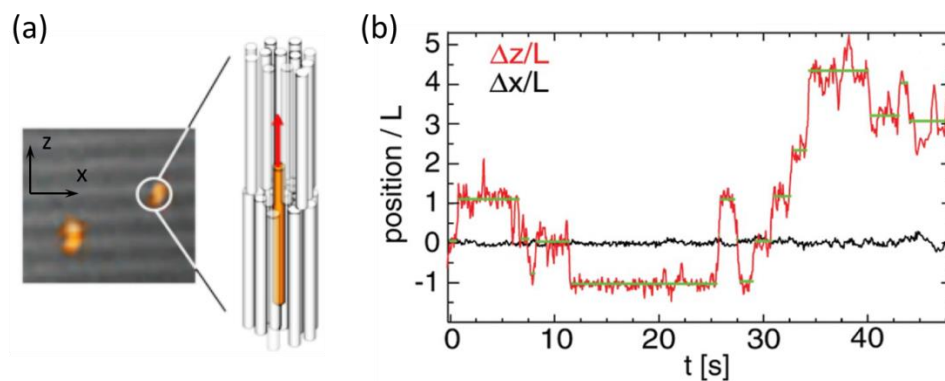


Figure 14: (a) Overlay of DIC and fluorescence images, and the corresponding schematic representation of a particle hopping between two smectic layers [106]. Only tracer amount of labeled viruses are mixed, with a ratio of $1: 10^5$. (b) Displacement of a given particle in the direction parallel (red) and perpendicular (black) to its director. The green lines indicate the residence time, i.e., the time for which one particle stays in a given layer.

Depletion is another method to entropically self-organize the filamentous viruses into ordered structures, which is achieved by adding non-absorbing polymers. The depletion force can be tuned by varying the polymer size and concentration. Consequently, different morphologies of self-organized viruses are obtained using PEG or Dextran as depletant, including membranes, platelets, smectic layers, as shown in Figure 15 [102], [109]–[112].

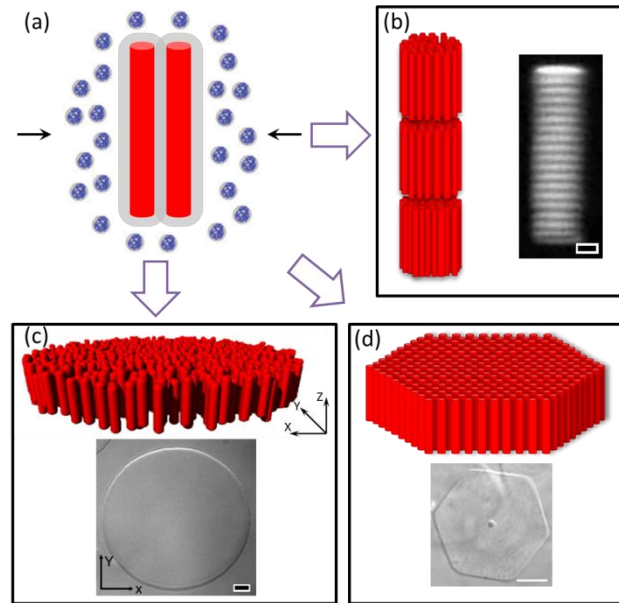


Figure 15: Depletion interactions induced by adding non-absorbing polymers organize rod-like viruses into different morphologies. (a) Schematic illustration of the depletion effect. The volume excluded to the center-of-mass of the depleting is indicated with light shadowing. Bringing two cylinders together results in an overlap of excluded volume shells, increases the accessible volume (entropy) of small depleting polymers, and leads to effective and tunable attractive interactions. (b) At high Dextran (500 k) concentration, mesoscopic disks stack up on top of each other and form smectic layers. (c) At intermediate dextran concentration, monolayer membranes with liquid order are formed [110]. (d) When relatively small-size polymer is used, such as PEG 8K, depletion can drive the viruses organizing into hexagonal platelets with positional order [109].

0.5.2 Templates or scaffolds for nanomaterials synthesis

The filamentous viruses, especially M13 phages, can be rationally genetically engineered or chemically modified to link with specific materials or chemical groups, which then serve as templates or scaffolds for a variety of applications, such as organization of complex nanostructures [113], ordering of quantum dots [114], drug-carrying [115], and imaging of

cancer cells [116]. Here we present the main strategies that have been reported to achieve the binding of desired functional groups or materials to the surface of these filamentous viruses.

(a) Phage display

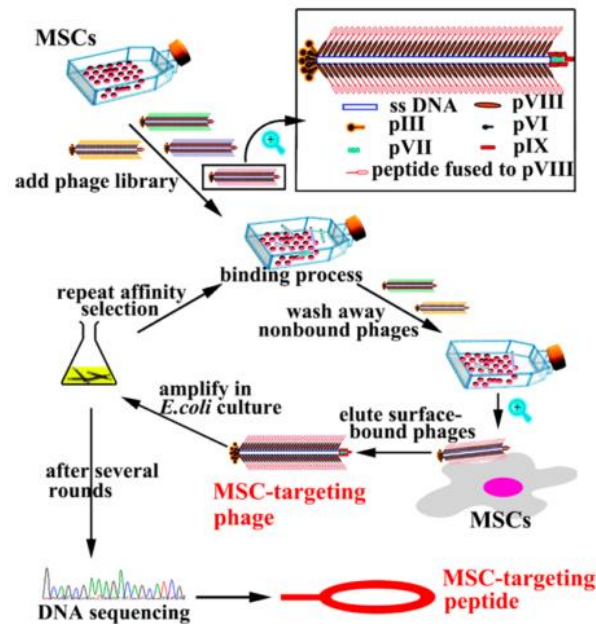


Figure 16: Scheme of the selection of mesenchymal stem cell (MSC): targeting peptides by screening a phage-displayed random peptide library against target cells. The process is called biopanning [117].

Phage display describes a selection technique in which a library of peptide or protein variants are expressed on the outside of a phage, while the genetic material encoding each variant resides on the inside [98], [118], [119]. This creates a physical linkage between each variant protein sequence and the DNA encoding it, which allows rapid partitioning based on binding affinity to a given target molecule (antibodies, enzymes, cell-surface receptors, etc.) by an *in vitro* selection process called panning [120]. In its simplest form, panning is carried out by incubating a library of phage-displayed peptides on a plate (or bead) coated with the target, washing away the unbound phage, and eluting the specifically bound phage (Figure 16). The eluted phage are then amplified and taken through additional binding/amplification cycles to enrich the pool in favor of binding sequences. After 3–4 rounds, individual clones are characterized by DNA sequencing and enzyme-linked immunosorbent assay (ELISA).

Filamentous virus is one of the most widely used systems to perform phage display. The inserted DNA encoding foreign peptides into the genes of specific coat proteins results in the

display of the peptides on the outer surface of the phage at the tip by genetic fusion to the N-terminus of minor coat proteins (e.g., p3 display), or along the side wall to the N-terminus of major coat proteins (i.e., p8 display). Since the surface (side wall or tips) of phage can be genetically modified to display designed peptides, the surface chemistry of the phage can be precisely controlled, which is an unique property that differentiates phages from other macromolecules [121].

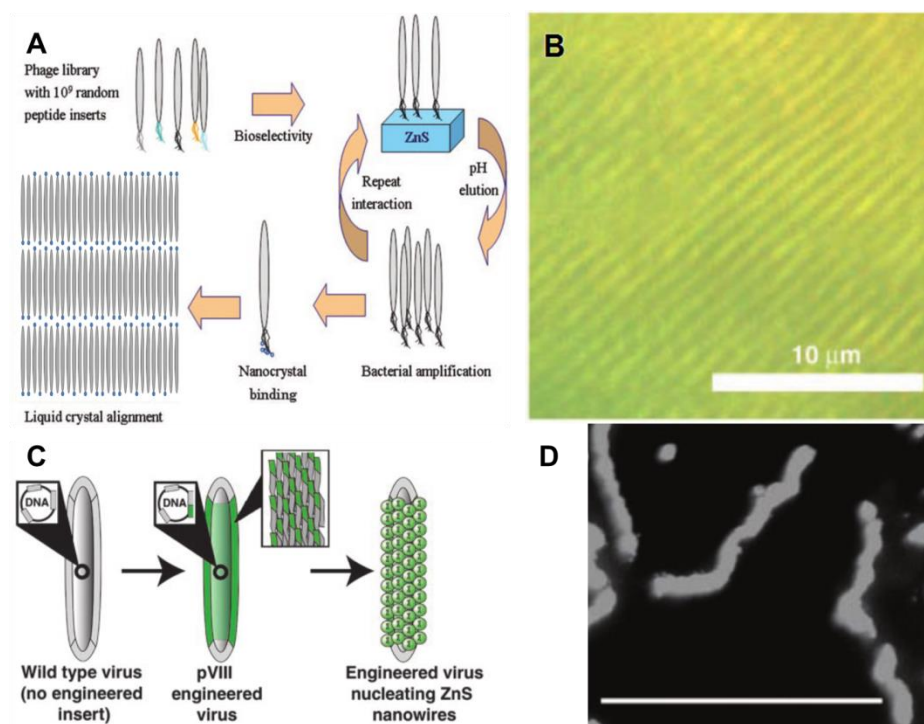


Figure 17: (A) Schematic diagram of the process used to generate layered nanocrystal films by the phage display method [114]. (B) Differential interference contrast microscopy (DIC) image shows interference patterns generated from parallel aligned smectic layers in the M13-ZnS suspension. (C) Illustration depicting peptide expression on the p8 protein, then subsequent nucleation of ZnS nanocrystals. (D) Annular dark field scanning transmission electron microscopy (ADF STEM) image shows the morphology of the resulting ZnS-virus nanowires [113].

When specific nanoparticle affinity is selected by phage display, filamentous viruses can also be used as template or scaffold to assemble or organize these nanoparticles into hierarchical structures. Belcher and her group members have utilized phase display of M13 viruses to bind magnetic or semiconducting nanocrystals and quantum dots, like FePt, CoPt, GaAs, ZnS, CdS, etc., [22], [49], [114], [122]–[126], either on the p3 tip or on the body (Figure 17). In these cases,

the DNA of p3 or p8 protein is modified to display peptides with specific recognition of the desired crystal surfaces. With the viruses as template or scaffold, nanocrystals are then arranged in nanowires [21], [113], [127] or layered film [114], [125].

Although phage display is a powerful technology, it relies entirely on peptide expressions and selections. If the needed functionalities were beyond peptide modification, the genetic tools would fail to address the requirements. In addition, the strength of interaction between desired materials and the specific binding peptide is normally weak (K_d between 10^{-6} and 10^{-9} M [128]). This results in a much lower efficiency of the binding, especially in solution, than other non-specific interaction, like streptavidin—biotin interaction which has a K_d of about 10^{-15} mM. Therefore, the alternative method, bioconjugation through chemical reaction, is put forward (see next section).

(b) Bioconjugation

Bioconjugation through specific chemical reaction is another frequently used technique to achieve functionalization on virus tip and body. For the functionalization on the full body of M13 phage, reaction with primary amine groups are often employed. Here, the amines include the side NH_2 of lysine and terminal NH_2 of p8 proteins. As the counterpart of this reaction, N-Hydroxysuccinimide (NHS) ester (Figure 18a) or Tetrafluorophenyl (TFP) ester activated compounds can be used. As a result of this simple way to generate functionalities, M13 bacteriophage has been chemically addressed with drugs [115], [129]–[131], RGD peptides [132], and fluorophores [43], [116], [133]. Besides, the DNA-mediated binding as an effective attraction has also been used to introduce target materials [134], [135]. Since the binding is thermally reversible, the linker can be switched on and off by tuning the temperature in a few degrees. In order to achieve the conjugation on virus tip, the exposed disulfide groups formed by cysteines on p3 proteins are often used. Disulfides can be reduced (normally by TCEP), forming thiols that react with maleimide (Figure 18b) or iodoacetyl activated compounds [136], [137]. It is also reported by Montalvan-Sorrosa et al. [138] that the formed thiols after reduction of disulfide groups are able to bond to Au nanoparticles, due to gold-sulfur reaction [139]. Note that they claim that the disulfide groups must be previously reduced to form thiol groups, and then bond to Au nanoparticles, which is not consistent with what we found: Au nanoparticles

bind directly with exposed disulfide groups on proximal end of the viruses. It will be discussed in Chapter 3.

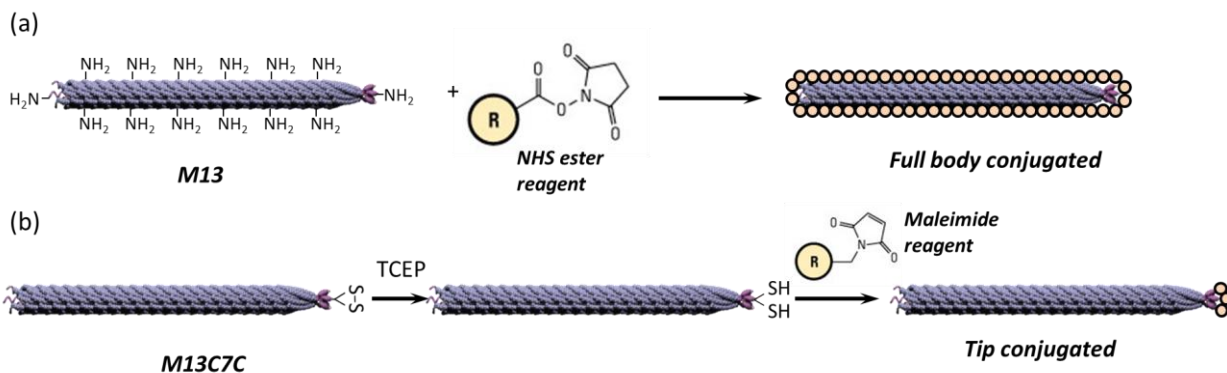


Figure 18: Scheme of bioconjugation on virus body and proximal tip. (a) The full body conjugation can be achieved by reaction between amine and NHS ester activated compounds. (b) Tip conjugation utilizes the disulfides that are available only at the proximal end of viruses (absent from main coat protein p8) to react with maleimide activated compounds after reduction by TCEP. R represents target functional groups or materials.

0.5.3 Building blocks for colloidal molecules

The filamentous viruses have also been used as building blocks for superstructures and colloidal molecules. The methodologies that presented in Section 0.5.2 can also be applied in assembly of colloidal molecules. For instance, phage display technique was used to select antistreptavidin binding motifs on p3 proteins and then react with streptavidin coated nanoparticles to create colloidal stars [126], [140]. Besides, train-like superstructures have also been assembled, via fused leucine zipper protein at both ends of the filamentous viruses [141]. However, the yield of the obtained colloidal complexes is low, due to the main drawback of phage display method: low binding affinity between viruses and selected materials (as mentioned in Section 0.5.2a). The bioconjugation through specific chemical reaction has also been employed to assemble virus based colloidal molecules, mainly through the thiols formed by reduction of disulfides on the proximal end [136]. DNA binding on the other hand has also been employed to assemble end-to-end multiphage structures. But these methods either show low efficiency of the binding reaction or high polydispersity in number of reacted viruses of obtained structures [142], [143]. Besides, the reproducibility of the methods is always poor.

0.6 Outline of the thesis

Because of the rich properties of filamentous viruses as model system of colloidal rods, our group intends to use these viruses to construct hierarchical colloidal architectures. In this thesis, filamentous viruses are used as building blocks specifically for the assembly of hybrid colloidal molecules. As mentioned previously, the existing methods to assemble colloidal molecules from filamentous viruses always show low efficiency or lack of control of the valency (n , number of reacted viruses in one colloidal molecule). In order to solve these issues, we propose two main strategies to introduce strong interaction between the tip of viruses, based on affinity of streptavidin to biotin and Au-sulfur reaction, respectively.

In Chapter 1, the virus based colloidal molecules are constructed based on affinity of streptavidin to biotin. Beforehand, a biotinylation step is performed at the proximal end of the viruses. Then the chemically biotinylated M13C7C viruses have reacted with streptavidin activated nanoparticles via their functionalized proximal ends. As a comparison, the mutants M13-AS bacteriophages displaying Step-tag histidine-proline-glutamine (HPQ) at their proximal ends are also used to bind with streptavidin coated nanoparticles. The affinity for streptavidin of the M13-AS viruses is measured by determining the dissociation constant, K_d . For both viral systems, a theoretical descript is shown by developing a quantitative model of the self-assembly and interaction of the modified viruses with streptavidin compounds. Virus based colloidal molecules of different valencies are then produced by conjugation of these tip-functionalized viruses with streptavidin activated nanoparticles. Thanks to a fluorescent labeling of the viral arms, the dynamics of such systems is also presented in real time by fluorescence microscopy.

The biotin-streptavidin method to create colloidal molecules (Chapter 1) includes steps of thiolation, biotinylation, and binding to streptavidin activated nanoparticles. Experimentally, we find that the thiolation is the key step that influences mostly the final yield. Therefore, in Chapter 2 we present the optimization details for the thiolation step. Several aspects, like the reducing reagent, concentration, time, temperature, etc., have been discussed. Finally, we establish an optimal thiolation process using iTCEP (Tris(2-carboxyethyl)phosphine hydrochloride immobilized by grafting on agarose beads) as reducing reagent. In order to characterize the efficiency of thiolation, we label the viruses with fluorescent dyes through

thiol—maleimide reaction, and the efficiency of thiolation step is quantified by the number of grafted dyes.

Although we succeeded to produce efficiently colloidal molecules utilizing biotin-streptavidin interaction, the whole process remains complicated and intricate. Besides, the degradation and release of streptavidin from nanoparticle surface with time still limits the stability of these colloidal molecules. Therefore, in Chapter 3, another more convenient and reliable method is raised based on the interaction between sulfur and noble metals. Thanks to the exposed disulfide groups located at p3 proteins, metallic nanoparticles are able to selectively bind to proximal ends of the M13 virus. The generic feature of this binding is verified by using different metallic nanoparticles (Au, Pt, Ag) and two virus strains (M13KE, M13C7C). In addition, the efficiency of this metal-sulfur reaction at virus proximal tips is optimized by investigating the influences of main experimental conditions, like capping reagent, ionic strength and molar excess.

In Chapter 3, our interest is focused on developing and optimizing metal-sulfur reaction at virus tip. In Chapter 4, we aim at controlling the valency, n , of the obtained colloidal molecules. Au nanobeads (AuNBs) and M13C7C viruses are chosen as building blocks in these investigations because AuNBs are easily tuned in size and show the highest affinity to M13C7C. Under the condition of a high excess of viruses per AuNB, two main aspects, size of AuNBs and effective electrostatic diameter of viruses, are found to significantly influence the valency. A quantitative model is built correspondingly, using AuNB diameter and ionic strength as variables, which accounts for assembly of colloidal molecules with the desired valency. Based on this model, we succeed to produce in large scale the simplest multivalent colloidal molecules, i.e., AB₂ type colloidal molecules ($n = 2$, two viruses reacted with one AuNB).

In Chapter 5, we further develop the metal-sulfide method to assemble heterobifunctional diblocks using M13C7C viruses as scaffolds. As a proof-of-concept experiment, bicolored diblocks are produced. A three-step procedure has been established. Yield of the heterobifunctional diblocks mainly depends on the last step. Therefore, the experimental conditions have been optimized for the last step by adding TCEP to break disulfide bridges which makes the sulfur more exposed to AuNBs. The obtained visualizable bicolored diblocks are used in the investigations of dynamics of flexible colloidal dimers. Especially, the

correlation between the red and green blocks, i.e. angle between them, is characterized by tracking each block simultaneously.

In the general conclusion, we summarize all the results obtained by using M13 viruses as building blocks to assembly rod-based colloidal molecules. Some perspectives with this system are also shown, including the further self-assembly of viruses in to more hierarchical superstructures at both ends and their self-organization in to hybrid biologic/metallic periodic multilayers.

0.7 References

- [1] W. Poon. Colloids as Big Atoms. *Science*, 2004, 304: 830–831.
- [2] Z. Wang, F. Wang, Y. Peng, Z. Zheng, and Y. Han. Imaging the homogeneous nucleation during the melting of superheated colloidal crystals. *Science*, 2012, 338: 87–90.
- [3] J. Russo and H. Tanaka. The microscopic pathway to crystallization in supercooled liquids. *Sci. Rep.*, 2012, 2: 505.
- [4] P. N. Pusey and W. van Megen. Observation of a Glass Transition in Suspensions of Spherical Colloidal Particles. *Phys. Rev. Lett.*, 1987, 59: 2083–2086.
- [5] P. N. Pusey and W. van Megen. Phase behaviour of concentrated suspensions of nearly hard colloidal spheres. *Nature*, 1986, 320: 340–342.
- [6] P. N. Pusey, W. Van Megen, P. Bartlett, B. J. Ackerson, J. G. Rarity, and S. M. Underwood. Structure of crystals of hard colloidal spheres. *Phys. Rev. Lett.*, 1989, 63: 2753–2756.
- [7] E. Grelet. Hexagonal order in crystalline and columnar phases of hard rods. *Phys. Rev. Lett.*, 2008, 100: 168301.
- [8] Z. Dogic and S. Fraden. Smectic Phase in a Colloidal Suspension of Semi flexible Virus Particles. *Phys. Rev. Lett.*, 1997, 78: 2417–2420.
- [9] J. Tang and S. Fraden. Isotropic-cholesteric phase transition in colloidal suspensions of filamentous bacteriophage fd. *Liq. Cryst.*, 1995, 19: 459–467.
- [10] O. D. Velev and S. Gupta. Materials fabricated by micro- and nanoparticle assembly - The challenging path from science to engineering. *Adv. Mater.*, 2009, 21: 1897–1905.
- [11] G. A. Ozin *et al.* Nanofabrication by self-assembly. *Mater. Today*, 2009, 12: 12–23.
- [12] V. N. Manoharan. Colloidal matter: Packing, geometry, and entropy. *Science*, 2015, 349: 1253751.
- [13] G. M. Whitesides. Self-Assembly at All Scales. *Science*, 2002, 295: 2418–2421.
- [14] M. R. Jones and C. A. Mirkin. Materials science: Self-assembly gets new direction. *Nature*, 2012, 491: 42–43.
- [15] J. Zhang, Z. Sun, and B. Yang. Self-assembly of photonic crystals from polymer colloids. *Curr. Opin. Colloid Interface Sci.*, 2009, 14: 103–114.
- [16] J. F. Galisteo-López, M. Ibisate, R. Sapienza, L. S. Froufe-Pérez, Ú. Blanco, and C. López. Self-

- assembled photonic structures. *Adv. Mater.*, 2011, 23: 30–69.
- [17] D. Mophew, J. Shaw, C. Avins, and D. Chakrabarti. Programming Hierarchical Self-Assembly of Patchy Particles into Colloidal Crystals via Colloidal Molecules. *ACS Nano*, 2018, 12: 2355–2364.
- [18] G. R. Yi, D. J. Pine, and S. Sacanna. Recent progress on patchy colloids and their self-assembly. *J. Phys. Condens. Matter*, 2013, 25: 193101.
- [19] S. Sacanna and D. J. Pine. Shape-anisotropic colloids: Building blocks for complex assemblies. *Curr. Opin. Colloid Interface Sci.*, 2011, 16: 96–105.
- [20] G. van Anders, N. K. Ahmed, R. Smith, M. Engel, and S. C. Glotzer. Entropically patchy particles: Engineering valence through shape entropy. *ACS Nano*, 2014, 8: 931–940.
- [21] K. T. Nam *et al.* Virus-Enabled Synthesis and Assembly of Nanowires for Lithium Ion Battery Electrodes. *Science*, 2006, 312: 885–888.
- [22] X. Dang *et al.* Virus-templated self-assembled single-walled carbon nanotubes for highly efficient electron collection in photovoltaic devices. *Nat. Nanotechnol.*, 2011, 6: 377–84.
- [23] T. Mirkovic, N. S. Zacharia, G. D. Scholes, and G. A. Ozin. Nanolocomotion - Catalytic nanomotors and nanorotors. *Small*, 2010, 6: 159–167.
- [24] A. van Blaaderen. Colloidal Molecules and Beyond. *Science*, 2003, 301: 470–471.
- [25] E. Duguet, A. Désert, A. Perro, and S. Ravaine. Design and elaboration of colloidal molecules: an overview. *Chem. Soc. Rev.*, 2011, 40: 941.
- [26] F. Li, W. C. Yoo, M. B. Beernink, and A. Stein. Site-specific functionalization of anisotropic nanoparticles: From colloidal atoms to colloidal molecules. *J. Am. Chem. Soc.*, 2009, 131: 18548–18555.
- [27] M. Grzelczak, J. Vermant, E. M. Furst, L. M. Liz-Marzán, and L. M. Liz-Marzá. Directed Self-Assembly of Nanoparticles. *ACS Nano*, 2010, 4: 3591–3605.
- [28] U. Jeong, Y. Wang, M. Ibisate, and Y. Xia. Some new developments in the synthesis, functionalization, and utilization of monodisperse colloidal spheres. *Adv. Funct. Mater.*, 2005, 15: 1907–1921.
- [29] D. J. Norris, E. G. Arlinghaus, L. Meng, R. Heiny, and L. E. Scriven. Opaline photonic crystals: How does self-assembly work? *Adv. Mater.*, 2004, 16: 1393–1399.
- [30] E. W. Seelig, B. Tang, A. Yamilov, H. Cao, and R. P. H. Chang. Self-assembled 3D photonic crystals from ZnO colloidal spheres. *Mater. Chem. Phys.*, 2003, 80: 257–263.
- [31] E. Yablonovitch. Inhibited spontaneous emission in solid-state physics and electronics. *Phys. Rev. Lett.*, 1987, 58: 2059–2062.
- [32] H. Míguez *et al.* Photonic crystal properties of packed submicrometric SiO₂ spheres. *Appl. Phys. Lett.*, 1997, 71: 1148–1150.
- [33] A. P. Hynninen, C. G. Christova, R. van Roij, A. van Blaaderen, and M. Dijkstra. Prediction and observation of crystal structures of oppositely charged colloids. *Phys. Rev. Lett.*, 2006, 96: 138308.
- [34] F. Li, D. P. Josephson, and A. Stein. Colloidal assembly: The road from particles to colloidal molecules and crystals. *Angew. Chem. Int. Ed.*, 2011, 50: 360–388.
- [35] S. C. Glotzer and M. J. Solomon. Anisotropy of building blocks and their assembly into complex

- structures. *Nat. Mater.*, 2007, 6: 557–562.
- [36] J. A. Millan, D. Ortiz, G. van Anders, and S. C. Glotzer. Self-assembly of archimedean tilings with enthalpically and entropically patchy polygons. *ACS Nano*, 2014, 8: 2918–2928.
- [37] A. B. Pawar and I. Kretzschmar. Fabrication, assembly, and application of patchy particles. *Macromol. Rapid Commun.*, 2010, 31: 150–168.
- [38] S. Sacanna, W. T. M. Irvine, P. M. Chaikin, and D. J. Pine. Lock and key colloids. *Nature*, 2010, 464: 575–578.
- [39] Y. Wang *et al.* Three-dimensional lock and key colloids. *J. Am. Chem. Soc.*, 2014, 136: 6866–6869.
- [40] A. Kuijk, D. V Byelov, A. V Petukhov, A. van Blaaderen, and A. Imhof. Phase behavior of colloidal silica rods. *Faraday Discuss.*, 2012, 159: 181–199.
- [41] M. A. Bates, D. Frenkel, M. A. Bates, and D. Frenkel. Phase behavior of two-dimensional hard rod fluids Phase behavior of two-dimensional hard rod fluids. *J. Chem. Phys.*, 2000, 112: 10033–10041.
- [42] J. Viamontes, P. W. Oakes, and J. X. Tang. Isotropic to nematic liquid crystalline phase transition of F-actin varies from continuous to first order. *Phys. Rev. Lett.*, 2006, 97: 118103.
- [43] M. P. Lettinga, E. Barry, and Z. Dogic. Self-diffusion of rod-like viruses in the nematic phase. *Europhys. Lett.*, 2005, 71: 692–698.
- [44] K. R. Purdy and S. Fraden. Isotropic-cholesteric phase transition of filamentous virus suspensions as a function of rod length and charge. *Phys. Rev. E*, 2004, 70: 61703.
- [45] Z. Dogic and S. Fraden. Ordered phases of filamentous viruses. *Curr. Opin. Colloid Interface Sci.*, 2006, 11: 47–55.
- [46] E. Grelet. Hard-rod behavior in dense mesophases of semiflexible and rigid charged viruses. *Phys. Rev. X*, 2014, 4: 21053.
- [47] E. Barry, D. Beller, and Z. Dogic. A model liquid crystalline system based on rodlike viruses with variable chirality and persistence length. *Soft Matter*, 2009, 5: 2563–2570.
- [48] J. H. Lee *et al.* Phage-Based Structural Color Sensors and Their Pattern Recognition Sensing System. *ACS Nano*, 2017, 11: 3632–3641.
- [49] Y. S. Nam *et al.* Virus-templated assembly of porphyrins into light-harvesting nanoantennae. *J. Am. Chem. Soc.*, 2010, 132: 1462–1463.
- [50] L. Rossi, S. Sacanna, W. T. M. Irvine, P. M. Chaikin, D. J. Pine, and A. P. Philipse. Cubic crystals from cubic colloids. *Soft Matter*, 2011, 7: 4139–4142.
- [51] S. Adireddy, C. Lin, B. Cao, W. Zhou, and G. Caruntu. Solution-based growth of monodisperse cube-like BaTiO₃ colloidal nanocrystals. *Chem. Mater.*, 2010, 22: 1946–1948.
- [52] T. Sugimoto, M. M. Khan, A. Muramatsu, and H. Itoh. Formation mechanism of monodisperse peanut-type α -Fe₂O₃ particles from condensed ferric hydroxide gel. *Colloids Surf. A*, 1993, 70: 167–169.
- [53] Y. Yin, C. Erdonmez, S. Aloni, and A. P. Alivisatos. Faceting of nanocrystals during chemical transformation: From solid silver spheres to hollow gold octahedra. *J. Am. Chem. Soc.*, 2006, 128: 12671–12673.
- [54] Q. Chen, J. Yan, J. Zhang, S. C. Bae, and S. Granick. Janus and Multiblock Colloidal Particles.

- Langmuir*, 2012, 28: 13555–13561.
- [55] H. Takei and N. Shimizu. Gradient Sensitive Microscopic Probes Prepared by Gold Evaporation and Chemisorption on Latex Spheres. *Langmuir*, 1997, 13: 1865–1868.
- [56] A. Perro, S. Reculosa, S. Ravaine, E. Bourgeat-Lami, and E. Duguet. Design and synthesis of Janus micro- and nanoparticles. *J. Mater. Chem.*, 2005, 15: 3745.
- [57] G. Zhang, D. Wang, and H. Möhwald. Patterning microsphere surfaces by templating colloidal crystals. *Nano Lett.*, 2005, 5: 143–146.
- [58] A. B. Pawar and I. Kretzschmar. Multifunctional patchy particles by glancing angle deposition. *Langmuir*, 2009, 25: 9057–9063.
- [59] Y. P. Zhao, D. X. Ye, G. C. Wang, and T. M. Lu. Novel Nano-Column and Nano-Flower Arrays by Glancing Angle Deposition. *Nano Lett.*, 2002, 2: 351–354.
- [60] A. B. Pawar and I. Kretzschmar. Patchy particles by glancing angle deposition. *Langmuir*, 2008, 24: 355–358.
- [61] Y. Wang *et al.* Colloids with valence and specific directional bonding. *Nature*, 2012, 491: 51–5.
- [62] V. N. Manoharan, M. T. Elsesser, and D. J. Pine. Dense Packing and Symmetry in Small Clusters of Microspheres. *Science*, 2003, 301: 483–487.
- [63] K. Chaudhary, Q. Chen, J. J. Juárez, S. Granick, and J. A. Lewis. Janus colloidal matchsticks. *J. Am. Chem. Soc.*, 2012, 134: 12901–12903.
- [64] D. Morphew and D. Chakrabarti. Clusters of anisotropic colloidal particles: From colloidal molecules to supracolloidal structures. *Curr. Opin. Colloid Interface Sci.*, 2017, 30: 70–80.
- [65] A. F. Demirörs, P. P. Pillai, B. Kowalczyk, and B. A. Grzybowski. Colloidal assembly directed by virtual magnetic moulds. *Nature*, 2013, 503: 99–103.
- [66] A. Perro, E. Duguet, O. Lambert, J. C. Taveau, E. Bourgeat-Lami, and S. Ravaine. A chemical synthetic route towards “Colloidal molecules.” *Angew. Chem. Int. Ed.*, 2009, 48: 361–365.
- [67] D. J. Kraft, W. S. Vlug, C. M. van Kats, A. van Blaaderen, A. Imhof, and W. K. Kegel. Self-assembly of colloids with liquid protrusions. *J. Am. Chem. Soc.*, 2009, 131: 1182–1186.
- [68] S. H. Kim, G. R. Yi, K. H. Kim, and S. M. Yang. Photocurable pickering emulsion for colloidal particles with structural complexity. *Langmuir*, 2008, 24: 2365–2371.
- [69] G. R. Yi, V. N. Manoharan, E. Michel, M. T. Elsesser, S. M. Yang, and D. J. Pine. Colloidal clusters of silica or polymer microspheres. *Adv. Mater.*, 2004, 16: 1204–1208.
- [70] Y. Xia, Y. Yin, Y. Lu, and J. McLellan. Template-Assisted Self-Assembly of Spherical Colloids into Complex and Controllable Structures. *Adv. Funct. Mater.*, 2003, 13: 907–918.
- [71] Y. Yin, Y. Lu, B. Gates, and Y. Xia. Template-assisted self-assembly: A practical route to complex aggregates of monodispersed colloids with well-defined sizes, shapes, and structures. *J. Am. Chem. Soc.*, 2001, 123: 8718–8729.
- [72] D. Luo, C. Yan, and T. Wang. Interparticle Forces Underlying Nanoparticle Self-Assemblies. *Small*, 2015, 11: 5984–6008.
- [73] Z. Dogic, P. Sharma, and M. J. Zakhary. Hypercomplex Liquid Crystals. *Annu. Rev. Condens. Matter Phys.*, 2014, 5: 137–157.
- [74] H. N. W. Lekkerkerker and R. Tuinier. *Colloids and the Depletion Interaction*, 1st ed. Springer, 2011.

-
- [75] C. Hubert *et al.* Synthesis of multivalent silica nanoparticles combining both enthalpic and entropic patchiness. *Faraday Discuss.*, 2015, 181: 139–146.
- [76] Q. Chen, S. C. Bae, and S. Granick. Directed self-assembly of a colloidal kagome lattice. *Nature*, 2011, 469: 381–384.
- [77] Q. Chen, S. C. Bae, and S. Granick. Staged self-assembly of colloidal metastructures. *J. Am. Chem. Soc.*, 2012, 134: 11080–11083.
- [78] H. Qiu, Z. M. Hudson, M. A. Winnik, and I. Manners. Multidimensional hierarchical self-assembly of amphiphilic cylindrical block comicelles. *Science*, 2015, 347: 1329–1332.
- [79] H. Qiu, G. Russo, P. A. Rugar, L. Chabanne, M. A. Winnik, and I. Manners. Tunable supermicelle architectures from the hierarchical self-assembly of amphiphilic cylindrical B-A-B triblock Co-micelles. *Angew. Chem. Int. Ed.*, 2012, 51: 11882–11885.
- [80] F. Oosawa. Interaction between parallel rodlike macroions. *Biopolymers*, 1968, 6: 1633–1647.
- [81] B. O’Shaughnessy and Q. Yang. Manning-Oosawa counterion condensation. *Phys. Rev. Lett.*, 2005, 94: 48302.
- [82] A. Naji, S. Jungblut, A. G. Moreira, and R. R. Netz. Electrostatic interactions in strongly coupled soft matter. *Physica A*, 2005, 352: 131–170.
- [83] R. R. Netz. Electrostatics of counter-ions at and between planar charged walls: From Poisson-Boltzmann to the strong-coupling theory. *Eur. Phys. J. E*, 2001, 5: 557–574.
- [84] A. Naji and R. R. Netz. Attraction of like-charged macroions in the strong-coupling limit. *Eur. Phys. J. E*, 2004, 13: 43–59.
- [85] L. Šamaj and E. Trizac. Wigner-crystal formulation of strong-coupling theory for counterions near planar charged interfaces. *Phys. Rev. E*, 2011, 84: 41401.
- [86] A. Naji, M. Kanduc, J. Forsman, and R. Podgornik. Perspective: Coulomb fluids--weak coupling, strong coupling, in between and beyond. *J. Chem. Phys.*, 2013, 139: 150901.
- [87] J. L. Sikorav, J. Pelta, and F. Livolant. A Liquid Crystalline Phase in Spermidine-Condensed DNA. *Biophys. J.*, 1994, 67: 1387–1392.
- [88] J. Pelta, F. Livolant, and J. L. Sikorav. DNA aggregation induced by polyamines and cobalthexamine. *J. Biol. Chem.*, 1996, 271: 5656–5662.
- [89] J. Pelta, D. Durand, J. Doucet, and F. Livolant. DNA mesophases induced by spermidine: structural properties and biological implications. *Biophys. J.*, 1996, 71: 48–63.
- [90] E. Raspaud, D. Durand, and F. Livolant. Interhelical spacing in liquid crystalline spermine and spermidine-DNA precipitates. *Biophys. J.*, 2005, 88: 392–403.
- [91] J. X. Tang, P. A. Janmey, A. Lyubartsev, and L. Nordenskiöld. Metal ion-induced lateral aggregation of filamentous viruses fd and M13. *Biophys. J.*, 2002, 83: 566–581.
- [92] J. C. Butler, T. Angelini, J. X. Tang, and G. C. L. Wong. Ion multivalence and like-charge polyelectrolyte attraction. *Phys. Rev. Lett.*, 2003, 91: 28301.
- [93] P. F. Damasceno, M. Engel, and S. C. Glotzer. Predictive Self-Assembly of Polyhedra into Complex Structures. *Science*, 2012, 453: 453–458.
- [94] G. van Anders, D. Klotsa, N. K. Ahmed, M. Engel, and S. C. Glotzer. Understanding shape entropy through local dense packing. *Proc. Natl. Acad. Sci.*, 2014, 111: E4812–E4821.
- [95] E. Grelet and R. Rana. From soft to hard rod behavior in liquid crystalline suspensions of

- sterically stabilized colloidal filamentous particles. *Soft Matter*, 2016, 12: 4621–4627.
- [96] Y. Yang, G. Chen, L. J. Martinez-Miranda, H. Yu, K. Liu, and Z. Nie. Synthesis and Liquid-Crystal Behavior of Bent Colloidal Silica Rods. *J. Am. Chem. Soc.*, 2016, 138: 68–71.
- [97] D. A. Marvin, M. F. Symmons, and S. K. Straus. Structure and assembly of filamentous bacteriophages. *Prog. Biophys. Mol. Biol.*, 2014, 114: 80–122.
- [98] G. P. Smith and V. A. Petrenko. Phage display. *Chem. Rev.*, 1997, 97: 391–410.
- [99] D. Marvin. Filamentous phage structure, infection and assembly. *Curr. Opin. Struct. Biol.*, 1998, 8: 150–158.
- [100] S. Bhattacharjee, M. J. Glucksman, and L. Makowski. Structural polymorphism correlated to surface charge in filamentous bacteriophages. *Biophys. J.*, 1992, 61: 725–735.
- [101] Z. Dogic and S. Fraden. Cholesteric phase in virus suspensions. *Langmuir*, 2000, 16: 7820–7824.
- [102] Z. Dogic and S. Fraden. Development of model colloidal liquid crystals and the kinetics of the isotropic-smectic transition. *Philos. Trans. R. Soc. A*, 2001, 359: 997–1015.
- [103] Z. Dogic. Surface freezing and a two-step pathway of the isotropic-smectic phase transition in colloidal rods. *Phys. Rev. Lett.*, 2003, 91: 165701.
- [104] E. Pouget, E. Grelet, and M. P. Lettinga. Dynamics in the smectic phase of stiff viral rods. *Phys. Rev. E*, 2011, 84: 41704.
- [105] M. P. Lettinga and E. Grelet. Self-diffusion of rodlike viruses through smectic layers. *Phys. Rev. Lett.*, 2007, 99: 197802.
- [106] E. Grelet, M. Paul Lettinga, M. Bier, R. Van Roij, and P. Van Der Schoot. Dynamical and structural insights into the smectic phase of rod-like particles. *J. Phys. Condens. Matter*, 2008, 20: 494213.
- [107] S. Naderi, E. Pouget, P. Ballesta, P. van der Schoot, M. P. Lettinga, and E. Grelet. Fractional hoppinglike motion in columnar mesophases of semiflexible rodlike particles. *Phys. Rev. Lett.*, 2013, 111: 37801.
- [108] L. Alvarez, M. P. Lettinga, and E. Grelet. Fast Diffusion of Long Guest Rods in a Lamellar Phase of Short Host Particles. *Phys. Rev. Lett.*, 2017, 118: 178002.
- [109] B. Sung, A. de la Cotte, and E. Grelet. Chirality-controlled crystallization via screw dislocations. *Nat. Commun.*, 2018, 9: 1405.
- [110] E. Barry and Z. Dogic. Entropy driven self-assembly of nonamphiphilic colloidal membranes. *Proc. Natl. Acad. Sci.*, 2010, 107: 10348–10353.
- [111] P. Sharma, A. Ward, T. Gibaud, M. F. Hagan, and Z. Dogic. Hierarchical organization of chiral rafts in colloidal membranes. *Nature*, 2014, 513: 77–80.
- [112] T. Gibaud *et al.* Reconfigurable self-assembly through chiral control of interfacial tension. *Nature*, 2012, 481: 348–351.
- [113] C. Mao *et al.* Viral assembly of oriented quantum dot nanowires. *Proc. Natl. Acad. Sci.*, 2003, 100: 6946–6951.
- [114] S.-W. Lee, C. Mao, C. E. Flynn, and A. M. Belcher. Ordering of Quantum Dots Using Genetically Engineered Viruses. *Science*, 2002, 296: 892–895.
- [115] I. Yacoby, M. Shamis, H. Bar, D. Shabat, and I. Benhar. Targeting antibacterial agents by using drug-carrying filamentous bacteriophages. *Antimicrob. Agents Chemother.*, 2006, 50: 2087–2097.

- [116] Q. Wang *et al.* Chemical modification of M13 bacteriophage and its application in cancer cell imaging. *Bioconjug. Chem.*, 2010, 21: 1369–77.
- [117] G. Abbineni, S. Modali, B. Safiejko-Mrocza, V. A. Petrenko, and C. Mao. Evolutionary selection of new breast cancer cell-targeting peptides and phages with the cell-targeting peptides fully displayed on the major coat and their effects on actin dynamics during cell internalization. *Mol. Pharm.*, 2010, 7: 1629–1642.
- [118] D. J. Rodi and L. Makowski. Phage-display technology - Finding a needle in a vast molecular haystack. *Curr. Opin. Biotechnol.*, 1999, 10: 87–93.
- [119] S. S. Sidhu. Phage display in pharmaceutical biotechnology. *Curr. Opin. Biotechnol.*, 2000, 11: 610–616.
- [120] S. F. Parmley and G. P. Smith. Antibody-selectable filamentous fd phage vectors: affinity purification of target genes. *Gene*, 1988, 73: 305–318.
- [121] B. P. Gray and K. C. Brown. Combinatorial peptide libraries: Mining for cell-binding peptides. *Chem. Rev.*, 2014, 114: 1020–1081.
- [122] S. R. Whaley, D. S. English, E. L. Hu, P. F. Barbara, and A. M. Belcher. Selection of peptides with semiconductor binding specificity for directed nanocrystal assembly. *Nature*, 2000, 405: 665–8.
- [123] B. D. Reiss, C. Mao, D. J. Solis, K. S. Ryan, T. Thomson, and A. M. Belcher. Biological routes to metal alloy ferromagnetic nanostructures. *Nano Lett.*, 2004, 4: 1127–1132.
- [124] K. T. Nam, B. R. Reelle, S. W. Lee, and A. M. Belcher. Genetically Driven Assembly of Nanorings Based on the M13 Virus. *Nano Lett.*, 2004, 4: 23–27.
- [125] S. W. Lee, S. K. Lee, and A. M. Belcher. Virus-based alignment of inorganic, organic, and biological nanosized materials. *Adv. Mater.*, 2003, 15: 689–692.
- [126] Y. Huang *et al.* Programmable Assembly of Nanoarchitectures Using Genetically Engineered Viruses. *Nano Lett.*, 2005, 5: 1429–34.
- [127] C. Mao *et al.* Virus-Based Toolkit for the Directed Synthesis of Magnetic and Semiconducting Nanowires. *Science*, 2004, 303: 213–217.
- [128] G. Winter, A. D. Griffiths, R. E. Hawkins, and H. R. Hoogenboom. Making Antibodies by Phage Display Technology. *Annu. Rev. Immunol.*, 1994, 12: 433–455.
- [129] I. Yacoby, H. Bar, and I. Benhar. Targeted drug-carrying bacteriophages as antibacterial nanomedicines. *Antimicrob. Agents Chemother.*, 2007, 51: 2156–2163.
- [130] I. Yacoby and I. Benhar. Targeted filamentous bacteriophages as therapeutic agents. *Expert Opin. Drug Deliv.*, 2008, 5: 321–330.
- [131] H. Bar, I. Yacoby, and I. Benhar. Killing cancer cells by targeted drug-carrying phage nanomedicines. *BMC Biotechnol.*, 2008, 8: 1–14.
- [132] J. Rong *et al.* Oriented cell growth on self-assembled bacteriophage M13 thin films. *Chem. Commun.*, 2008, 5185–5187.
- [133] D. L. Jaye, C. M. Geigerman, R. E. Fuller, A. Akyildiz, and C. A. Parkos. Direct fluorochrome labeling of phage display library clones for studying binding specificities: Applications in flow cytometry and fluorescence microscopy. *J. Immunol. Methods*, 2004, 295: 119–127.
- [134] Z. Ruff *et al.* Designing disordered materials using DNA-coated colloids of bacteriophage fd and gold. *Faraday Discuss.*, 2016, 186: 473–488.

- [135] M. Chiappini, E. Eiser, and F. Sciortino. Phase behaviour in complementary DNA-coated gold nanoparticles and fd-viruses mixtures: a numerical study. *Eur. Phys. J. E*, 2017, 40: 7.
- [136] F. Huang *et al.* Pair potential of charged colloidal stars. *Phys. Rev. Lett.*, 2009, 102: 108302.
- [137] K. E. Sapsford *et al.* Functionalizing nanoparticles with biological molecules: Developing chemistries that facilitate nanotechnology. *Chem. Rev.*, 2013, 113: 1904–2074.
- [138] D. Montalvan-Sorrososa, J. L. González-Solis, J. Mas-Oliva, and R. Castillo. Filamentous virus decoration with gold nanoparticles: global fingerprints of bionanocomposites acquired with SERS. *RSC Adv.*, 2014, 4: 57329–57336.
- [139] R. Bott. Fundamental Studies of the Chemisorption of Organosulfur Compounds on Au(111). Implications for Molecular Self-Assembly on Gold Surfaces. *J. Am. Chem. Soc.*, 1987, 109: 733–740.
- [140] A. S. Khalil *et al.* Single M13 bacteriophage tethering and stretching. *Proc. Natl. Acad. Sci.*, 2007, 104: 4892–4897.
- [141] R. Y. Sweeney, E. Y. Park, B. L. Iverson, and G. Georgiou. Assembly of Multimeric Phage Nanostructures Through Leucine Zipper Interactions. *Biotechnol. Bioeng.*, 2006, 95: 539–545.
- [142] F. Huang. Interactions and Collective Behavior of Attractive Colloidal Rods and Microspheres Grafted with Filamentous Bacteriophage. *Brandeis University*, 2009.
- [143] G. T. Hess, C. P. Guimaraes, E. Spooner, H. L. Ploegh, and A. M. Belcher. Orthogonal labeling of M13 minor capsid proteins with DNA to self-assemble end-to-end multiphage structures. *ACS Synth. Biol.*, 2013, 2: 490–496.

Chapter 1

Rod-like virus based multiarm colloidal molecules

This part of work is done by collaboration mainly with Alexis de la Cotte, former PhD student in our group. The results have already been published in the *ACS Nano* on 2017. Therefore, we present the preprint version of this paper as Chapter 1.

In this Chapter, two different types of tip-functionalized M13 viruses are used to assemble the colloidal molecules, including genetically engineered M13-AS displaying Strep-tags and chemically biotinylated M13C7C viruses. For both viral systems, a theoretical comparison is performed by developing a quantitative model of the self-assembly and interaction with streptavidin compounds. Virus based colloidal molecules of different valencies are then produced by conjugation of these tip-functionalized viruses with streptavidin activated nanoparticles, with valency can be solely controlled by tuning the molar excess. Besides, the dynamics of such systems is also investigated in real time by fluorescence microscopy, thanks to the fluorescent labeling of the viral arms.

Rod-Like Virus Based Multiarm Colloidal Molecules

Alexis de la Cotte^{1,‡}, Cheng Wu^{1,‡}, Marie Trévisan¹, Andrii Repula¹, Eric Grelet^{1,*}

¹*Centre de Recherche Paul-Pascal, CNRS & Université de Bordeaux,
115 Avenue Schweitzer, 33600 Pessac, France*

Abstract

We report on the construction of multiarm colloidal molecules by tip-linking filamentous bacteriophages, functionalized either by biological engineering or chemical conjugation. The affinity for streptavidin of a genetically modified vector phage displaying Strep-tags fused to one end of the viral particle, is measured by determining the dissociation constant, K_d . In order to both improve the colloidal stability and the efficiency of the self-assembly process, a biotinylation protocol having a chemical yield higher than 90% is presented to regio-selectively functionalize the cystein residues located at one end of the bacteriophages. For both viral systems, a theoretical comparison is performed by developing a quantitative model of the self-assembly and interaction of the modified viruses with streptavidin compounds, which accurately accounts for our experimental results. Multiarm colloidal structures of different valencies are then produced by conjugation of these tip-functionalized viruses with streptavidin activated nanoparticles. We succeed to form stable virus based colloidal molecules, whose number of arms, called valency, is solely controlled by tuning the molar excess. Thanks to a fluorescent labeling of the viral arms, the dynamics of such systems is also presented in real time by fluorescence microscopy.

Keywords: self-assembly, M13 bacteriophage, nanorod, hybrid, colloidal molecule, tunable valency, star polymer.

The design of structured materials at the mesoscopic scale is a challenge that can be addressed with two main strategies usually referred as top-down and bottom-up approaches.^{1,2} While the top-down methods consist in the elaboration of patterns and in their progressive size reduction, the bottom-up approach requires the use of nano- or micro-scaled building blocks for which the self-assembly can be driven by entropic or enthalpic contributions allowing for producing hierarchical architectures.³ Specifically, most of reported studies have focused on sphere-based assemblies with specific sizes and/or functionalizations opening the field of so-called “colloidal molecules”.⁴⁻⁶ To go beyond the spherical symmetry and developing more complex architectures, some investigations have been performed using nanorods as elementary building blocks.⁷⁻¹¹ Mainly two distinct paths have been considered for creating multiarm colloidal molecules: the core-first and the arm-first approaches. In the former case, the core is a multivalent initiator from which the arms can be grown. In this way, multivalent-branched nanocrystals¹² or polymer stars can be obtained by a specific crystal growth or by the polymerization of monomers around the core.¹³⁻¹⁹ This method allows for a control over the length and/or the width of each constituent but limits the construction of objects to a specific valency and a tailored size. The second approach consists in the self-assembly of linear constituents into multivalent star- or flower-like structures. This technique requires an end-to-end assembly of the particles which can be achieved in different ways such as DNA templating,^{20,21} amphiphilic interactions,²²⁻²⁴ biorecognition^{7,9,25-27} or tip-linking reaction of linear polymer chains.^{28,29} In this paper, we focus on the end-to-end self-assembly of filamentous viruses and aim to obtain multiarm structures of tunable valency (*i.e.* variable number of arms). Such viral rod-like particles can be seen both as elementary building blocks monodisperse in size and shape, and as versatile scaffolds for biological engineering and chemical functionalization of their coat proteins.³⁰⁻³² Prior studies have reported the use of bacteriophages, mainly modified by phage display, that self-assemble into chains of various length,^{25,33} rings³⁴ or radial structures.^{9,10} These works are based on the genetic engineering of viruses with mutated tip proteins (minor proteins p3 and p9, corresponding respectively to the two extremities of the phage) onto which specific polypeptidic sequences are fused. The formation of chains or rings is then driven either by the complementarity of the involved polypeptidic sequences²⁵ or by the introduction of an external crosslinker.³⁴ Star-like structures were also achieved by using the affinity of biotin for streptavidin¹⁰ or by biorecognition of a specific motif Histidine-Proline-Glutamine (HPQ),³⁵ called Strep-tag,

with streptavidin coated nanoparticles.⁹ Specifically, a mutant called M13-AntiStreptavidin (M13AS), initially isolated through the screening of a phage display library, has been already used in templating hierarchically organized hybrid materials.^{9,36,37} Here, we study this M13AS mutant displaying Strep-tags at one end by first quantifying its affinity for streptavidin with the determination of its dissociation constant in solution, K_d . Because of the relatively high dissociation constant K_d found, limiting therefore the self-assembly efficiency for the formation of colloidally stable multiarm structures, we have developed a chemical alternative approach based on the biotinylation of cystein residues present at one tip (p3 proteins) of the so-called M13C7C bacteriophages. The protocol relies on the thiol based bioconjugation, and it has been optimized to be both highly specific (no other coat protein modified) and efficient (yield of about 92%). We then discuss a quantitative model accounting for the interaction with streptavidin of both the biologically and the chemically functionalized phages for various initial conditions. When exposed to a dispersion of streptavidin coated nanoparticles, biotinylated phages self-assemble into colloidally stable multiarm structures, as the affinity of streptavidin for biotin is several orders of magnitude higher than for Strep-tags. Moreover, these multiarm molecules display a tunable valency which can be continuously monitored by varying the relative molar excess of biotinylated phages and streptavidin activated nanoparticles. This approach makes also possible a second chemical functionalization of the phages by their body labeling with fluorescent dyes, allowing for the *in situ* observation by optical microscopy of their self-assembly into multiarm colloidal molecules.

RESULTS AND DISCUSSION

M13AS Binding Affinity and Biotinylation Yield of M13C7C-B

In our mixtures of M13 viruses (either AntiStreptavidin phages, M13AS or biotinylated phages, M13C7C-B) and streptavidin coated nanoparticles (NP) exhibiting q streptavidin molecules (Strep) per NP, the principle of mass conservation applied on virus and streptavidin species provides the two following relations:

$$[M13]_0 = [M13]_{free} + [M13]_{bound} \quad (1)$$

with $[M13]_0$ the initial virus concentration, $[M13]_{free}$ and $[M13]_{bound}$ the respective concentrations at equilibrium of free and bound (or reacted) viruses with streptavidin coated nanoparticles;

$$q \times [NP]_0 = (q \times [NP]_{free} + (q - n) \times [NP]_{bound}) + n \times [NP]_{bound} \quad (2)$$

where n is the number of viruses bound per NP ($1 \leq n \leq q$), $[NP]_0$ and $[NP]_{free}$ the respective initial and unreacted concentrations of nanoparticles, and $[NP]_{bound}$ the concentration of nanoparticles conjugated with at least one M13 virus (Fig. 1). The binding affinity of a ligand for a receptor is given by the dissociation constant, K_d , which results from the following equilibrium in solution:³⁸



and is defined as:

$$K_d \equiv \frac{[M13]_{free} \times [Strep]_{free}}{[M13]_{bound}} \quad (4)$$

where $[Strep]_{free} = q \times [NP]_{free} + (q - n) \times [NP]_{bound}$. Qualitatively, the lower the K_d value is, the more stable the complex is and thus the stronger the affinity. In the case of the interaction between biotin and streptavidin protein, K_d reaches a value of 10^{-15} M, considered the strongest non-covalent bond found in nature.³⁹ The Histidine-Proline-Glutamine (HPQ) motif is a well-known Strep-tag with however a lower affinity for streptavidin than biotin, typically found in the μ M range.³⁵ However, the affinity of M13AS phage where the HPQ motif is displayed on each of its five p3 proteins, has not yet been determined. Using Eqs. 1 and 2, let's rewrite K_d as a function of an unique variable, the fraction of bound nanoparticles $f(NP) \equiv [NP]_{bound}/[NP]_0$:

$$K_d = \left(\frac{[M13]_0}{n \times f(NP)} - [NP]_0 \right) \times (q - n \times f(NP)) \quad (5)$$

Thanks to Eq. 5, the M13AS-streptavidin dissociation constant, K_d , can be determined by counting by TEM both $f(NP)$ and n , the average number of viruses per nanoparticle having at least one virus bound (defined also as the valency of the self-assembled structure). Note that using this model, a precise estimation of K_d can only be performed if no steric

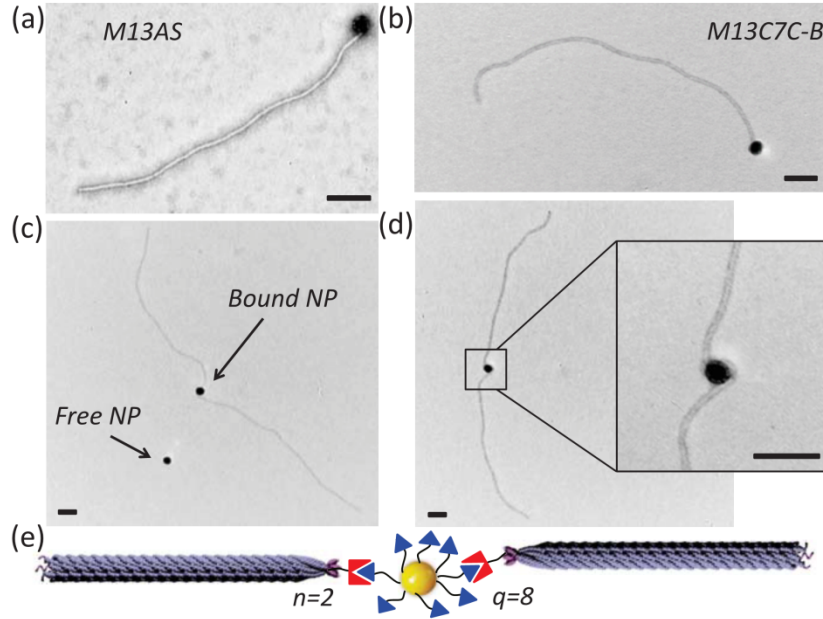


FIG. 1. Transmission electron microscopy (TEM) images of M13AS ((a) and (c)) and M13C7C-B ((b) and (d)) viruses complexed with streptavidin-coated nanoparticles (NP). (a),(b) Single viruses and (c),(d) pairs of viruses bound to a nanoparticle. The scale bars represent 100 nm. (e) Schematic representation of two viruses ($n = 2$) bound to a NP exhibiting $q = 8$ streptavidin proteins at its surface.

hindrance limits the binding of viruses to nanoparticles. This means practically that $n \ll q$, as experimentally confirmed in Fig. 2(a) and (b) for which $n \simeq 1.5$ (see Table I).

As M13AS viruses are in large excess compared to NP (see Table I), only the concentrations at equilibrium of free and bound NP as well as the average number of viruses grafted per NP, n , can be counted by TEM on a given sample ($[M13AS]_{free}$ being too high to be determined at the same time). In order to determine K_d , two specific mixtures of M13AS and streptavidin-coated nanoparticles (Samples **1** and **2**, described in Table I) were realized with different initial conditions, for which the molar excess is introduced, α :

$$\alpha \equiv \frac{[M13]_0}{[NP]_0} \quad (6)$$

Both mixtures were observed in TEM (Fig. 1) and the distributions of the number of viruses grafted per bead is provided in Fig. 2(a) and (b) for samples **1** and **2**, respectively. The mean values of n and $f(NP)$ are deduced from these distributions, and consequently

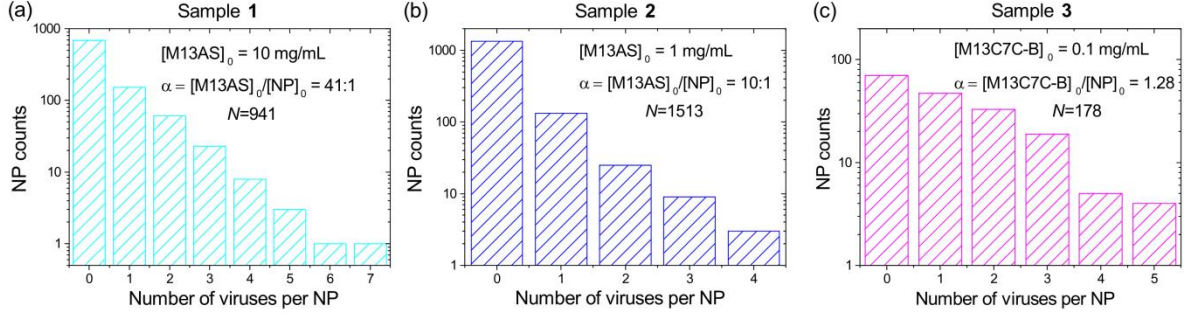


FIG. 2. Distribution of the number of bound viruses per nanoparticle in suspensions of (a) M13AS at initial concentration of 10 mg/mL (5.4×10^{-7} M) with a molar excess of virus per nanoparticle $\alpha = 41$ (Sample **1**), (b) $[M13AS]_0 = 1$ mg/mL (5.4×10^{-8} M) with $\alpha = 10$ (Sample **2**), (c) biotinylated viruses at $[M13C7C-B]_0 = 0.1$ mg/mL (5.4×10^{-9} M) with $\alpha = 1.28$ (Sample **3**). N indicates the total number of NP counted by TEM for establishing the statistics of each sample.

TABLE I. Summary of the experimental conditions and measurements obtained by TEM for the three mixtures of viruses and streptavidin coated nanoparticles. Samples **1** and **2** correspond to biologically engineered M13AS phages and sample **3** to tip-biotinylated M13C7C-B viruses. The fraction of bound nanoparticles, $f(NP)$, and the average number of viruses per bead, n , result from TEM counting shown in the distributions plotted in Fig. 2. The dissociation constant, K_d , is calculated for samples **1** and **2** according to Eq. 5, and is taken from literature³⁹ for sample **3**.

Sample	1	2	3
Virus	M13AS	M13AS	M13C7C-B
$[M13]_0$ (M)	5.4×10^{-7}	5.4×10^{-8}	5.4×10^{-9}
$[NP]_0$ (M)	1.3×10^{-8}	5.4×10^{-9}	4.2×10^{-9}
$\alpha = [M13]_0/[NP]_0$	41	10	1.28
$f(NP)$	0.27	0.11	0.61
n	1.62	1.31	1.94
K_d (M)	9×10^{-6}	3×10^{-6}	10^{-15}

K_d is obtained thanks to Eq. 5. A similar dissociation constant (within the experimental margin of error) $K_d = 6 (\pm 3) \times 10^{-6}$ M is found for both samples (Table I). This average value is also in good agreement with the one reported in literature for the Histidine-Proline-Glutamine Strep-tag of about 1 μ M.³⁵ The slightly lower binding affinity found in our case can be explained by the following reason: The determination of binding affinity is usually performed with the target compound (here: streptavidin) deposited on a solid surface, whereas our experiments were performed in bulk with dispersions of streptavidin coated NPs. These NPs not only diffuse slower than molecular streptavidin, but also induce steric hindrance as soon as some viruses are bound making more difficult further binding of other viruses. Nevertheless, this relative high value of the dissociation constant, for which $K_d \gg [M13AS]_0 \geq [NP]_0$ (Table I), does not allow for a tight and non-reversible binding. A first alternative would be to design a Strep-tag with an affinity in the nM range, providing then a suitable efficiency for high enough initial virus (> 1 mg/mL) and bead concentrations. The second alternative is to work with biotin derivatives ($K_d \simeq 10^{-15}$ M), which have been chemically grafted at one of the virus tips (see *Materials and methods*). In order to determine the biotinylation yield of the M13C7C-B phages, sample **3** has been prepared (Table I), where phages and streptavidin activated nanoparticles have been introduced in similar amount ($\alpha \simeq 1$), allowing for their simultaneous counting by TEM (Fig. 1). Specifically, among a total number of 229 counted viruses, 210 were bound by their tip to nanoparticles and 19 were found free, giving a fraction of bound M13C7C-B of $f(M13) = 0.92$ and therefore a yield of biotinylation of 92%. It is worth mentioning that the functionalization of the virus tips by biotin is not only efficient, but also highly selective as shown by the absence of any virus based by-products. Moreover, the specificity of the reaction between beads and functionalized phages has been checked by a control experiment with raw M13 viruses, and, as expected no interaction is observed with nanoparticles (see Figure S3 in Supporting Information).

Quantitative Model for the Formation of Virus/NP Structures

Rewriting the expression of K_d given in Eq. 5, the fraction of bound nanoparticles $f(NP)$ can be accounted by the following quadratic equation:

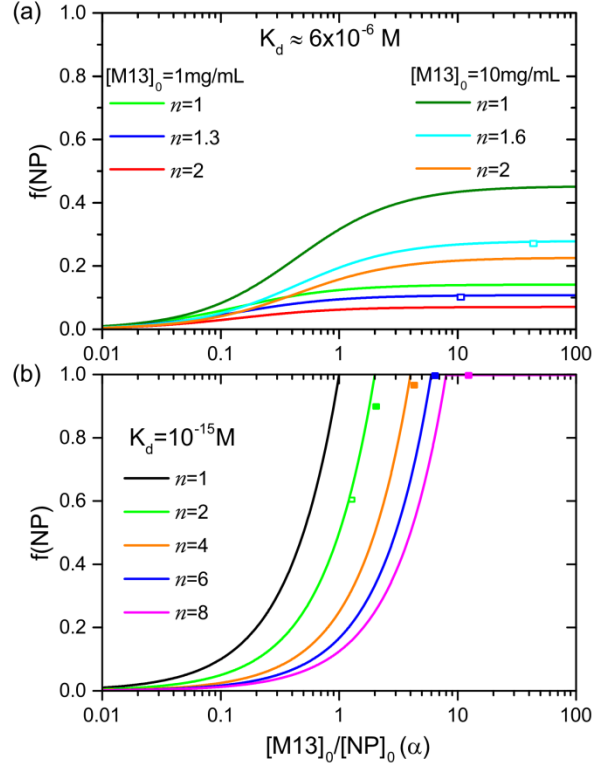


FIG. 3. Fraction of bound nanoparticles, $f(NP)$, as modeled by Eq. 7, as a function of the molar excess, α , obtained for different average numbers of viruses per NP, n . Results calculated for: (a) M13AS virus strain with $K_d \simeq 6 \times 10^{-6} \text{ M}$ for two different initial virus concentrations, $[M13AS]_0$; (b) biotinylated viruses, M13C7C-B, with $K_d = 10^{-15} \text{ M}$. In this case, the results are independent of the initial virus concentration, as $[M13AS]_0 \gg K_d$, and only depend on the molar excess α . The cyan, blue and green open square symbols represent the samples **1**, **2** and **3**, respectively, as described in Table I. The green, orange, blue and pink full square symbols represent the four experimental samples of respective average valency $n = 2.1, 4.2, 6.1$ and 8.3 , as reported in the next Section.

$$f(NP)^2 - \frac{1}{n} \left(\frac{\alpha K_d}{[M13]_0} + q + \alpha \right) f(NP) + \frac{q\alpha}{n^2} = 0 \quad (7)$$

Eq. 7 can be easily solved analytically to provide $f(NP)$ for different initial conditions. The results are plotted in Fig. 3. When the binding affinity for streptavidin is low, as for M13AS viruses, the self-assembly yield to form multiarm structures ($n \geq 2$) remains weak ($f(NP) < 25\%$), whatever the initial virus and NP concentrations (Fig. 3(a)). At a fixed

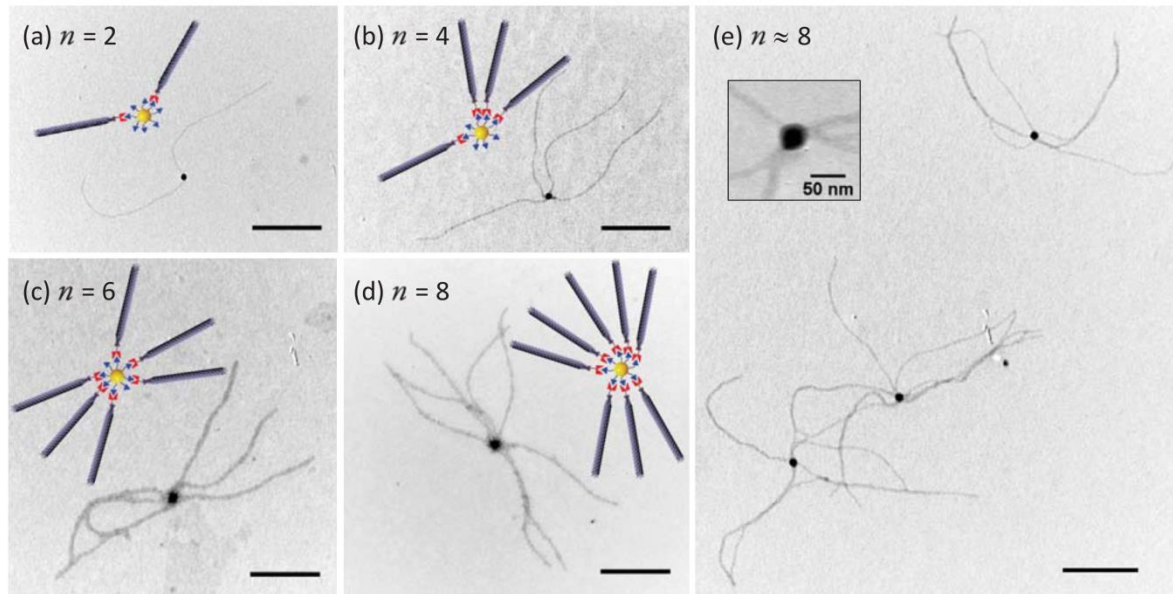


FIG. 4. Virus based multiarm self-assemblies observed by TEM obtained from the reaction between tip-biotinylated phages (M13C7C-B) and streptavidin coated nanoparticles. The number of arms can be continuously tuned, as illustrated with structures of valency $n = 2$ ((a), dimer), 4 ((b), tetramer), 6 ((c), hexamer) and 8 ((d), octamer). (e) Large field of view with three multiarm molecules of average valency $n \approx 8$. Inset: zoom-in of the multiarm structure core. Except in the inset, the scale bars represent 500 nm.

value of the dissociation constant K_d , only the initial conditions affect the equilibrium, as illustrated by the two experimental data points corresponding to samples **1** and **2**, which are in very good agreement with the predictions of the model. Fig. 3(b) shows that strongly increasing the binding affinity favors the formation of multiarm structures, for which a total reaction can be obtained. More importantly, the valency of multiarm self-assemblies can be controlled and tuned *only* by varying the molar excess α . Finally, an outstanding agreement between our model and sample **3** is found (Fig. 3(b)), especially considering the absence of any free parameter. In conclusion, our model quantitatively accounts for the self-assembly behavior of our two experimental systems, and it confirms that biotinylated phages are the most suitable one to form multiarm colloidal molecules, as described in the next paragraph.

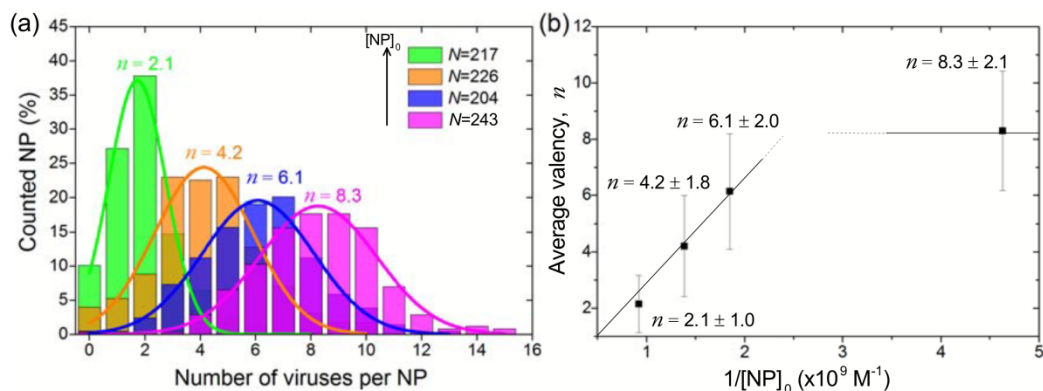


FIG. 5. (a) Distribution of the number of viruses per nanoparticle for four different samples, at fixed biotinylated virus concentration, $[M13C7C-B]_0$, and increasing nanoparticle concentration, $[NP]_0$. The arithmetic mean, or average valency n , is indicated and the solid lines correspond to Gaussian fits. N is the total number of NP counted by TEM for establishing the statistics of each sample. (b) The average valency n increases linearly with the molar excess, and saturates when n reaches the maximum number of available streptavidin proteins per NP, $q \simeq 8$. The error bars are the standard deviation obtained from the Gaussian fits.

Construction of Multiarm Colloidal Molecules

Multiarm colloidal molecules were achieved by preparing four samples of M13C7C-B phages mixed with aqueous dispersions of streptavidin coated nanoparticles (see *Materials and methods* section). As shown in Fig. 4 and in Supplementary Fig. 4, the rod-based colloidal molecules are radial structures possessing a single central NP surrounded by up to $n = 8$ arms formed by tip-linked M13C7C-B functionalized phages. Figure 5 displays the increase of the average valency n of multiarm assemblies when the initial concentration of NP is decreased at a fixed virus concentration. This behavior is *quantitatively* consistent with our theoretical model, as plotted in Fig. 3(b) where the full symbols represent the four samples of colloidal molecules reported in Fig. 5. We experimentally confirm that the molar excess is the key-parameter to tune the valency of the self-assemblies. After a linear increase, the average valency n saturates in Fig. 5(b) when it reaches the maximum number of available streptavidin binding sites per bead, q . At this saturated value, n becomes independent of the initial molar excess α (for $\alpha \geq q$), as predicted by the model (Fig. 3(b)). In the results shown in Fig. 5(a), all samples present a similar distribution of

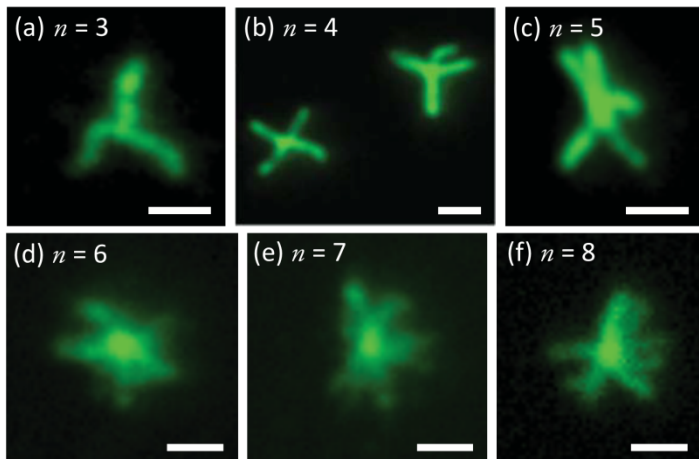


FIG. 6. Optical fluorescence microscopy images showing multiarm colloidal molecules formed by fluorescently labeled M13C7C-B phages. Different valencies, n , can be observed *in situ* in aqueous dispersions. The scale bar, identical for the six images, represents $1 \mu m$.

virus populations (except for the lowest average valency $n = 2.1$ which is asymmetric), whose width, defined as the standard deviation of the corresponding Gaussian fits, is δn 2. This width of the average valency is narrow enough to obtain slightly polydisperse (in terms of number of arms) batches of star-like colloidal molecules for the four different prepared samples (corresponding to the four different initial NP concentrations). Thanks to an efficient and regio-selective biochemical functionalization of the M13C7C phages followed by a conjugation with streptavidin activated beads, the large scale production of multiarm structures of well-defined and tunable valency has been achieved. Furthermore, biotinylated phages are an interesting system to work with because of their ability to be twice chemically modified without losing their functionality. We have succeeded in labeling with fluorescent dyes the virus body, targeting mainly the p8 major coat proteins. Labeled M13C7C-B phages can therefore be visualized at the single particle level by optical fluorescence microscopy (Fig. 6), allowing for *in situ*, *i.e.* at equilibrium, sample observation as shown in the movie presented in Supporting Information. If the structures are identical in shape to those seen by TEM (Fig. 4), information on the dynamics of the different multiarm structures are here available. Remarkably, some flexibility can be noticed between the arms of the self-assemblies, contrary for instance to multipod structures obtained by crystal growth.¹¹ This flexibility in the link between bound viruses is distinguishable from the Brownian motion

of the multiarm structures themselves. Such *in situ* observations provide the experimental equilibrium state of virus based multiarm structures.

CONCLUSIONS

In this paper, we have studied the self-assembly of functionalized filamentous viruses into multiarm colloidal structures. First, we used an engineered phage (M13AS), modified at one end to display a polypeptidic sequence (HPQ motif) exhibiting affinity for streptavidin. We determined the dissociation constant of the system in solution to be $K_d = 6 \times 10^{-6}$ M consistent with literature value for this protein tag. In order to strengthen the affinity for streptavidin, a selective and efficient biotinylation protocol of one of the phage tips has been successfully performed. When conjugated with streptavidin activated nanoparticles, these chemically modified phages self-assemble into colloiddally stable multiarm structures, whose valency has been continuously tuned from 1 to 8 by varying the molar excess. An additional chemical functionalization of the phage body by fluorescent dyes has been done to optically visualize the multiarm colloidal molecules at the single particle scale and to get *in situ* information on their dynamics. The results presented here show how regio-functionalized viruses can be used as building blocks for mesostructured materials and for the development of a next generation of rod based colloidal particles.

MATERIALS AND METHODS

M13-AntiStreptavidin phage presents Strep-tags on each of its five p3 proteins localized at one tip. M13AS was kindly provided by S.-W. Lee from the University of Berkeley (USA). M13AS was isolated through the screening of a phage display library and several rounds of selection for streptavidin, with the following inserted sequence on the p3 proteins, identified by DNA sequencing (see Figure S1 in Supporting Information for the complete sequencing): ACHHPQGPPCGGS.⁴⁰ The specific motif Histidine-Proline-Glutamine (HPQ),³⁵ called Strep-tag, is known for its affinity with streptavidin. Large amplification of these phages of molecular weight $M_w = 1.85 \times 10^7$ g/mol was performed using standard biological procedures.⁴¹ Before further use, M13AS phages were extensively dialyzed against PBS buffer (pH 7.5, I=20 mM).

A second filamentous phage, called M13C7C and displaying cystein residues on the exposed part of each p3 protein (cystein amino acids otherwise absent from the other coat proteins of the phage), has been used in this study and bioconjugated with maleimide activated biotin. Infecting solution was purchased from New England Biolabs (NEB, USA), and corresponds to a mixture of several M13C7C clones. The amino acid sequences inserted on each of the five p3 proteins of the viruses display 7 random amino acids flanked by two oxidized cysteins which form a disulfide bridge. After phage titration, we isolated a plaque consisting of a colony of bacteria infected by a single virus clone and thus a unique amino acid sequence (see Figure S2 in Supporting Information for the complete DNA sequencing). M13C7C phages were also grown and purified using standard biological protocols.⁴¹

In order to have free thiols available for conjugation with maleimide activated compounds, a reduction step of the disulfide bridges is required. This was done by introducing a reducing agent, as Tris(2-carboxyethyl)phosphine hydrochloride (TCEP, Thermo Scientific) used at a concentration around 2 mM.^{42,43} To prevent any re-oxidization of the free thiols and the reformation of the disulfide bridges, all the reaction process occurred in degassed media and in the presence of 1 mM of ethylenediaminetetraacetic acid (EDTA, Sigma Aldrich).⁴² The viruses were first depleted by the addition of 20 % (v/v) of a PEG-8000/NaCl mixture (200 g/L of PEG-8000, 2.5 M of NaCl, degassed), then redispersed in 50 mM Tris (+ 1 mM EDTA, degassed) to have a final concentration of about 1 mg/mL. The dispersion of phages in presence of TCEP was then stirred (400 rpm) at 4°C during 48 hours.^{31,44} After the reduction reaction, viruses were purified by a centrifugation step (13.5 kg during 20 minutes) followed by 6 rounds of 10 min dialysis against PBS buffer (pH 6.5, I=350 mM + 1 mM EDTA, degassed). Maleimide-PEG2-biotin (Thermo Scientific) was dissolved in distilled water (Maximum solubility: 25 mg/mL). A 1000-fold molar excess was taken per virus and added drop-wise to the suspension. The mixture was kept under inert atmosphere thanks to the initial bubbling of Argon, protected from light and stirred during 2 hours at room temperature. The resulting phages after biotinylation, called M13C7C-B, were then dialyzed against Bis-Tris (I=20 mM pH 7.4, 0.02% NaN3) and purified by rinsing with the same buffer in a 100k MWCO filter tube (Amicon Ultra, Merck Millipore).

The fluorescent labeling of the M13C7C-B was achieved in PBS buffer (pH 7.8, I = 350 mM) at a concentration of 0.2 mg/mL. An excess of 3 dyes (either Alexa488-NHS ester

activated, Molecular Probes, or Fluorescein-NHS ester) per p8 main coat protein (about 3000 proteins per virus) first dissolved in N,N-dimethylformamide (DMF) was added to the suspension. Particular care was taken that the proportion of DMF does not exceed 20% of the total volume in order to avoid any denaturation of the phages by the organic solvent. The mixture was protected from light and kept under stirring at room temperature during 2 hours. The resulting viruses were then extensively dialyzed against Bis-Tris buffer (pH 7.4, I=20 mM).

To construct multiarm structures with M13C7C-B as well as to estimate the binding affinity of M13AS with streptavidin, the viruses were mixed with 30 nm streptavidin coated iron oxide nanoparticles (Ocean NanoTech) for 14 hours at room temperature. The number of available streptavidin proteins per bead for conjugation with phages, q , is estimated to be of about 8 (maximum mean valency observed). Rather large nanoparticles have been chosen in order to make easier their counting by transmission electron microscopy (TEM) experiments. In particular, non-specific interactions between viruses can then be easily discriminated, especially when compared with the use of free molecular streptavidin whose relative small size makes tricky its observation by TEM. Note that some streptavidin release occurred with time due to nanoparticle aging (life time of 3 months).

Samples were then observed by TEM on a Hitachi H-600 microscope operating at 75 kV and images were recorded with an AMT CCD camera. The diluted virus suspension (typically 10^{-2} - 10^{-3} mg/mL) was settled onto freshly treated (O_2 plasma, K1050X, Quorum Technologies) 200-mesh formvar/carbon-coated grids (Agar) and stained with 2% (w/w) uranyl acetate.

The fluorescent labeled virus particles were visualized using an inverted microscope (IX-71, Olympus) equipped with high numerical aperture (NA) oil objective (100x PlanAPO NA 1.40, Olympus) and a Neo sCMOS camera (Andor).

ASSOCIATED CONTENT

Supporting Information: DNA sequencing of the two bacteriophages, large field of view images by TEM of the control experiment with raw viruses and of the multiarm structures, and movie of multiarm colloidal molecules observed by fluorescence microscopy.

AUTHOR CONTRIBUTIONS

E.G. designed the project and supervised the research. C.W. and A.C. prepared the biotinylated phages and studied their self-assembly, M.T. prepared the samples and performed the experiments on M13AS viruses, C.W. and A.R. performed the fluorescence microscopy experiments. E.G. and A.C. developed the theoretical model, and wrote the manuscript.

ACKNOWLEDGMENTS

This research was supported by the French National Research Agency (ANR) through the project AURORE. We thank Pr S.-W Lee for the generous gift of M13AS and P. van der Schoot for useful discussion. A.R. acknowledges support from the European Union's Horizon 2020 research and innovation programme under the Marie Skłodowska-Curie Grant Agreement No 641839.

* grelet@crpp-bordeaux.cnrs.fr

‡ These authors contributed equally to this work

- ¹ Mijatovic, D.; Eijkel, J. C. T.; van den Berg, A. Technologies for Nanofluidic Systems: Top-Down vs. Bottom-Up. A Review. *Lab Chip* **2005**, *5*, 492-500.
- ² Biswas, A.; Bayer, I. S.; Biris, A. S.; Wang, T.; Dervishi, E.; Faupel, F. Advances in Top-Down and Bottom-Up Surface Nanofabrication: Techniques, Applications & Future Prospects. *Adv. Colloid Interface Sci.* **2012**, *170*, 2-27.
- ³ Frenkel, D. Order Through Entropy. *Nat. Mater.* **2015**, *14*, 9-12.
- ⁴ van Blaaderen, A. Colloidal Molecules and Beyond. *Science* **2003**, *301*, 470-471.
- ⁵ Manoharan, V. N.; Elsesser, M. T.; Pine, D. J. Dense Packing and Symmetry in Small Clusters of Microspheres. *Science* **2003**, *301*, 483-487.
- ⁶ Wang, Y.; Wang, Y.; Breed, D. R.; Manoharan, V. N.; Feng, L.; Hollingsworth, A. D.; Weck, M.; Pine, D. J. Colloids with Valence and Specific Directional Bonding. *Nature* **2012**, *491*, 51-55.
- ⁷ Salant, A.; Amitay-Sadovsky, E.; Banin, U. Directed Self-Assembly of Gold-Tipped CdSe Nanorods. *J. Am. Chem. Soc.* **2006**, *128*, 10006-10007.

- ⁸ Figuerola, A.; Franchini, I. R.; Fiore, A.; Mastria, R.; Falqui, A.; Bertoni, G.; Bals, S.; Van Tendeloo, G.; Kudera, S.; Cingolani, R.; Manna, L. End-to-End Assembly of Shape-Controlled Nanocrystals *via* a Nanowelding Approach Mediated by Gold Domains. *Adv. Mater.* **2009**, *21*, 550-554.
- ⁹ Huang, Y.; Chiang, C.-Y.; Lee, S. K.; Gao, Y.; Hu, E. L.; De Yoreo, J.; Belcher, A. M. Programmable Assembly of Nanoarchitectures Using Genetically Engineered Viruses. *Nano Lett.* **2005**, *5*, 1429-1434.
- ¹⁰ Huang, F.; Addas, K.; Ward, A.; Flynn, N. T.; Velasco, E.; Hagan, M. F.; Dogic, Z.; Fraden, S. Pair Potential of Charged Colloidal Stars. *Phys. Rev. Lett.* **2009**, *102*, 108302, 1-4.
- ¹¹ Glotzer, S. C.; Solomon, M. J. Anisotropy of Building Blocks and Their Assembly into Complex Structures. *Nat. Mater.* **2007**, *6*, 557-562.
- ¹² Manna, L.; Milliron, D. J.; Meisel, A.; Scher, E. C.; Alivisatos, A. P. Controlled Growth of Tetrapod-Branched Inorganic Nanocrystals. *Nat. Mater.* **2003**, *2*, 382-385.
- ¹³ Cameron, D. J. A.; Shaver, M. P. Aliphatic Polyester Polymer Stars: Synthesis, Properties and Applications in Biomedicine and Nanotechnology. *Chem. Soc. Rev.* **2011**, *40*, 1761-1776.
- ¹⁴ Kennedy, J. P.; Jacob, S. Cationic Polymerization Astronomy. Synthesis of Polymer Stars by Cationic Means. *Acc. of Chem. Res.* **1998**, *31*, 835-841.
- ¹⁵ He, M.; Pang, X.; Liu, X.; Jiang, B.; He, J.; Snaith, H.; Lin, Z. Monodisperse Dual-Functional Upconversion Nanoparticles Enabled Near-Infrared Organolead Halide Perovskite Solar Cells. *Angew. Chem. Int. Ed.* **2016**, *55*, 4280-4284.
- ¹⁶ Xu, H.; Pang, X.; He, Y.; He, M.; Jung, J.; Xia, H.; Lin, Z. An Unconventional Route to Monodisperse and Intimately Contacted Semiconducting Organic-Inorganic Nanocomposites. *Angew. Chem. Int. Ed.* **2015**, *54*, 4636-4640.
- ¹⁷ Feng, C.; Pang, X.; He, Y.; Li, B.; Lin, Z. Robust Route to Unimolecular Core-Shell and Hollow Polymer Nanoparticles. *Chem. Mater* **2014**, *26*, 6058-6067.
- ¹⁸ Jiang, B.; Pang, X.; Li, B.; Lin, Z. Organic-Inorganic Nanocomposites *via* Placing Monodisperse Ferroelectric Nanocrystals in Direct and Permanent Contact with Ferroelectric Polymers. *J. Am. Chem. Soc.* **2015**, *137*, 11760-11767.
- ¹⁹ Yang, D.; Pang, X.; He, Y.; Wang, Y.; Chen, G.; Wang, W.; Lin, Z. Precisely Size-Tunable Magnetic/Plasmonic Core/Shell Nanoparticles with Controlled Optical Properties. *Angew. Chem. Int. Ed.* **2015**, *54*, 12091-12096.

- ²⁰ Dujardin, E.; Hsin, L. B.; Wang, C. R. C.; Mann, S. DNA-Driven Self-Assembly of Gold Nanorods. *Chem. Comm.* **2001**, *14*, 1264-1265.
- ²¹ Pal, S.; Deng, Z.; Wang, H.; Zou, S.; Liu, Y.; Yan, H. DNA Directed Self-Assembly of Anisotropic Plasmonic Nanostructures. *J. Am. Chem. Soc.* **2011**, *133*, 17606-17609.
- ²² Nie, Z.; Fava, D.; Kumacheva, E.; Zou, S.; Walker, G. C.; Rubinstein, M. Self-Assembly of Metal-Polymer Analogues of Amphiphilic Triblock Copolymers. *Nat. Mater.* **2007**, *6*, 609-614.
- ²³ Pang, X.; He, Y.; Jung, J.; Lin, Z. 1D Nanocrystals with Precisely Controlled Dimensions, Compositions, and Architectures. *Science* **2016**, *353*, 1268-1272.
- ²⁴ Jiang, B.; He, Y.; Li, B.; Zhao, S.; Wang, S.; He, Y.-B.; Lin, Z. Polymer-Templated Formation of Polydopamine-Coated SnO₂ Nanocrystals: Anodes for Cyclable Lithium-Ion Batteries. *Angew. Chem. Int. Ed.* **2017**, *56*, 1869-1872.
- ²⁵ Sweeney, R. Y.; Park, E. Y.; Iverson, B. L.; Georgiou, G. Assembly of Multimeric Phage Nanostructures Through Leucine Zipper Interactions. *Biotechnol. Bioeng.* **2006**, *95*, 539-545.
- ²⁶ Caswell, K. K.; Wilson, J. N.; Bunz, U. H. F.; Murphy, C. J. Preferential End-to-End Assembly of Gold Nanorods by Biotin-Streptavidin Connectors. *J. Am. Chem. Soc.* **2003**, *125*, 13914-13915.
- ²⁷ Gabryelczyk, B.; Szilvay, G. R.; Singh, V. K.; Mikkila, J.; Kostianen, M.A.; Koskinen, J.; Linder, M. B. Engineering of the Function of Diamond-like Carbon Binding Peptides through Structural Design. *Biomacromolecules* **2015**, *16*, 476-482.
- ²⁸ Schaeffgen, J. R.; Flory, P. J. Synthesis of Multichain Polymers and Investigation of their Viscosities. *J. Am. Chem. Soc.*, **1948**, *70*, 2709-2718.
- ²⁹ Pakula, T.; Vlassopoulos, D.; Fytas, G.; Roovers, J. Structure and Dynamics of Melts of Multiarm Polymer Stars. *Macromolecules* **1998**, *31*, 8931-8940.
- ³⁰ Molek, P.; Bratkovic, T. Bacteriophages as Scaffolds for Bipartite Display: Designing Swiss Army Knives on a Nanoscale. *Bioconjugate Chem.* **2015**, *26*, 367-378.
- ³¹ Ng, S.; Jafari, M. R.; Derda, R. Bacteriophages and Viruses as a Support for Organic Synthesis and Combinatorial Chemistry. *ACS Chem. Biol.* **2012**, *7*, 123-138.
- ³² Cao, B.; Yang, M.; Mao, C. Phage as a Genetically Modifiable Supramacromolecule in Chemistry, Materials and Medicine. *Acc. Chem. Res.* **2016**, *49*, 1111-1120.
- ³³ Hess, G. T.; Guimaraes, C. P.; Spooner, E.; Ploegh, H. L.; Belcher, A. M. Orthogonal Labeling of M13 Minor Capsid Proteins with DNA to Self-Assemble End-to-End Multiphage Structures.

- ACS Synth. Biol.* **2013**, *2*, 490-496.
- ³⁴ Nam, K. T.; Peelle, B. R.; Lee, S.-W.; Belcher, A. M. Genetically Driven Assembly of Nanorings Based on the M13 Virus. *Nano Lett.* **2004**, *4*, 23-27.
- ³⁵ Devlin, J. J.; Panganiban, L. C.; Devlin, P. E. Random Peptide Libraries: A Source of Specific Protein Binding Molecules. *Science* **1990**, *249*, 404-406.
- ³⁶ Lee, S.-W.; Lee, S. K.; Belcher, A. M. Virus-Based Alignment of Inorganic, Organic, and Biological Materials. *Adv. Mater.* **2003**, *15*, 689-692.
- ³⁷ Kim, W.-G.; Song, H.; Kim, Ch.; Moon, J.-S.; Kim K.; Lee, S.-W.; Oh, J.-W. Biomimetic Self-Templating Optical Structures Fabricated by Genetically Engineered M13 Bacteriophage. *Biosens. Bioelectron.* **2016**, *85*, 853-859.
- ³⁸ Sanders, C. R. *Biomolecular Ligand-Receptor Binding Studies: Theory, Practice and Analysis*, Vanderbilt University, 2010.
- ³⁹ Green, N. M. Avidin. *Adv. Protein Chem.* **1975**, *29*, 85-133.
- ⁴⁰ Yoo, S. Y.; Oh, J.-W.; Lee, S.-W. Phage-Chips for Novel Optically Readable Tissue Engineering Assays. *Langmuir* **2012**, *28*, 2166-2172.
- ⁴¹ Sambrook, J.; Russell, D. W. *Molecular Cloning: A Laboratory Manual*, 3rd Edition, Cold Spring Harbor Laboratory Press: New-York, 2001.
- ⁴² Rentero Rebollo, I.; Heinis, C. Phage Selection of Bicyclic Peptides. *Methods* **2013**, *60*, 46-54.
- ⁴³ Bellotto, S.; Chen, S.; Rentero Rebollo, I.; Wegner, H. A.; Heinis, C. Phage Selection of Photo-switchable Peptide Ligands. *J. Am. Chem. Soc.* **2014**, *136*, 5880-5883.
- ⁴⁴ Jafari, M. R.; Deng, L.; Kitov, P. I.; Ng, S.; Matochko, W. L.; Tjhung, K. F.; Zeberoff, A.; Elias, A.; Klassen, J. S.; Derda, R. Discovery of Light-Responsive Ligands through Screening of a Light-Responsive Genetically Encoded Library. *ACS Chem. Biol.* **2014**, *9*, 443-450.

Chapter 2

Reduction of disulfide groups at proximal end of M13C7C viruses by TCEP/iTCEP and labeling with maleimide activated fluorescent dyes

Contents

2.1 Introduction	54
2.2 Methods and results.....	56
2.2.1 TCEP as reductant	56
2.2.2 iTCEP as reductant	61
2.3 Conclusion.....	64
2.4 References	65

2.1 Introduction

Filamentous viruses are good model systems as colloidal rods and scaffolds for chemical functionalization and biological engineering. Compared to fd, M13 is more used for chemical modification because: (a) The wild type fd viruses are highly charged ($10\text{ e}^-/\text{nm}$) [1] which impedes the reaction with negative charged functional units (most proteins are negatively charged in water). In this case, M13 viruses that have 30% less charges are more preferable [2]. (b) A mutant of M13, called M13C7C, with a fused disulfide constrained (Cys–Cys) heptapeptide to the N-terminal of p3 protein that located at the proximal end, has been derived [3], [4] (Figure 1a, Figure 2a). There are 4 more disulfide bridges on p3 protein, but they are not located at the extreme end of the protein. Therefore, for bioconjugation, they may not be as efficient as the fused disulfide. This inserted disulfide group provides therefore very efficient passway to achieve local chemical modification at the proximal end of filamentous viruses.

In Chapter 1, we presented the biotinylation on the proximal end of M13C7C viruses exploiting the reaction between thiols and maleimide activated compounds. Beforehand, a reduction has to be performed on disulfide groups to form thiols (thiolation), as shown in Figure 1b, which is an important step to get high yield in the global biotinylation procedure. Therefore, in this chapter we present the investigation on optimizing the thiolation by using mobile Tris(2-carboxyethyl)phosphine (TCEP) or immobilized Tris(2-carboxyethyl)phosphine (iTCEP) as reductants.

Several compounds have been reported as reagents to reduce disulfides, such as Dithiothreitol (DTT) [5] and Beta-mercaptoethanol (BME) [6]. In this chapter, TCEP is chosen due to its main features: the ability to selectively reduce disulfide bonds in wide pH range, good water solubility and resistance to air oxidation. It has been widely used in reduction of alkyl disulfides [7]–[9] including M13C7C viruses [10], [11]. But the thiols produced after reduction can still crosslink with each other because of reoxidation if they are not properly stabilized in a reducing environment. Indeed, we have evidenced that the viruses tip-linked with each other, forming star-like structures (Figure 2b), owing to the crosslinking of thiols belonging to different viruses. The tip-linking ratio increases with the virus concentration which impedes further biotinylation. Note that we have to perform the reduction at a higher concentration ($\sim 1\text{ mg/mL}$) compared to other reported studies [10]–[12], due to the amount of materials needed for

further self-assembly experiments. So the purpose of this chapter is to explore the optimal conditions for thiolation and bioconjugation steps. Several aspects, like TCEP concentration, virus concentration and reaction time, have been explored.

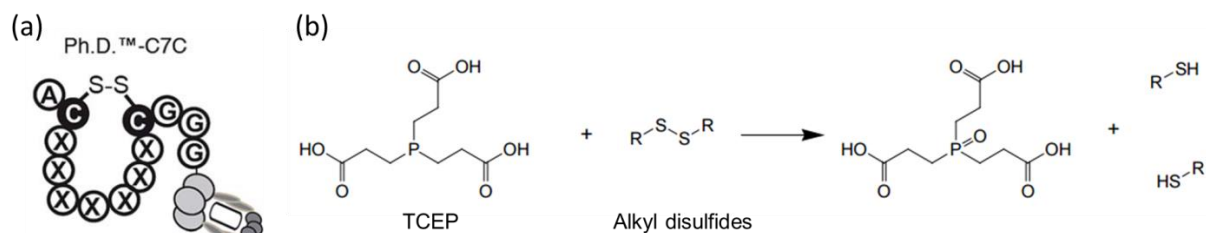


Figure 1: (a) Illustration of M13C7C virus with a fused disulfide constrained (Cys–Cys) heptapeptide at the proximal end. (b) Chemical reduction (thiolation) of alkyl disulfides by TCEP.

As mentioned, except for the inserted disulfide located at the very end of p3 protein, there are 4 more disulfides existing in p3 protein. They are not as exposed as the fused one, but can still react with the mobile TCEP. In order to increase the selectivity, immobilized TCEP (iTCEP), with TCEP covalently grafted to cross-linked agarose beads (diameter of tens of μm), is also used as reducing agent. The iTCEP gel is supposed to only react with the very exposed disulfide group, i.e., the inserted one, which makes the reduction more regio-selective and the maleimide–thiol reaction possibly more efficient. Additionally, from an experimental process point of view, iTCEP can be more conveniently removed by centrifugation. A further conjugation of maleimide activated fluorescent dyes to the resulting thiols is performed to characterize the thiolation efficiency.

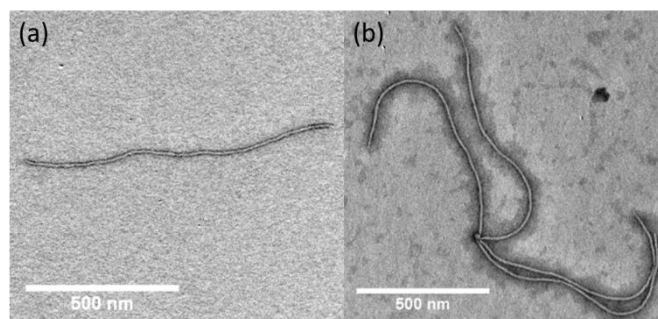


Figure 2: Transmission electron microscopy (TEM) images of (a) single M13C7C virus and (b) tip-linked M13C7C viruses. This cross-linking is caused by reoxidation of thiols after the reduction of disulfides by TCEP.

2.2 Methods and results

2.2.1 TCEP as reductant

Conditions for reduction of the disulfides (thiolation) by TCEP are optimized based on the existing studies [10]–[13]. Note that TCEP is often prepared and used as a hydrochloride salt, so we refer TCEP to its salt form, i.e., TCEP·HCl (CAS: 51085-45-9), which is purchased from Pierce. Here we discuss the main aspects to mainly influence the yield of the reaction.

(a) TCEP concentration and Buffer

In principle, higher TCEP concentration gives better efficiency of the reduction. But the pH of the suspension will be significantly affected by the TCEP, because TCEP is trivalent with three carboxyl acids. In reported papers, mainly two concentrations of TCEP are applied: 1 and 10 mM [13], [14]. We test the pH of several buffers in presence of 1 and 10 mM TCEP, including PBS, MES and Tris buffers, and choose the buffer according to its ability to maintain the pH. The corresponding results are shown in Table 1:

Table 1: pH of different buffers in presence of 1 and 10 mM TCEP.

	No TCEP	+ 1 mM TCEP	+10 mM TCEP
Tris·HCl buffer ^a	8.2	7.6	4.0
Tris (without HCl) ^b	10.1	8.7	7.1
PBS buffer ^c	6.5	6.4	5.5
MES buffer ^d	6.2	6.0	4.2

^aTris·HCl buffer: 50 mM Tris, pH 8.2, I = 25 mM, pK_a = 8.2; ^bTris (without HCl): 50 mM Tris [12]; ^cPBS buffer: 100 mM PBS, 100 mM NaCl, pH 6.5, I = 350 mM, pK_{a1} = 2.15, pK_{a2} = 7.2, pK_{a3} = 12.33; ^dMES buffer: 50 mM MES, pH 6.2, I = 225 mM, pK_a = 6.2.

According to the results shown in Table 1, pH of the buffers after adding 10 mM TCEP decreases a lot, which means the buffers lost their ability to maintain pH in this case. With 1 mM TCEP, variations of pH are less significant. Also our previous experiments showed that the thiolation of M13C7C at conditions of 10 mM TCEP, 42 °C, around 30% of viruses are tip-linked. So the TCEP concentration is settled to 1 mM, which is also consistent to the value given by Heinis [10] and Derda [11].

In order to increase the colloidal stability of the viruses, it's better to keep them in highly charged state. Since M13C7C viruses are negatively charged with an isoelectric point (pI) of 4.5, high pH can thus increase the charge density of the viruses and enhance the electrostatic repulsion between each other, and consequently, improve their colloidal stability. In addition, TCEP shows better rate of reduction at relative high pH [7], [15]. For this reason, we use 50 mM Tris (without HCl) as the buffer, which gives a final pH 8.7 (suitable for the reaction) after adding 1 mM TCEP.

(b) Reaction temperature and virus concentration

The temperature for thiolation is chosen between two different values based on existing studies: 42 °C [10] and room temperature (22 °C) [11]. After the reaction, both samples were incubated in ice for 5 min, which may decrease the tip-linkage for thiolation at 42 °C, as the p3 proteins is expected to unfold at 42 °C. There are four more disulfides on each p3 protein, and three of them are buried deeply. These disulfide groups could be exposed to the solvent at 42 °C due to unfolding and be reduced to thiols by TCEP, which increases the possibility of crosslinking. In this case, incubation on ice could refold the p3 protein and reduce tip-linking between viruses. No effect of ice incubation has been found on thiolation of viruses at room temperature, since the p3 proteins are supposed to be folded all the time.

The other parameters we applied for thiolation were: Concentration of M13C7C was settled to be ~ 1 mg/mL, given by the final concentration we needed; reaction time was 1 hour which is in principle enough for the reduction according to the existing literature [10], [11], [13], [14]; after the reduction, the buffer was changed by dialysis to PBS (I = 350 mM, pH 6.5) both to remove the TCEP and to have the optimal ionic strength and pH for reaction with maleimide activated compounds. This dialysis was performed at 4 °C for 1 h with buffer replacements every 10 min [16]. The thiolated viruses were kept in PBS buffer for 36 hour to check the time evolution. Percentages of the tip-linked viruses at each step were characterized by transmission electron microscopy (TEM), results for thiolation at 22 °C and 42 °C are summarized in Table 2 and Table 3.

Table 2: Percentages of single/tip-linked M13C7C after reduction by TCEP at 22 °C *, measured by TEM.

	<i>Initial</i>	<i>Cooling on ice after 5 min</i>	<i>Dialyzing against PBS after 1 hour</i>	<i>36 h after dialysis</i>
Counted viruses	209	189	190	214
Singles	98% ± 1%	91% ± 2.1%	86% ± 2.5%	77% ± 2.9%
Tip-linked	2% ± 1%	9% ± 2.1%	14% ± 2.5%	23% ± 2.9%

* Error bars are defined by standard error of random samples, calculated by $\sqrt{P(1-P)/n}$, where P is the percentage of the component, n is the total counts.

Table 3: Percentages of single/tip-linked M13C7C after reduction by TCEP at 42 °C *, measured by TEM.

	<i>Initial</i>	<i>Cooling on ice after 5 min</i>	<i>Dialyzing against PBS after 1 hour</i>	<i>36 h after dialysis</i>
Counted viruses	209	173	259	230
Singles	98% ± 1%	96% ± 1.5%	81% ± 2.4%	53% ± 3.3%
Tip-linked	2% ± 1%	4% ± 1.5%	19% ± 2.4%	47% ± 3.3%

* Error bars are defined by standard error of random samples, calculated by $\sqrt{P(1-P)/n}$, where P is the percentage of the component, n is the total counts.

Both results of reactions at 22 °C and 42 °C show that more than 90% thiolated viruses remain in single state after cooling on ice. It means that in the presence of TCEP, during the 1 hour reaction, there is no crosslinking between thiolated viruses. After dialyzing against PBS buffer, TCEP is removed from the suspension. Without TCEP, thiols at the proximal ends of M13C7C viruses can be reoxidized slowly by oxygen in the air, leading to tip-linking. The sample reduced at 42 °C shows faster tip-linking rate with time. So room temperature is chosen for the thiolation. In fact, lower temperature, like 4 °C, can be used as long as we don't unfold p3 protein. For example, when TCEP are used as control experiment of iTCEP, the thiolation is performed at 4 °C.

Besides, we observe very small amount of broken viruses (< 1%) after thiolation of M13C7C by TCEP at 42 °C. We believe that 42 °C is really “harsh condition”, as mentioned by Heinis [10], that may break the virus due to side reaction [17].

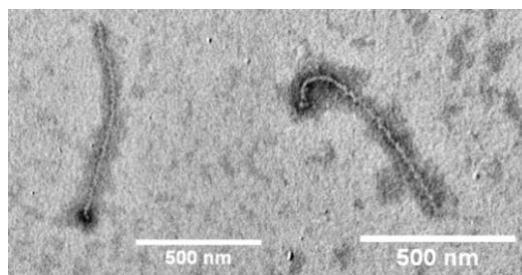


Figure 3: TEM images of short (broken) M13C7C observed after reduction by TCEP at 42 °C.

Another possible reason that could form cross-linkage between virus tips is hydrophobic interaction. Since TCEP can break disulfide bridges which is important for folding of proteins, the hydrophobic peptides will be exposed to the solvent and thus may lead to hydrophobic interaction between virus tips. In order to check whether hydrophobic interaction exists, we avoid reoxidation by maintaining fresh TCEP in the solution. Additionally, PBS buffer is substituted by Tris because PBS may oxidize TCEP [18]. This is achieved by dialyzing the virus suspension against 1 mM fresh TCEP (in 50 mM Tris) after the reaction. The effect of virus concentration is also tested by depletion (depletion could increase the virus concentration to hundreds of mg/mL locally (viruses in bundles) which favors a lot the cross-linking between viruses). The procedure is described as: 1 mM TCEP was mixed with 1 mg/mL M13C7C viruses in 50 mM Tris solution, with a 300 rpm stirring at 22 °C. After 1 hour thiolation, the mixture was dialyzed against fresh 50 mM Tris in presence of 1 mM TCEP. In this case, the thiolated viruses will stay in reduced state. TEM grids were prepared to check the percentage of tip-linked M13C7C viruses with time. Then the concentration of viruses was increased strongly to hundreds of mg/mL by depletion, and diluted by the same 50 mM Tris (with 1 mM TCEP) to 10 mg/mL and then 1 mg/mL. Depletion of viruses was performed by adding (2.5 M NaCl, 20% PEG 8K) to the sample. Percentages of tip-linked viruses were also checked after depletion and after diluting to virus concentrations of 10 and 1 mg/mL. Results are presented in Figure 4.

After refreshing the thiolated viruses with new TCEP, 89% single viruses are observed, and this number still increases slightly with time, which means that adding TCEP prevents the thiols from oxidation and therefore avoids virus tip-linking. The high percentage of single M13C7C indicates that the reduced viruses have a good colloidal stability at 1 mg/mL concentration in presence of TCEP. We can also conclude that the hydrophobic interaction by unfolding of p3

protein in presence of TCEP is not the reason of tip-linkage, otherwise we should obtain more cross-linked viruses with time.

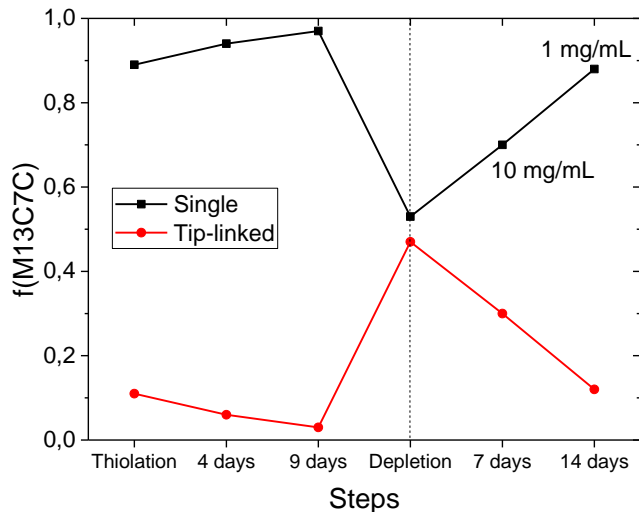


Figure 4: Fractions of single and tip-linked viruses in different steps. Black squares represent single viruses and red circles represent tip-linked viruses. Dashed line indicates a concentration step. Virus concentrations shown in the figure are after redispersing the virus pellet in 50 mM Tris buffer in presence of 1 mM TCEP. Numbers of counted viruses for all steps are more than 200.

On the other hand, increasing the virus concentration by depletion (to hundreds of mg/mL) creates about 50% tip-linked viruses. This percentage reduces by decreasing the virus concentration. When concentration is decreased to 10 mg/mL (by diluting in 50 mM Tris with 1 mM TCEP), the tip-linked viruses will be disassembled partially, resulting in only around 30% tip-linked viruses, as shown in Figure 4. This value further decreases to about 20% when the viruses are diluted to 1 mg/mL (with 1 mM TCEP). Here we proved that the ratio of cross-linked viruses depends on virus concentration. So, in order to avoid any cross-linking, we should keep it at ~ 1 mg/mL where we can have about 90% free M13C7C viruses.

In conclusion, the conditions for thiolation of M13C7C viruses by TCEP are optimized for: 1 mM TCEP for reduction of disulfide at the proximal end of M13C7C in a buffer of 50 mM Tris, which maintains the pH at relative high value and favors the colloidal stability of viruses and the reduction rate. Temperature should stay low to avoid unfolding of p3 proteins. Room temperature (22 °C) or lower (such as 4 °C) is suitable for the thiolation. Then, a reducing environment could inhibit the tip-linking, because it prevents the thiols to be reoxidized,

especially at low virus concentration. Finally, high concentration of viruses increases the ratio of tip-linking, thus a value around 1 mg/mL is suggested, since the cross-linking of viruses can be minimized to less than 10%.

The limitation of using the soluble mobile TCEP is that we may reduce other disulfide bonds buried under protein. Except for the fused cysteines which is inserted, the next one located at 7th position of N-terminal (Figure 5), can still be reduced by TCEP. This side-reaction can decrease the specificity of the reduction. In order to perform this thiolation of M13C7C in a controlled way, the immobilized TCEP that only have access to the exposed disulfide group is employed.

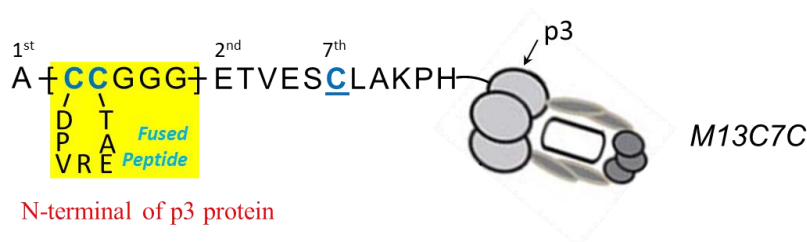


Figure 5: Illustration of the specific M13C7C strain used in this thesis. Fused peptide containing two cysteines that form a disulfide is inserted between 1st and 2nd amino acid, and highlighted in yellow. The next cysteine that can be exposed is located at 7th position in p3 protein.

2.2.2 iTCEP as reductant

The iTCEP, short for immobilized TCEP disulfide reducing gel, is purchased from Pierce. The protocol for using iTCEP refers to Derda [11], which used iTCEP of an effective concentration of 1.6 mM. Reduction was conducted at 4 °C for 60 hours. The reaction time is longer than what we used for TCEP in Section 2.2.1, because the iTCEP diffuses much less than the mobile one. After reaction, iTCEP can be removed simply by centrifugation at 10000 g, which is more convenient than TCEP (dialysis required). For quantitative comparison, reduction by TCEP was performed in the same conditions: temperature 4 °C, virus concentration 1 mg/mL, TCEP concentration 1.6 mM, and reaction time 60 hours. In addition, the thiolated viruses after were reacted with maleimide activated fluorescent dyes to characterize the yield of thiolation, since we could determine the number of reacted dyes per virus by spectrophotometry. Therefore, after the thiolation by iTCEP or TCEP, virus suspension were centrifuged (to remove iTCEP)

and/or dialyzed against PBS buffer ($I = 350$ mM, pH 6.5) at 4 °C, to be ready for the following fluorescent labeling of virus proximal tips. For the labeling, a typical molar excess of 200 dyes (Dylight™ 550 maleimide) per viruses first dissolved in N,N-dimethylformamide (DMF) was mixed with 1 mg/mL thiolated viruses. The mixture was protected from oxygen and light by filling the container with Argon and covering it with Aluminum foil. The maleimide–thiol reaction was conducted under stirring of 300 rpm at room temperature for 2 h. The obtained labeled viruses were pelleted by ultracentrifugation to remove the unreacted dyes, and then redispersed in Bis-Tris buffer ($I = 20$ mM, pH 7.0) with 1 mM TCEP. We checked the states of viruses by TEM at different steps, including: after reduction, after dialysis against PBS buffer, after labeling (removal of the free dyes), after redispersing to 1 mg/mL, and after adding 1 mM TCEP to create reducing environment. The percentages of free and tip-linked viruses are summarized in Figure 6.

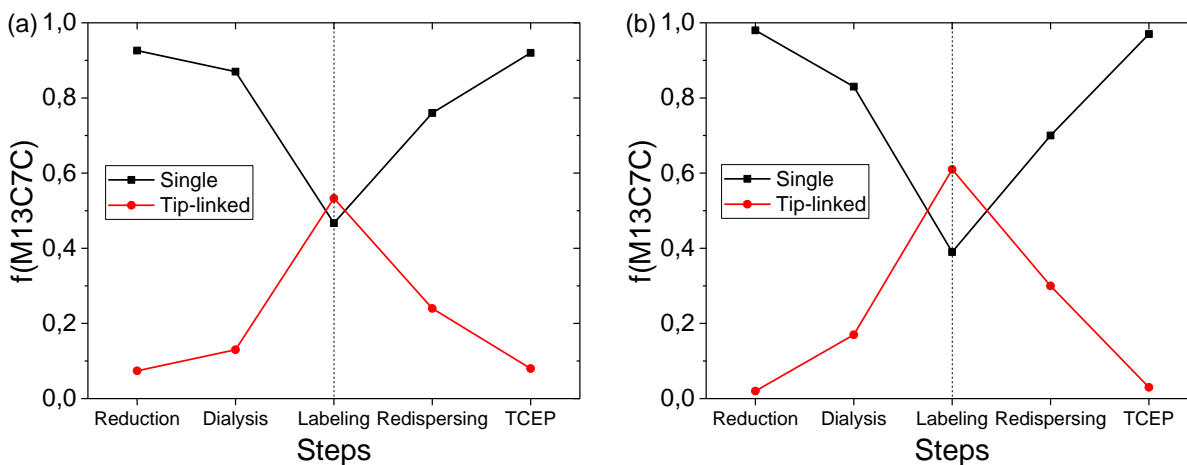


Figure 6: Fractions of single and tip-linked viruses in different steps during the labeling processes with (a) iTCEP and (b) TCEP as reductants. Black squares represent fractions of single viruses, and red circles represent fractions of tip-linked viruses. Dashed lines in both figures indicate the labeling comprises of an ultracentrifugation step. Numbers of counted viruses for all steps are more than 200.

The results for iTCEP and TCEP show same trends. During the reduction process, most M13C7C viruses stay free, with only less than 10% which are tip-linked, because the reducing environment provided by iTCEP/TCEP prevents the cross-linking. After the change of buffer to PBS, no TCEP exists anymore in the suspensions. Oxidation can thus occur slowly with time and lead to increase of tip-linking. The percentage of tip-linked viruses dramatically raises up

after labeling, because the viruses are much more concentrated due to the ultracentrifugation step which aims to remove the free ungrafted dyes in excess. As discussed in Section 2.2.1, high concentration is one important reason for cross-linking. Therefore, about half viruses are tip-linked at this step. The tip-linked star-like structures can be partially disassembled by diluting the virus suspension. Fractions of tip-linked viruses decrease to about 20~30% when the viruses are diluted to 1 mg/mL. And this value can still be decreased to less than 10% by adding TCEP. Finally, in both case of iTCEP and TCEP, we succeed to keep about 90% viruses from being tip-linked. No significant difference is found between iTCEP and TCEP in terms of efficiency to avoid tip-linking between viruses.

However, a successful thiolation does not only depend on amount of free viruses we obtained, but also on the yield of the reaction with maleimide activated compounds afterwards. Thus, labeling with maleimide activated fluorescent dyes after thiolation was performed. Thanks to spectrophotometry, we are able to determine the number of dyes per virus labeled on their tips and thus quantify the efficiency of thiolation. Characterization part was done by A. Repula, PhD student in our group. As a result, an average of about 10 dyes are labeled per virus tip using iTCEP as reductant, and only about 3 dyes for TCEP. Detailed procedures and analysis will be shown in his thesis. We conclude that iTCEP as the reductant shows better thiolation efficiency than TCEP, especially considering that only exposed disulfide group can be labeled when thiolation is by iTCEP.

Note that maleimide group can also react with primary amine. However, the efficiency is about 1000 times less than thiols [19]. The number of primary amines on the surface of M13C7C viruses is hundreds times more than the thiols (~3000 of -NH₂ comparing to ~20 of -SH per virus), which means maleimide may react on the body of viruses (with p8 proteins). Therefore, to confirm the fluorescent dyes are indeed labeled at the virus ends, we observe these tip-labeled viruses in smectic phase by fluorescence microscopy. Tracer amount of body labeled viruses with green dyes are mixed to show the arrangement of viruses in the structure. Results are shown in Figure 7.

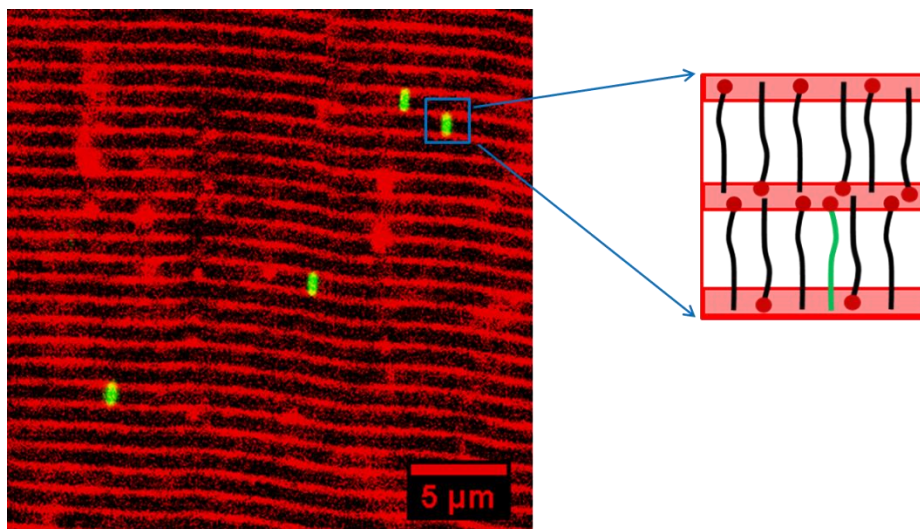


Figure 7: Fluorescent image of the tip-labeled M13C7C viruses in smectic phase and corresponding schematic representation. The red dyes at virus tips emphasize interlayer spacing. The low fraction of body labeled green viruses added in the matrix of tip-labeled viruses shows that viruses are orientated normal to the layers and confirms a smectic A phase.

We observe clear layers of red fluorescent dyes, and in between there are 4 single viruses fully labeled with green dyes normal to the layers. Position and direction of the green viruses indicates the formation of Smectic A phase. The existence of layers of red dyes demonstrates that the red dyes are labeled only at tips of viruses, as shown in the scheme in Figure 7. Also, it proves that the maleimide groups are highly selectively reacted to thiols even though primary amines are in big excess. Overall, we have proven here that a successful tip-labeling has been achieved.

2.3 Conclusion

We optimized the thiolation of M13C7C by TCEP to avoid tip-linking of viruses. 1 mM TCEP is used accompanied by a buffer of 50 mM Tris to maintain the pH at relative high value, which favors the reduction rate of TCEP and the colloidal stability of viruses. The temperature is settled at room temperature (22 °C) or lower, to avoid unfolding of p3 proteins. The tip-linking ratio increases with virus concentration. Thus concentration of 1 mg/mL where about 90% viruses are single (in presence of TCEP) is suggested. Immobilized TCEP (iTCEP) has been shown to be better reducing reagent for thiolation, as it only reacts to the exposed disulfide groups, which indicates a better regio-selectivity. Besides, the iTCEP is much more convenient

to purify (by centrifugation) comparing to TCEP (by dialysis). Even though the percentage of tip-linking after iTCEP reduction has similar trend to TCEP, the following labeling with maleimide activated dyes clearly exhibits better thiolation efficiency, because about 10 dyes are labeled with iTCEP, but only 3 dyes for TCEP. By showing fluorescent layers of dyes, we also proved that with the high selectivity of maleimide to thiols, the fluorescent dyes are only grafted at the virus tips.

2.4 References

- [1] K. Zimmermann, H. Hagedorn, C. C. Heuck, M. Hinrichsen, and H. Ludwig. The ionic properties of the filamentous bacteriophages Pf1 and fd. *J. Biol. Chem.*, 1986, 261: 1653–1655.
- [2] A. Lyubartsev, J. Tang, P. Janmey, and L. Nordenskiöld. Electrostatically Induced Polyelectrolyte Association of Rodlike Virus Particles. *Phys. Rev. Lett.*, 1998, 81: 5465–5468.
- [3] F. Huang *et al.* Pair potential of charged colloidal stars. *Phys. Rev. Lett.*, 2009, 102: 108302.
- [4] C. Mao *et al.* Virus-Based Toolkit for the Directed Synthesis of Magnetic and Semiconducting Nanowires. *Science*, 2004, 303: 213–217.
- [5] W. Konigsberg. Reduction of Disulfide Bonds in Proteins with Dithiothreitol. *Methods Enzymol.*, 1972, 25: 185–188.
- [6] J. C. Bardwell, K. McGovern, and J. Beckwith. Identification of a protein required for disulfide bond formation in vivo. *Cell*, 1991, 67: 581–589.
- [7] W. R. Gray and W. R. Gray. Disulfide structures of highly bridged peptides : A new strategy for analysis Disulfide structures of highly bridged peptides : A new strategy for analysis. *Protein Sci.*, 1993, 2: 1732–1748.
- [8] T. G. Senkevich, C. L. White, E. V Koonin, and B. Moss. A viral member of the ERV1/ALR protein family participates in a cytoplasmic pathway of disulfide bond formation. *Proc. Natl. Acad. Sci.*, 2000, 97: 12068–12073.
- [9] J. Wu and J. T. Watson. A novel methodology for assignment of disulfide bond pairings in proteins. *Protein Sci.*, 1997, 6: 391–398.
- [10] I. Rentero Rebollo and C. Heinis. Phage selection of bicyclic peptides. *Methods*, 2013, 60: 46–54.
- [11] S. Kalhor-Monfared *et al.* Rapid Biocompatible Macrocyclization of Peptides with Decafluorosulfone. *Chem. Sci.*, 2016, 9: 1–6.
- [12] M. R. Jafari *et al.* Discovery of light-responsive ligands through screening of a light-responsive genetically encoded library. *ACS Chem. Biol.*, 2014, 9: 443–450.
- [13] S. Bellotto, S. Chen, I. Rentero Rebollo, H. A. Wegner, and C. Heinis. Phage selection of photoswitchable peptide ligands. *J. Am. Chem. Soc.*, 2014, 136: 5880–5883.
- [14] E. Pretzer and J. E. Wiktorowicz. Saturation fluorescence labeling of proteins for proteomic analyses. *Anal. Biochem.*, 2008, 374: 250–262.
- [15] P. D. Tzanavaras, C. Mitani, A. Anthemidis, and D. G. Themelis. On-line cleavage of disulfide bonds by soluble and immobilized tris-(2-carboxyethyl)phosphine using sequential injection analysis. *Talanta*, 2012, 96: 21–25.

- [16] D. Montalvan-Sorrosa, J. L. González-Solis, J. Mas-Oliva, and R. Castillo. Filamentous virus decoration with gold nanoparticles: global fingerprints of bionanocomposites acquired with SERS. *RSC Adv.*, 2014, 4: 57329–57336.
- [17] P. Liu *et al.* A Tris (2-Carboxyethyl) Phosphine (TCEP) Related Cleavage on Cysteine-Containing Proteins. *J. Am. Soc. Mass Spectrom.*, 2010, 21: 837–844.
- [18] J. C. Han and G. Y. Han. A procedure for quantitative determination of tris(2-carboxyethyl)phosphine, an odorless reducing agent more stable and effective than dithiothreitol. *Anal. Biochem.*, 1994, 220: 5–10.
- [19] G. T. Hermanson. *Bioconjugate Techniques*, 3rd ed. Academic Press, 2013.

Chapter 3

Introducing patchiness to the tip of rod-like viruses by grafting metallic nanoparticles

Contents

3.1	Introduction	68
3.2	Materials and Methods.....	69
3.3	Results and Discussion.....	74
3.3.1	Influence of M13 virus strains on the reaction with AuNBs	74
3.3.2	Improvement of the binding between M13 viruses and AuNBs by TCEP	77
3.3.3	Influence of metal species on the nanoparticle-M13 reaction.....	78
3.3.4	Roles of capping reagent and ionic strength on the reaction between M13C7C and AuNBs	81
3.3.5	Influence of molar excess on the reaction between M13C7C and AuNBs	87
3.4	Conclusions	88
3.5	References	88

3.1 Introduction

We have introduced streptavidin-biotin interaction between nanoparticles and proximal end of the filamentous viruses to create colloidal molecules in Chapter 1. This method requires a pre-step of biotinylation of the p3 proteins of the viruses. M13C7C viruses with exposed disulfide groups at the end of p3 proteins are employed, since the disulfides can be reduced to thiols by TCEP/iTCEP and then react with maleimide activated biotin. The star-like colloidal molecules are therefore assembled by biotinylated M13C7C viruses and streptavidin coated nanoparticles. However, the whole process is intricate, especially the reduction of disulfides by TCEP/iTCEP (see Chapter 2). The formed thiols are easily reoxidized and cause cross-linking between viruses. In addition, we observed the release of streptavidin with time from surface of nanoparticles, which also reduces the stability of the obtained colloidal molecules.

Several other strategies, such as phage display, leucine zipper interaction and DNA-DNA hybridization, have also been used to assemble filamentous viruses in to superstructures [1]–[4]. But they always show low efficiency. Therefore, in this chapter we explore a simpler method to create robust virus based colloidal molecules, utilizing affinity between disulfides of the viruses and noble metallic nanoparticles. In this case, we avoid all the complicate steps including reduction, biotinylation and streptavidin-biotin interaction. It is well known that sulfurs, including thiols, disulfides and thiolates, can react to the surface of noble metals, like gold, platinum, silver and palladium [5]–[12]. The formed bond is described as weak covalent bond [13], [14] that is stronger than any non-specific bond including streptavidin-biotin interaction. Prior studies have shown that the organic or biologic sulfur can self-assemble on the surface of these metals [10], [15], [16], which could be used in applications like biological sensor and drug delivery. Specifically, by chemically functionalizing each virus coat protein with thiols, AuNBs have been grafted to the body and tip of the filamentous viruses [17]. Yet the sulfur—metal bond has not yet been directly employed to create virus based colloidal molecules.

In this chapter, the M13 viruses (including M13KE and M13C7C), possessing exposed disulfide groups (Cys-Cys) only at the end of p3 protein (proximal end), can be used as ideal building blocks with strongly reactive or “patchy” ends. Based on the reaction between disulfides and noble metallic nanoparticles, we aim to produce AB_n type virus based colloidal molecules, where A represents the metallic nanoparticle, and B represents M13 virus, with n the

valency (i.e., number of reacted viruses per nanoparticle) (Figure 1a). In this chapter, we only focus on investigating the reaction efficiency between metallic nanoparticles and M13 viruses (details about tuning valency of the colloidal molecules will be discussed in Chapter 4). Specifically, several aspects for this reaction between viruses and metallic nanoparticles will be studied in this chapter, including strains of viruses, metal species, capping reagents, ionic strength, and initial molar excess, to prove the generic feature of this methodology. Besides, electrostatic interaction will be investigated as a mean of conjugation between the distal end of viruses and metallic nanoparticles (Figure 1b), by tuning the ionic strength.

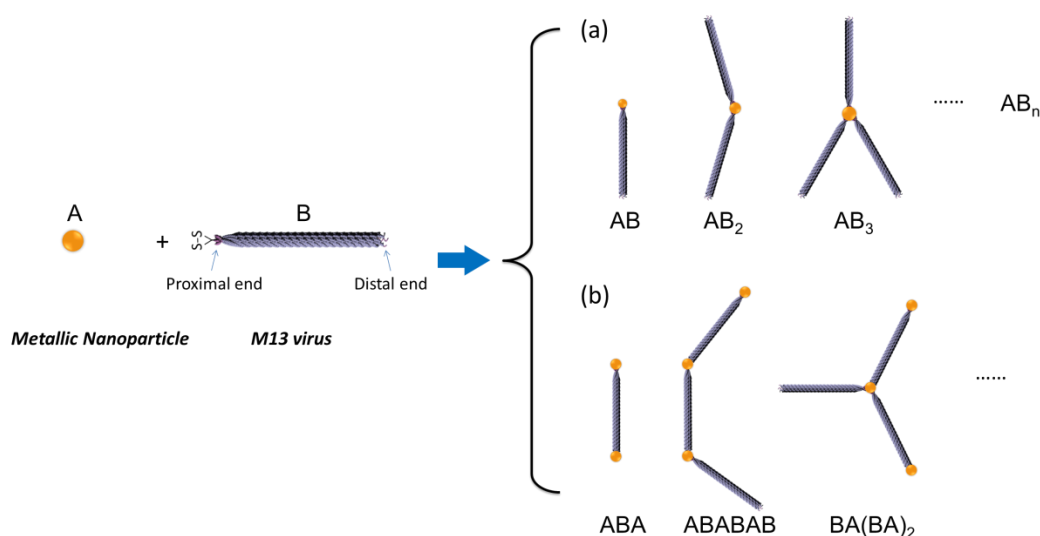


Figure 1: Illustration of reaction between metallic nanoparticles and M13C7C viruses. (a) Colloidal molecules of AB_n type are obtained when the metallic nanoparticles are reacted to the proximal ends via sulfur–metal bond. (b) When the metallic nanoparticles are also bound to the distal end due to electrostatic interaction, ABA type and colloidal chains (trains) or branches can be formed. A and B represent metallic nanoparticle and M13 virus, respectively.

3.2 Materials and Methods

(a) M13 viruses

In this chapter, two different strains of M13 viruses are used including the M13KE with a wide type p3 protein and M13C7C which has been genetically fused with disulfides constrained (Cys-Cys) peptide to the N-terminal of p3 proteins (Figure 2). The fused peptides of M13C7C on p3 protein are identified by DNA sequencing as follows: ACDPVREATCGGG, where the

two cysteines form a disulfide bridge. For M13KE, the most available sulfur (cysteine) is located at 7th position of p3 protein: AETVESCLAKPH, which could potentially be used for binding with metallic nanoparticles if sufficiently exposed. (Complete sequence of amino acids of p3 protein for M13C7C and M13KE is provided in Appendix I.)

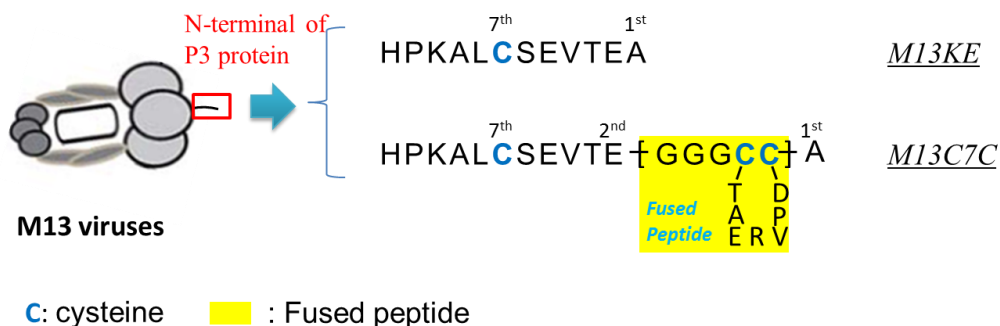


Figure 2: Illustration of the position of sulfur (cysteine) in p3 protein of M13KE and M13C7C strains. Compared to M13KE, p3 protein of M13C7C processes a fused peptide containing two cysteines forming a disulfide bridge. This fused peptide is inserted between 1st and 2nd amino acid, and highlighted in yellow. The next cysteine that can be exposed is located at 7th position.

M13 viruses, including M13KE and M13C7C viruses were produced and purified by standard biological method [18], then suspended in Tris·HCl (I = 110 mM, pH 8.2) buffer at a concentration of 2 mg/mL (corresponding to particle concentration of 6.5×10^{13} /mL) as stock solution stored at 4 °C. Concentration of the viruses was determined by the optical density at 269 nm with an extinction coefficient $\epsilon_{269} = 3.84 \text{ mg}^{-1} \text{ mLcm}^{-1}$.

(b) Au nanobeads

Au nanobeads (AuNBs) of diameter 17.3 and 18.7 nm are stabilized in suspension with two different capping reagents—tannic acid and citrate, respectively. Sizes of the AuNBs were measured by transmission electron microscope (TEM) (Hitachi H600) operating at 75 kV. Diameter distributions are shown in Figure 3. TEM images were recorded with an AMT CCD camera. Tannic acid capped AuNB (17.3 nm) suspension was purchased from Nanocomposix; Citrate capped AuNB suspension were gift from Serge Ravaine.

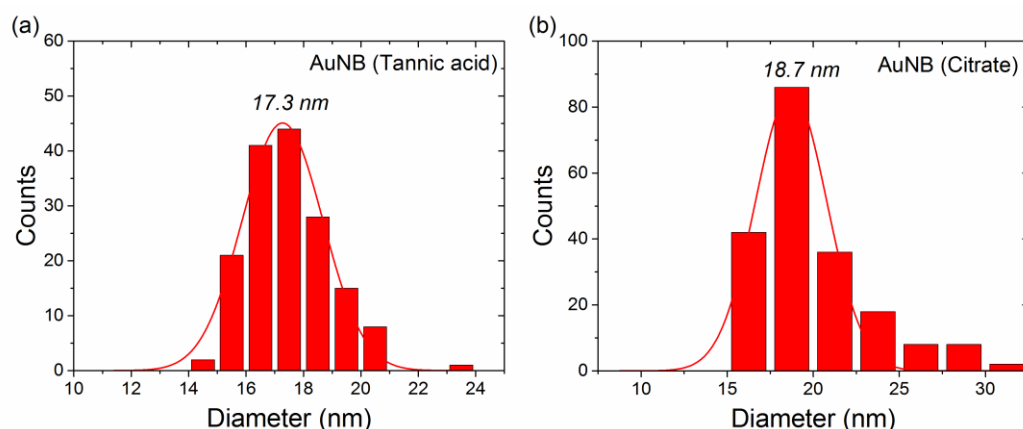


Figure 3: Diameter distributions of the tannic acid and citrate capped Au nanobeads (AuNBs) measured by TEM. Average diameters are obtained by Gaussian fits which are showed as red lines.

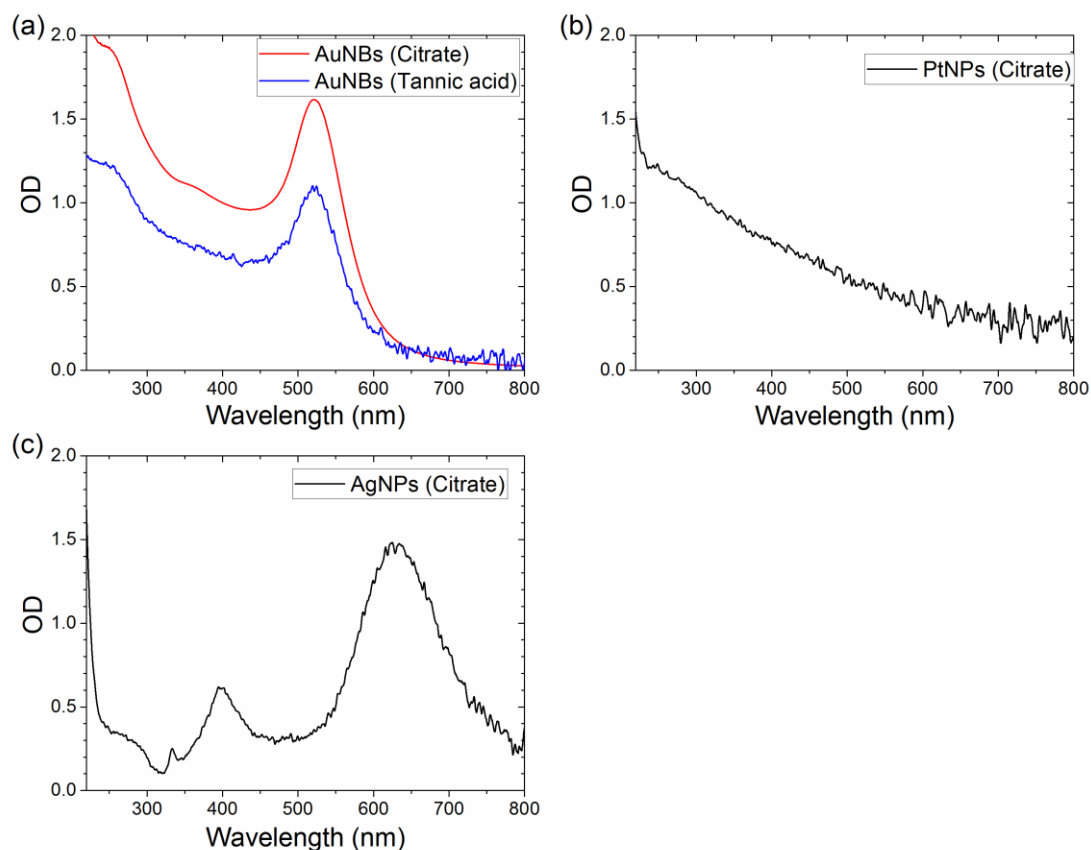


Figure 4: UV-Vis spectra for stock suspensions of metallic nanoparticles used in this chapter.

Concentrations of the AuNB suspensions are calculated based on the UV-Vis absorptions (measured by Nanodrop one, Thermo, UV-Vis spectra are shown in Figure 4a) due to the surface plasmon resonance effect. Two main methods based respectively on absorption at 400

and 520 nm have been reported to measure the concentration of Au nanobeads. The absorption at 400 nm can be used to deduce the Au(0) concentrations using the molar extinction coefficient $\epsilon_{400} = 2400 \text{ M}^{-1}\text{cm}^{-1}$ [19]. Particle density is then calculated knowing the size of AuNB. The absorption at 520 nm gives the Au particle concentration with a molar extinction coefficient ϵ_{520} depending on the diameter of AuNB. In this chapter, specific ϵ_{520} is taken from the fitting based on the data from Cytodiagnosics [20], as presented in Figure 5.

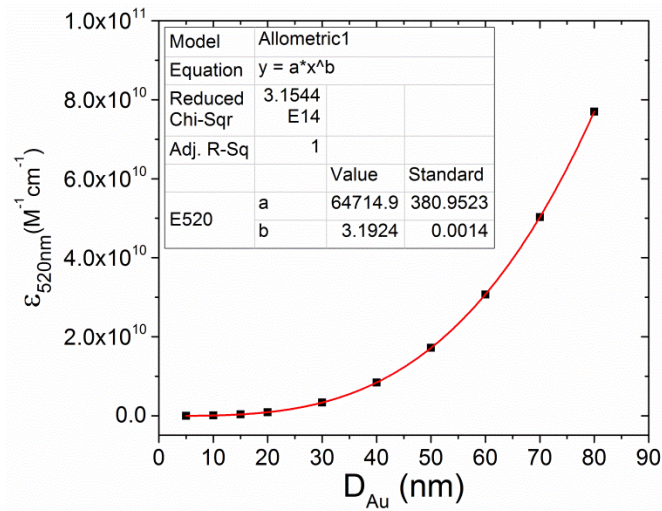


Figure 5: Molar extinction coefficient taken from Cytodiagnosics. Fitting is done with an allometric function. According to the fitting, the ϵ_{520} for 17.3 nm AuNBs is $5.80 \times 10^8 \text{ M}^{-1}\text{cm}^{-1}$.

Here we present the calculation for concentration of 17.3 nm AuNBs as an example:

(i) Based on the optical density (OD) at 400 nm: Diameter of AuNB is $D = 17.3 \text{ nm}$ as determined by TEM (Figure 3a), volume of one nanobead is $V = \pi D^3/6 = 2854 \text{ nm}^3$, and its corresponding mass is $m = \rho V = 5.51 \times 10^{-17} \text{ g}$, where $\rho = 19.3 \text{ g/cm}^3$ is the density of Au. Optical density of the 17.3 nm Au nanobead suspension at 400 nm is $\text{OD}_{400} = 0.679 \text{ cm}^{-1}$ (Figure 4a), so Au(0) concentration is $C_{\text{Au}(0)} = \text{OD}_{400}/\epsilon_{400} = 2.83 \times 10^{-4} \text{ mol/L}$. Then particle concentration of this AuNB suspension is calculated as $C_{\text{AuNB}} = C_{\text{Au}(0)} \cdot M_w/m = 1.01 \times 10^{12} \text{ particles/mL}$, where $M_w = 197 \text{ g/mol}$ is the molar mass of gold.

(ii) Based on the OD at 520 nm: Molar extinction coefficient for 17.3 nm AuNBs are taken from the fitting in Figure 5, which is $\epsilon_{520} = 5.80 \times 10^8 \text{ M}^{-1}\text{cm}^{-1}$. Optical density at 520 nm is $\text{OD}_{520} = 1.096 \text{ cm}^{-1}$ (Figure 4a). Particle concentration of the suspension in mole is determined by $C_{\text{AuNB}} = \text{OD}_{520}/\epsilon_{520} = 0.189 \times 10^{-8} \text{ mol/L} = 1.13 \times 10^{12} \text{ particles/mL}$.

The values of Au particle concentration calculated from method (i) and (ii) are consistent within a small error bar. This discrepancy could come from the fact that size of the AuNBs is not perfectly uniform. AuNB diameter always shows as a distribution, as shown in Figure 3. In this and following chapters, Au particle concentration calculated from method (i) is used, here is 1.01×10^{12} particles/mL.

(c) Platinum and silver nanoparticles

Size and concentration of citrate capped platinum nanoparticles (PtNPs, 30 nm) are taken from the information provided by supplier (NanoComposix). Silver nanoparticles are gift from Serge Ravaine, and their concentration is estimated to be 3.0×10^{11} particles/mL according to TEM counting. AuNBs suspension has the suitable concentration that can be used for reaction directly, but PtNPs and AgNPs suspensions are too diluted. To increase concentrations of PtNPs and AgNPs, centrifugations were performed (detailed conditions see Appendix II). Concentration after centrifugation is recalculated according to the UV-Vis absorbation compared to the initial spectra. Ionic strength is decreased to $I = 2$ mM before centrifugation to avoid any aggregation of the nanoparticles. Tris(2-carboxyethyl)phosphine (TCEP) used to improve reaction between sulfur and platinum/silver nanoparticles was purchased from Pierce.

Table 1: Summary of metallic nanoparticles used in the reactions with M13 viruses

Metallic nanoparticles	Diameter (nm)	Capping reagent
AuNBs	18.7	Citrate
	17.3	Tannic acid
PtNPs	30	Citrate
AgNPs	30~60*	Citrate

* AgNPs are mixture of triangle (prism) and spheres, size of the nanoparticles is estimated to be between 30 to 60 nm by TEM.

Details of the metallic nanoparticles are summarized in Table 1. For each reaction, the viruses and nanoparticles were dialyzed against the corresponding buffer and then stirred at 300 rpm in 1 mL glass vial at room temperature for 14 hours. Afterwards, samples were dialyzed against Tris·HCl $I = 2$ mM for storing before characterization by TEM. Note that all the metallic nanoparticles are capped either by tannic acid or by citrate. Both compounds can be replaced by organic sulfides, providing the possibility for reaction between M13 viruses and the metallic

nanoparticles. All the reactions in this chapter are performed at a concentration $C_v \leq C^* = 0.04$ mg/mL (overlapping concentration of M13 viruses).

3.3 Results and Discussions

3.3.1 Influence of M13 virus strains on the reaction with AuNBs

(a) M13KE

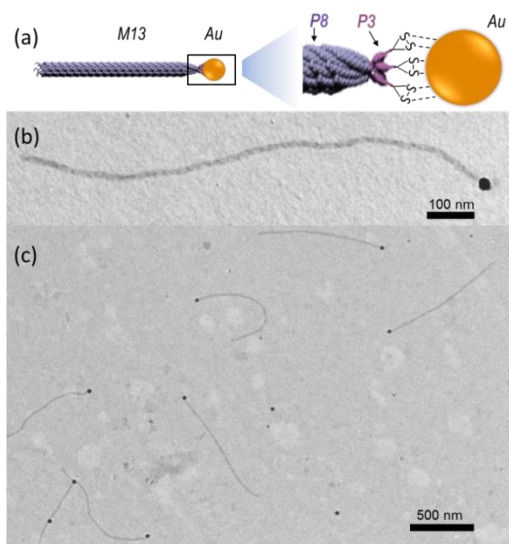


Figure 6: Sceptor-like AB type colloidal molecule formed by binding an AuNB to the proximal end of M13KE virus. A and B represent AuNB and M13 virus, respectively. (a) Schematic representation of AB type colloidal molecule. P3 proteins are located at proximal end of the M13KE virus, with exposed disulfides at their N-terminus. These disulfides can form weak covalent bond with AuNBs, resulting in very stable sceptor-like AB type colloidal molecules. (b) Transmission electron microscopy (TEM) image of one AB type sceptor-like colloidal molecule composed of one M13KE virus and an AuNB of diameter 17.3 nm. (c) Large field of view image showing seven AB type structures.

To start with, the conjugation of metallic nanoparticles to tips of filamentous viruses is investigated by using 17.3 nm tannic acid capped AuNBs and M13KE viruses. M13KE viruses have wide-type p3 proteins which have the first accessible sulfur (cysteine) at 7th position (Figure 2). The binding was performed under conditions of ionic strength $I = 10$ mM, pH 8.2, virus concentration $C_v = 0.04$ mg/mL, initial molar excess $\alpha = [\text{AuNB}]_0/[\text{M13}]_0 = 3$. Reaction yield was characterized by the fractions of viruses involved in each structure, $f(\text{M13}) = N_v/N_{tot}$, where N_v is number of viruses involved in structures and N_{tot} is total virus number. In

this chapter, all the reactions were performed with molar initial excess $\alpha \geq 1$. Thus, to determine the yields, we only count structures with viruses after reactions.

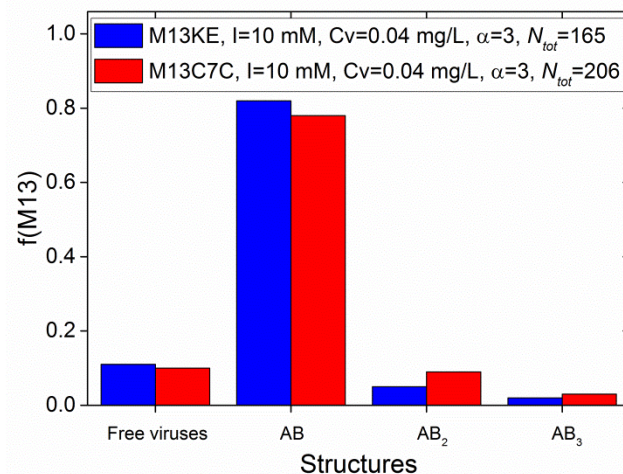


Figure 7: Fractions of colloidal molecules obtained by reaction between M13 viruses (including M13KE and M13C7C) and tannic acid capped AuNBs with initial molar excess $\alpha = 3$. At this high molar excess, both M13KE and M13C7C react well with AuNBs (about 90% viruses reacted), resulting in a majority of AB type colloidal molecules as products. The fraction of each structure is calculated by $f(M13) = N_v/N_{tot}$, where N_v is number of viruses involved in this structure and N_{tot} is total virus number.

After reaction, 90% M13KE viruses are bound to AuNBs, including a majority of 82% scepter-like AB type hybrid colloidal molecules (Figure 6) and small percentages of AB₂ type (5%) and AB₃ type (2%) colloidal molecules. We therefore demonstrate a very efficient conjugation between M13KE viruses and AuNBs. The high overall reaction yield is attributed to the weak covalent bond formed between sulfur (cysteine) and Au [7], [8], which is more efficient than any other non-specific bond, like the Biotin-Streptavidin interaction used in Chapter 2. Moreover, the high percentage of AB types (82%) among all the formed structures indicates a high selectivity of the morphology.

(b) M13C7C

In order to explore the generic feature of this reaction, another strain of viruses, M13C7C, is also reacted with tannic acid capped AuNBs for comparison with M13KE. Considering that this reaction is actually a sulfur—gold reaction, so the main difference between M13KE and M13C7C is position and number of sulfur (cysteine). M13C7C virus is fused with a disulfide

constrained (Cys-Cys) peptide between 1st and 2nd position of N-terminal of p3 protein, which means its sulfurs are supposed to be more exposed than M13KE. The reaction between AuNBs and M13C7C viruses were performed in the same conditions as M13KE, fractions of the products are summarized in Figure 7 (red columns). It actually shows a similar overall reaction yield as M13KE, including 78% AB type, 9% AB₂ type and 3% AB₃ type colloidal molecules.

Both strains of viruses, M13C7C and M13KE, react well with tannic acid capped AuNBs, with an overall yield of about 90%. It shows the feasibility of binding AuNBs to the proximal end of M13 viruses via sulfur—Au bond. Besides, reacting with M13KE also confirms that the reaction between AuNB and proximal end is not related to any specific peptides. (M13 viruses have been used a lot for phage display through the inserted peptide, but the approach shown here is more generic.)

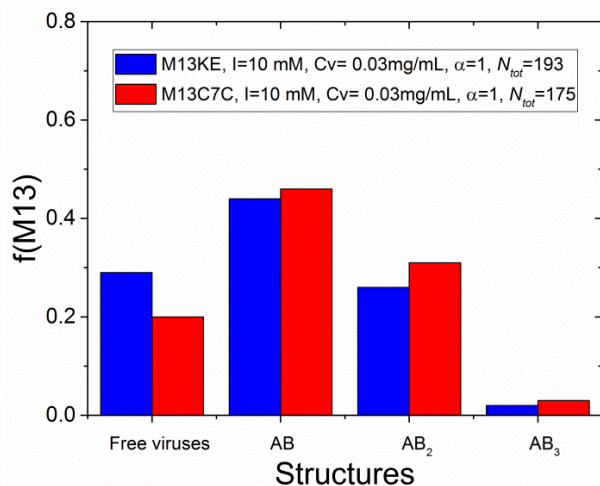


Figure 8: Fractions of structures obtained by reaction between M13 viruses (including M13KE and M13C7C) and tannic acid capped AuNBs with an initial molar excess $\alpha = 1$. M13C7C strain shows slightly higher overall yield than M13KE, which also indicates it has better affinity in the binding of AuNBs to its proximal tip. The fraction of each structure is calculated by $f(M13) = N_v/N_{tot}$, where N_v is number of viruses involved in this structure and N_{tot} is total virus number.

Considering these two strains have different number and position of exposed disulfides, they should have different efficiencies in tip-conjugation with tannic acid capped AuNBs. However, same yields between M13KE and M13C7C are observed. We believe this stems from the big excess of AuNBs ($\alpha = 3$) which diminishes their diversity. In order to determine the difference of reaction efficiency between these two strains, we performed the conjugations with

a smaller initial molar excess, $\alpha = 1$, and the results are shown in Figure 8. The distributions of obtained structures for both strains are still similar, except that more free viruses are left for M13KE than M13C7C, which means that the overall reaction yield for M13C7C (80%) is slightly higher than M13KE (71%). Therefore, we conclude that the M13C7C strain has slightly higher affinity than M13KE in the binding of AuNB to its proximal tip.

3.3.2 Improvement of the binding between M13 viruses and AuNBs by TCEP

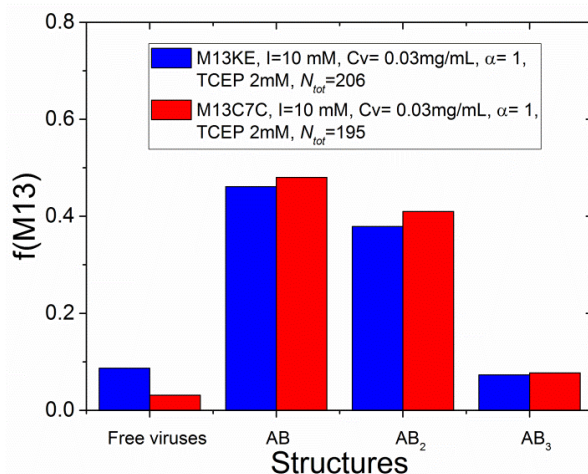


Figure 9: Overall yield of reactions between M13KE/M13C7C and AuNBs is improved by adding 2 mM TCEP. Compared to the results without TCEP (Figure 8), the overall yield is increased from 71% to 91% for M13KE and from 80 to 97% for M13C7C. The fraction of each structure is calculated by $f(M13) = N_v/N_{tot}$, where N_v is number of viruses involved in this structure and N_{tot} is total virus number.

In order to improve the conjugation between AuNBs and proximal end of the viruses, which essentially corresponding to the binding between sulfur and Au, TCEP is often used. Because TCEP can break the disulfide bridges which makes sulfurs more exposed to AuNBs. To check this effect, 2 mM TCEP is added to the two existing samples, M13KE and M13C7C viruses reacting with tannic acid capped AuNB with initial molar excess $\alpha = 1$, as described in the previous paragraph. Amount of TCEP is chosen according to results obtained by Derda's group [21]. Initially, 20% M13KE and 29% M13C7C are left unreacted in these two samples, respectively. Results after adding TCEP are presented in Figure 9. An efficient improvement is observed for both samples. Overall yield increases from 71% to 91% for M13KE and from 80% to 97% for M13C7C. In both cases, TCEP succeeds to break disulfide bridges, the formed thiols

are therefore more accessible by AuNBs, resulting in enhancement of binding efficiency. Note that the M13C7C still shows higher reaction efficiency than M13KE, which is consistent with the results without TCEP.

Since we have been observing a better binding between AuNBs and M13C7C than M13KE, with or without TCEP, in the following sections of this chapter, we choose to use M13C7C viruses for the conjugation with metallic nanoparticles.

3.3.3 Influence of metal species on the nanoparticle-M13C7C reaction

Inspired by the adsorption of organosulfides or alkanethiols on gold, reactions between sulfur and other metals, such as silver, copper, platinum, and palladium, have been derived [10], [12], [22], [23]. The high affinity of sulfur to noble metals makes it possible to introduce highly alterable functionalities. We have already proven that AuNBs can react well at the proximal tip of M13 viruses where exposed disulfides are located. In this section, we extend this bioconjugation by using two other noble metallic nanoparticles: silver and platinum.

(a) Platinum Nanoparticles

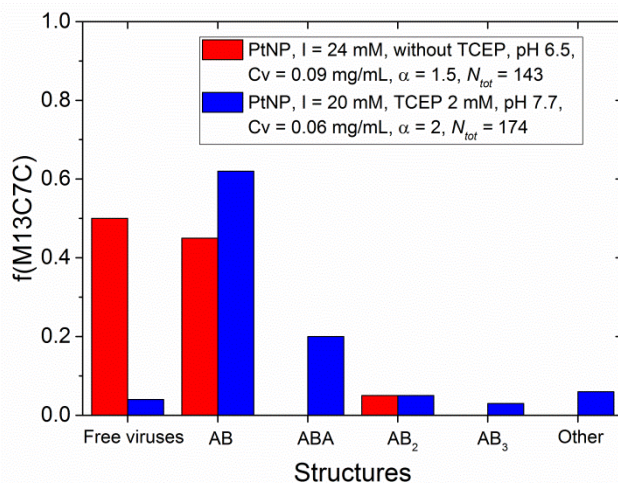


Figure 10: Fractions of colloidal structures obtained from reaction between M13C7C viruses and citrate capped platinum nanoparticles, with and without TCEP. The fraction of each structure is calculated by $f(\text{M13C7C}) = N_v/N_{tot}$, where N_v is number of M13C7C viruses involved in this structure and N_{tot} is total virus number. By increasing initial molar excess and adding TCEP, the overall yield is improved efficiently from 50% to more than 90%. Also the binding of PtNPs on the distal end of viruses occurs, yielding ABA type, and “other” big branched and linear colloidal molecules, as shown in Figure 11.

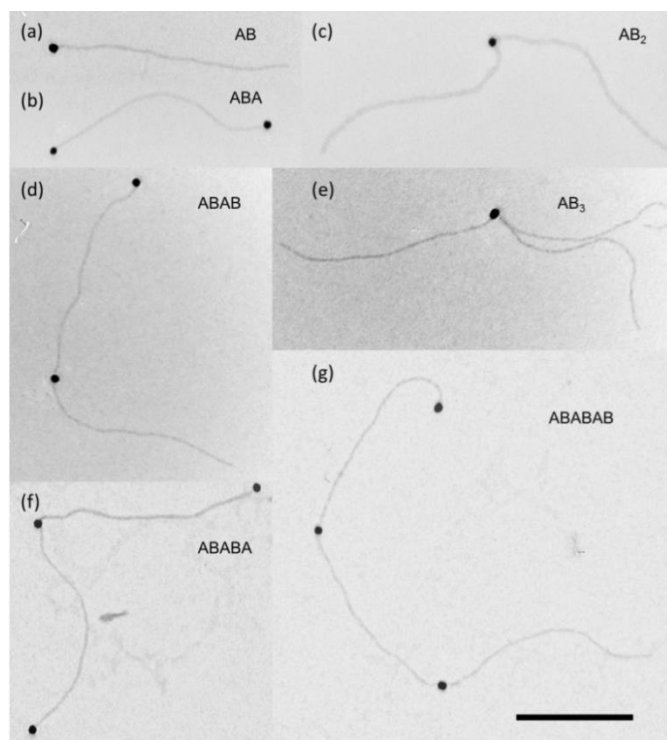


Figure 11: Transmission electron microscopy (TEM) images of the morphologies formed by PtNPs and M13C7C viruses. (a) AB type; (b) ABA type; (c) AB₂ type; (d) ABAB type; (e) AB₃ type; (f) ABABA type; (g) ABABAB type. A represents PtNP, B represents M13 virus. Scale bar, 500 nm.

Platinum is reported to have also good affinity to the thiols/disulfides [10], [24]–[26], but the reaction between citrate capped Platinum nanoparticles (PtNPs) and M13C7C viruses is not as efficient as for AuNBs. Results (Figure 10, red columns) show that only around half M13C7C viruses are reacted with a fraction of 42% AB type structures. Two factors could account for the reason of the lower yield compared to AuNBs: the affinity between Pt and disulfide is not as strong as Au [25]; the applied molar excess $\alpha = 1.5$ is less than what we used for AuNBs. We then improve the reaction by increasing the molar ratio to $\alpha = 2$ and adding TCEP to break the disulfide groups which makes the sulfur more exposed. Results (Figure 10, blue columns) show that TCEP can promote efficiently the reaction between PtNPs and M13C7C viruses. The fractions of total reacted M13C7C viruses increases to more than 90% in presence of TCEP. However, the yield for AB type is not very high (~60%), because in the products there exist also 20% ABA type, 5% AB₂ type, 3% AB₃ type, and a small fraction of other big branched and linear colloidal molecules (Figure 11). The formation of ABA types

means the PtNPs also bind to the distal end of the viruses. This effect, expected to be related to the capping reagent of NPs and electrostatic interaction, will be discussed in the Section 3.3.4.

A promising perspective for platinum hybridized colloidal molecules is that they could be used as self-propelled system using hydrogen peroxide as fuel [27]–[29]. However, most of the research works focus only on 2D motion of active particles because the size of the existing active systems is always big so that Brownian motion is negligible. In the case of our AB type colloidal molecules (with a platinum particle at the end), their sizes are small enough that can be considered for exploring the 3D motion in an active system.

(b) Silver Nanoparticles

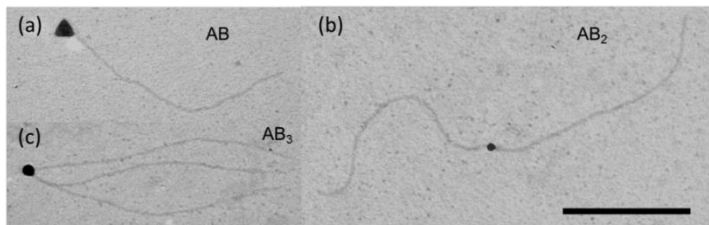


Figure 12: TEM images of colloidal molecules composed of M13C7C viruses and silver nanoparticles. (a), (b), and (c) are AB type, AB₂ type and AB₃ type respectively. Scale bar, 500 nm.

Silver is another noble metal frequently used in the colloidal and nano science and it has been reported to have even better affinity to sulfur than gold [11]. Here, AgNPs are also employed to confirm the generic feature of reaction between sulfur on the proximal end of viruses and metallic nanoparticles. A preliminary reaction between M13C7C and citrate capped AgNPs without TCEP didn't succeed. Therefore, we improved the reaction efficiency by adding 2 mM TCEP. Meantime, the initial molar excess and ionic strength are also increased to $\alpha = 5$ and $I = 45$ mM, which could also favor the binding. Finally, we succeeded in the binding of AgNPs at the proximal end of M13C7C viruses (Figure 12). Totally, 67% of viruses have reacted, yielding 54% AB type, 11% AB₂ type, and 2% AB₃ type colloidal molecules, as shown in Figure 13. The low overall reaction efficiency could be partially due to one of the biggest disadvantages of silver, i.e., its oxidation [26]. The formed oxidized coat on the AgNP surface can hinder the reaction then results in a low yield. Besides, the concentration of M13C7C used in this reaction is one order of magnitude lower (compared to AuNBs and PtNPs), which also can be the reason of low yield. Because silver nanoparticles are quite unstable (oxidized easily),

it is therefore not suitable system for further investigation. After verifying that AgNPs is able to react with proximal end of M13C7C viruses, we didn't perform more experiments to optimize the conditions and improve the efficiency of this reaction.

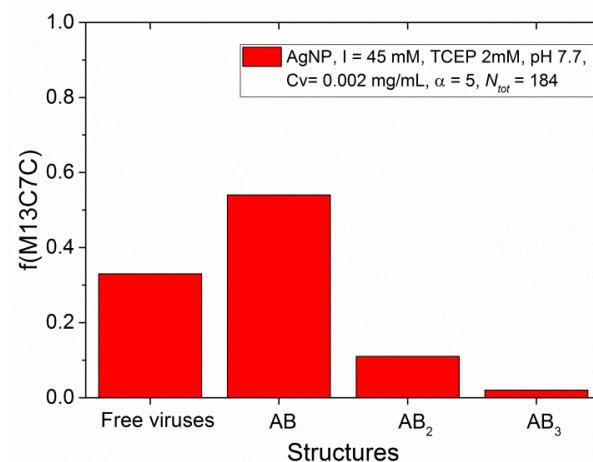


Figure 13: Reaction of M13C7C with citrate capped silver nanoparticles. In the presence of TCEP, about 65% of M13C7C have reacted with AgNPs, yielding mainly AB type (54%), AB₂ type (11%) and very few AB₃ type structures. The fraction of each morphology is calculated by $f(M13C7C) = N_v/N_{tot}$, where N_v is number of M13C7C viruses involved in this structure and N_{tot} is total virus number.

Overall, the platinum and silver nanoparticles are all proven to be able to react with proximal ends of M13C7C viruses via the metal—sulfur bond. Therefore, we demonstrate that the reaction between AuNBs and the proximal end of M13 viruses can be extended to other noble metals, which can serve as a generic method to create hybrid colloidal molecules and superstructures with filamentous viruses.

3.3.4 Roles of capping reagent and ionic strength on the binding between M13C7C and AuNBs

The capping reagents of metallic nanoparticles will be discussed in this section are tannic acid and citrate (Figure 14). These two ligands provide different colloidal stabilities for the metallic nanoparticles. Both compounds can be exchanged and replaced by sulfur containing biomolecules, which provides the possibility for reaction between disulfides at proximal end of viruses and metallic nanoparticles. In this section, we investigate the influence of capping reagent by binding citrate and tannic acid capped AuNBs to tips of M13C7C viruses at different ionic strengths.

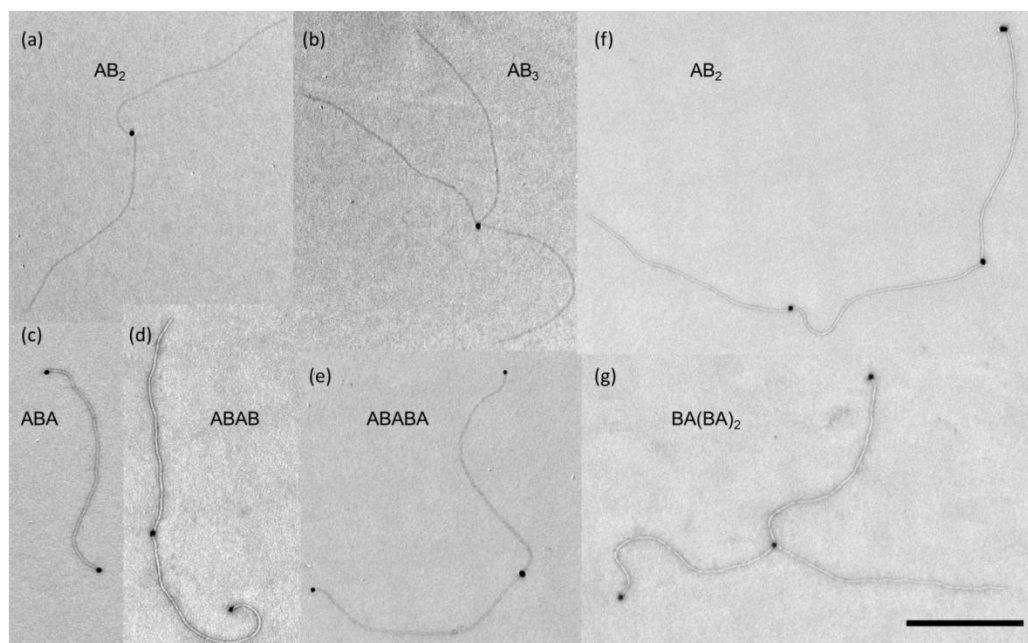


Figure 16: TEM images of different colloidal molecules assembled by M13C7C viruses and citrate capped AuNBs. (a, b) The AB_n type colloidal molecules are formed at low ionic strength, where binding of AuNBs only occurred at virus proximal end. When the binding occurs also on the distal end of M13C7C viruses by electrostatic interaction, ABA type (c), ABAB type (d), ABABA type (e), chain-/train-like ABABAB type (f) and branched $BA(BA)_2$ type are also formed. Scale bar, 500 nm.

At very low ionic strength ($I = 1$ mM), almost no reaction occurred at the end of M13C7C viruses (blue columns in Figure 15) due to the long ranged electrostatic repulsion, as both viruses and AuNBs are negatively charged. The range of the repulsion is defined by the Debye screening length, given by:

$$\kappa^{-1} = \frac{1}{\sqrt{8\pi l_B N_A I}}, \quad (1)$$

where l_B is the Bjerrum length (of about 0.71 nm in water at room temperature), N_A is Avogadro's number and I is ionic strength. At $I = 1$ mM, $\kappa^{-1} = 9.6$ nm, AuNBs and viruses cannot approach each other. Once the ionic strength is increased to 5 mM, range of the repulsion is partially screened (κ^{-1} decreases to 4.3 nm), thus efficiency of the reaction between citrate capped AuNBs and proximal ends strongly increases (red columns in Figure 15). More than 80% viruses have reacted with citrate capped AuNBs, including 76% AB type colloidal molecules. Except for the AB type, small percentages of AB_2 and AB_3 types (Figure 16a, b) are

also observed in the products. The reaction on the proximal end can still be improved by increasing ionic strength to 10 mM (green columns in Figure 15) where the Debye length decreases to $\kappa^{-1} = 3.0$ nm. In this case, a high yield of 91% AB type colloidal is obtained. With this high yield, it's possible to massively produce Scepter-like hybrid colloidal particles. After a suitable centrifugation to remove the excess of free AuNBs (calculations for determining the conditions of the centrifugation are discussed in Appendix II), these monodisperse colloidal nanoparticles could be used for various purposes, such as self-organization. Beyond this ionic strength, at $I = 15$ mM ($\kappa^{-1} = 2.5$ nm), part of the citrate capped AuNBs lose their colloidal stability and aggregate, resulting in 23% viruses involved in aggregates (magenta columns in Figure 15). Meanwhile, the citrate capped AuNBs start to bind to the distal end of M13C7C viruses, which is the same behavior as the one already observed with the citrate stabilized PtNPs (Figure 11). As a result, various colloidal molecules are observed, including a fraction of 32% of ABA type and a small percentage of other big structures, as shown in Figure 16c–g. The possible reason of AuNBs reaction with the distal end of the viruses is electrostatic attraction between p9 proteins and the capping reagent of AuNBs (citrate). Even though the viruses are highly negatively charged mainly given by p8 proteins, the distal end shows locally slightly positive charge because of p9 proteins (p7 proteins are also located at the distal end of M13C7C viruses, but they are buried and screened from the environment [31]; Detailed information of charge properties of p9 protein is presented in Appendix I). The minor positive charges are “hidden” by strongly negative charges at low ionic strength (0–10 mM), consequently showing overall repulsion between viruses and AuNBs. At high ionic strength, the positive charges are able to be exposed slightly and attract the negatively charged AuNBs (citrate capped), which could result in a reaction between distal ends of viruses and AuNBs. This reaction could be employed to create hybrid colloidal oligomers as long as we can keep the citrate capped AuNBs stable at high ionic strength, which is practically difficult. Overall, in order to avoid aggregation of citrate capped AuNBs, the optimal ionic strength for reaction between viruses and these nanobeads is ionic strength $I = 10$ mM.

(b) Tannic acid capped AuNBs

We have shown that with citrate capped AuNBs, the binding on proximal end of M13C7C viruses was achieved with high efficiency. However, the citrate capped AuNBs were not stable

at high ionic strength. They partially aggregated in buffer of $I = 15$ mM. This brings problems for other research that requires the usage of high ionic strength, like reaction of fluorescently labeled viruses with AuNBs and production of AB_n ($n \geq 2$) type colloidal molecules (see Chapter 4 and 5). Therefore, in this chapter, better stabilized AuNBs, which are capped by tannic acid, are used to react to the proximal end of viruses. Experimentally, tannic acid capped AuNBs were mixed with M13C7C viruses at five various ionic strengths $I = 2, 10, 20, 40,$ and 80 mM. Virus concentrations, initial molar excess and pH of buffer are fixed at $C_v = 0.04$ mg/mL, $\alpha = 3$ and pH 8.2, respectively. A similar influence of ionic strength is found as for citrate capped AuNBs. At low ionic strength ($I = 2$ mM) (Figure 17, blue column), reaction efficiency is low due to the electrostatic repulsion between both negatively charged viruses and tannic acid (pK_a of tannic acid is between 7 and 8, depending on its extent of dissociation [32]). At too high ionic strength, the tannic acid capped AuNBs aggregate, as we found that the AuNB suspension turns dark quickly in $I = 80$ mM buffer. In between ($I = 10, 20,$ and 40 mM), M13C7C viruses react well with the tannic acid capped AuNBs. For all these three samples, more than 90% viruses have reacted at the proximal end to AuNBs. Moreover, among all the obtained structures, 75% to 80% AB types are yielded, indicating a high selectivity of products in these experimental conditions. The tannic acid capped AuNBs show much better colloidal stability than citrate capped ones, as they are still stable at $I = 40$ mM. This is very important for the further dynamic study, because the fluorescently labeled viruses require an ionic strength of about 40 mM to react with AuNBs (discussed in Chapter 5). Between $I = 10$ and 40 mM, no obvious effect of ionic strength is observed for tannic acid capped AuNBs. Compared with citrate capped AuNBs (at $I = 10$ mM), we obtained slightly less AB type with tannic acid capped AuNBs but more AB_2 and AB_3 types. This could attribute to the higher concentration (0.04 mg/mL for tannic acid capped AuNBs, 0.01 mg/mL for citrate capped ones), that increases the possibility of two or three viruses bond to one AuNB.

We also tried to bind tannic acid capped AuNBs to distal ends of M13 viruses. But we didn't succeed, and no ABA type is observed. We believe it stems from the lack of electrostatic attraction. As mentioned in the Section 3.3.3(a), citrate capped AuNBs are negatively charged, which can bind to the slightly positively charged p9 protein on the distal end of viruses. However, tannic acid is much less charged because its pK_a (between 7 and 8, depending on its

extent of dissociation [32]) is much smaller than pK_{a1} of citric acid ($pK_{a1} = 3.0$, $pK_{a2} = 4.6$, $pK_{a3} = 5.8$ [30]). Another possible reason is that the tannic acid is a better capping reagent and more difficult to be replaced than citrate. Electrostatic interaction is not as strong as disulfide—Au bond therefore cannot provide the affinity between tannic acid capped AuNBs and the distal end of viruses.

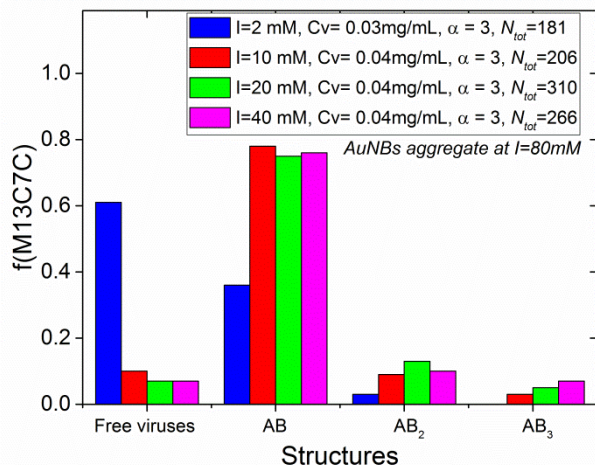


Figure 17: Influence of ionic strength on the reaction between Tannic acid capped AuNBs and M13C7C viruses. Five ionic strengths are used, $I = 2$ (blue), 10 (red), 20 , (in green), 40 mM (blue) and 80 mM (AuNBs aggregate). The other experimental parameters are initial molar excess $\alpha = [AuNB]_0/[M13C7C]_0 = 3$, $pH = 8.2$, virus concentration $C_v = 0.04$ mg/mL (0.3 mg/mL for $I = 2$ mM). The overall yield increases with ionic strength, once the ionic strength is high enough (between 10 and 40 mM), it doesn't influence significantly the reaction. The fraction of each structure is calculated by $f(M13C7C) = N_v/N_{tot}$, where N_v is number of viruses involved in this structure and N_{tot} is total virus number.

By comparing citrate capped AuNBs with tannic acid capped AuNBs, we can conclude that: First, no significant influence is found between these two capping compounds in terms of binding on the proximal ends of viruses which essentially is Au—disulfide interaction. Second, the tannic acid acts as a better stabilizer than citrate, which is preferable when we need to perform experiments at a high ionic strength or to conserve the sample for a long-term use. Last, the citrate capped AuNBs can partially bind also to the distal end of the viruses, which could be utilized for synthesis of hybrid colloidal oligomers.

3.3.5 Influence of initial molar excess on the reaction between M13C7C and AuNBs

The effect of initial molar excess $\alpha = [\text{AuNB}]_0/[\text{M13C7C}]_0$ on reaction between AuNBs and proximal ends of M13C7C is studied, using AuNBs capped with tannic acid. Three molar excesses, $\alpha = 1, 3,$ and $5,$ are applied, with ionic strength and pH are fixed at 10 mM and 8.2, respectively. Results are presented in Figure 18. With $\alpha = 1,$ the reaction is not very efficient, and still 20% of viruses remain free. And the selectivity of the products is low, including 46% AB type and 31% AB₂ type colloidal molecules. Increasing the initial molar excess α from 1 to 3 dramatically enhances the reaction efficiency and the yield for AB type. About 90% M13C7C have reacted, including a yield of AB type of 78%. With a higher molar excess of 5, the reaction is still slightly improved: 94% viruses are reacted and yield of AB type increases to 85%. Overall, the reaction is improved significantly when the initial molar excess is increased from 1 to 3, and slightly from 3 to 5, in terms of both efficiency and selectivity of AB type colloidal molecules. From practical point of view, molar excess $\alpha = 3$ is more preferable if the aim is mass production of AB type hybrid colloidal molecules. In this case, we can still obtain high yield but reduce the cost a lot compared to using $\alpha = 5.$

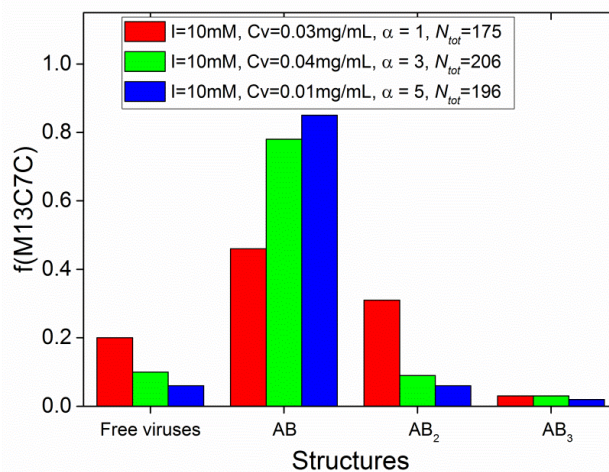


Figure 18: Influence of initial molar excess $\alpha = [\text{AuNB}]_0/[\text{M13C7C}]_0$ on the reaction between M13C7C viruses and tannic acid capped AuNBs. Three molar excesses: $\alpha = 1$ (red), 3 (green), and 5 (blue) are used. From $\alpha = 1$ to 3, the efficiency of the reaction and yield of AB type are efficiently increased. From $\alpha = 3$ to 5, the efficiency and selectivity of AB₂ type still increase but only slightly. The fraction of each structure is calculated by $f(\text{M13C7C}) = N_v/N_{tot}$, where N_v is number of viruses involved in this structure and N_{tot} is total virus number.

3.4 Conclusions

In this chapter, we present a simple, robust and reliable methodology that can be used to create rod based hybrid colloidal molecules. The rod-like M13 viruses (including M13KE and M13C7C), exhibiting exposed disulfide groups at their proximal tips, can bind metallic nanoparticles (including Au, Pt and Ag nanoparticles) to their tips. The reaction between proximal end of the filamentous viruses and metallic nanoparticles are reliable regardless of metal species, strains of filamentous viruses and capping reagents of nanoparticles (as long as they can be exchanged). Besides, AuNBs do show better reaction efficiency than PtNPs and AgNPs. The adding of TCEP can improve the binding between viruses and metallic nanoparticles, especially for Pt and Ag. In order to form Scepter-like AB type, tannic acid capped AuNBs are suggested, because they are colloidal stable in buffer at high ionic strength (up to 40 mM). With an initial molar excess $\alpha \geq 3$, high yield of AB type can be produced (~80%), which then can be used for the study of their self-organization. The binding of metallic nanoparticles can also occur at the distal end of M13 when citrate is used as capping reagent. However, this reaction is not yet controllable. Therefore, in the next chapter we focus on the binding of proximal end of viruses to AuNBs to synthesize colloidal molecules with tunable valency.

3.5 References

- [1] G. T. Hess, C. P. Guimaraes, E. Spooner, H. L. Ploegh, and A. M. Belcher. Orthogonal labeling of M13 minor capsid proteins with DNA to self-assemble end-to-end multiphage structures. *ACS Synth. Biol.*, 2013, 2: 490–496.
- [2] R. Y. Sweeney, E. Y. Park, B. L. Iverson, and G. Georgiou. Assembly of Multimeric Phage Nanostructures Through Leucine Zipper Interactions. *Biotechnol. Bioeng.*, 2006, 95: 539–545.
- [3] Y. Huang *et al.* Programmable Assembly of Nanoarchitectures Using Genetically Engineered Viruses. *Nano Lett.*, 2005, 5: 1429–34.
- [4] K. T. Nam, B. R. Reelle, S. W. Lee, and A. M. Belcher. Genetically Driven Assembly of Nanorings Based on the M13 Virus. *Nano Lett.*, 2004, 4: 23–27.
- [5] R. Di Felice and A. Selloni. Adsorption modes of cysteine on Au(111): Thiolate, amino-thiolate, disulfide. *J. Chem. Phys.*, 2004, 120: 4906–4914.
- [6] R. G. Nuzzo and D. L. Allara. Adsorption of Bifunctional Organic Disulfides on Gold Surfaces. *J. Am. Chem. Soc.*, 1983, 105: 4481–4483.
- [7] J. L. Burt, C. Gutiérrez-Wing, M. Miki-Yoshida, and M. José-Yacamán. Noble-metal nanoparticles directly conjugated to globular proteins. *Langmuir*, 2004, 20: 11778–11783.

- [8] H. Grönbeck, A. Curioni, and W. Andreoni. Thiols and disulfides on the Au(111) surface: The headgroup-gold interaction. *J. Am. Chem. Soc.*, 2000, 122: 3839–3842.
- [9] Z. Huang, F. Chen, P. A. Bennett, and N. Tao. Single Molecule Junctions Formed via Au–Thiol Contact: Stability and Breakdown Mechanism. *J. Am. Chem. Soc.*, 2007, 129: 13225–13231.
- [10] Z. Li, S. C. Chang, and R. S. Williams. Self-assembly of alkanethiol molecules onto platinum and platinum oxide surfaces. *Langmuir*, 2003, 19: 6744–6749.
- [11] Y. J. Lee, I. C. Jeon, W. Paik, and K. Kim. Self-Assembly of 1,2-Benzenedithiol on Gold and Silver: Fourier Transform Infrared Spectroscopy and Quartz Crystal Microbalance Study. *Langmuir*, 1996, 12: 5830–5837.
- [12] J. C. Love, D. B. Wolfe, M. L. Chabinyc, K. E. Paul, and G. M. Whitesides. Self-assembled monolayers of alkanethiolates on palladium are good etch resists. *J. Am. Chem. Soc.*, 2002, 124: 1576–1577.
- [13] P. Kohli, K. K. Taylor, J. J. Harris, and G. J. Blanchard. Assembly of covalently-coupled disulfide multilayers on gold. *J. Am. Chem. Soc.*, 1998, 120: 11962–11968.
- [14] Y. Xue, X. Li, H. Li, and W. Zhang. Quantifying thiol-gold interactions towards the efficient strength control. *Nat. Commun.*, 2014, 5: 4348.
- [15] T. Sainsbury, T. Ikuno, D. Okawa, D. Pacilé, J. M. J. Fréchet, and A. Zettl. Self-assembly of gold nanoparticles at the surface of amine- and thiol-functionalized boron nitride nanotubes. *J. Phys. Chem. C*, 2007, 111: 12992–12999.
- [16] A. Ulman *et al.* Self-assembled monolayers of rigid thiols. *J. Biotechnol.*, 2000, 74: 175–188.
- [17] D. Montalvan-Sorrosa, J. L. González-Solis, J. Mas-Oliva, and R. Castillo. Filamentous virus decoration with gold nanoparticles: global fingerprints of bionanocomposites acquired with SERS. *RSC Adv.*, 2014, 4: 57329–57336.
- [18] J. Sambrook and W. D. Russell. *Molecular Cloning A Laboratory Manual*, 4th Ed. Cold Spring Harbor Laboratory Press: New-York, 2012.
- [19] T. Hendel, M. Wuithschick, F. Kettemann, A. Birnbaum, K. Rademann, and J. Polte. In Situ Determination of Colloidal Gold Concentrations with UV–Vis Spectroscopy: Limitations and Perspectives. *Anal. Chem.*, 2014, 86: 11115–11124.
- [20] www.cytodiagnosics.com/store/pc/Gold-Nanoparticle-Properties-d2.htm.
- [21] S. Kalhor-Monfared *et al.* Rapid Biocompatible Macrocyclization of Peptides with Decafluorosulfone. *Chem. Sci.*, 2016, 9: 1–6.
- [22] B. Xu, G. Gonella, B. G. Delacy, and H. L. Dai. Adsorption of anionic thiols on silver nanoparticles. *J. Phys. Chem. C*, 2015, 119: 5454–5461.
- [23] P. E. Laibinis, G. M. Whitesides, D. L. Allara, Y. T. Tao, A. N. Parikh, and R. G. Nuzzo. Comparison of the structures and wetting properties of self-assembled monolayers of n-alkanethiols on the coinage metal surfaces, copper, silver, and gold. *J. Am. Chem. Soc.*, 1991, 113: 7152–7167.
- [24] D. A. Stern *et al.* Adsorbed Thiophenol and Related Compounds Studied at Pt(111) Electrodes by EELS, Auger Spectroscopy, and Cyclic Voltammetry. *J. Am. Chem. Soc.*, 1988, 110: 4885–4893.
- [25] J. A. Williams and C. B. Gorman. Alkanethiol reductive desorption from self-assembled monolayers on gold, platinum, and palladium substrates. *J. Phys. Chem. C*, 2007, 111: 12804–12810.

- [26] J. C. Love, L. A. Estroff, J. K. Kriebel, R. G. Nuzzo, and G. M. Whitesides. Self-assembled monolayers of thiolates on metals as a form of nanotechnology. *Chem. Rev.*, 2005, 105: 1103–1169.
- [27] W. Wang, W. Duan, S. Ahmed, A. Sen, and T. E. Mallouk. From one to many: Dynamic assembly and collective behavior of self-propelled colloidal motors. *Acc. Chem. Res.*, 2015, 48: 1938–1946.
- [28] S. Sanchez, L. Soler, and J. Katuri. Chemically powered micro- and nanomotors. *Angew. Chem. Int. Ed.*, 2015, 54: 1414–1444.
- [29] W. F. Paxton, P. T. Baker, T. R. Kline, Y. Wang, T. E. Mallouk, and A. Sen. Catalytically induced electrokinetics for motors and micropumps. *J. Am. Chem. Soc.*, 2006, 128: 14881–14888.
- [30] H. T. S. Britton and A. R. Robinson. CXCVIII.—Universal buffer solutions and the dissociation constant of veronal. *J. Chem. Soc.*, 1931, 1456–1462.
- [31] H. Endemann and P. Model. Location of filamentous phage minor coat proteins in phage and in infected cells. *J. Mol. Biol.*, 1995, 250: 496–506.
- [32] T. Ahmad. Reviewing the tannic acid mediated synthesis of metal nanoparticles. *J. Nanotechnol.*, 2014, 2014: 1–11.

Chapter 4

Self-assembly of rod-like viruses into colloidal molecules with controlled valency

Contents

4.1	Introduction	92
4.2	Materials and Methods.....	93
4.3	Results and Discussion.....	95
4.3.1	Influence of ionic strength on the valency of self-assembled colloidal molecules.....	95
4.3.2	Influence of AuNB surface area on the valency of self-assembled colloidal molecules	98
4.3.3	Quantitative Model for the valency of colloidal molecules	99
4.3.4	Mass production of AB ₂ type colloidal molecules.....	103
4.4	Conclusions	105
4.5	References	105

4.1 Introduction

We have shown that metallic nanoparticles can bind efficiently to the proximal end of M13 viruses thanks to the sulfur-metal covalent bond. On the contrary, binding on the distal end is much less efficient and not really controllable. Therefore, in this chapter we explore the assembly of virus based colloidal molecules with tunable valency (n , number of viruses reacted with one nanoparticle) using the binding of metallic nanoparticles only to proximal end of M13 viruses. Tannic acid capped Au nanobeads (AuNBs) and M13C7C viruses are chosen as building blocks in these investigations because: the tannic acid capped AuNBs show better colloidal stability, higher reaction efficiency than other metallic nanoparticles, and regio-selective binding only to virus proximal end (Chapter 3); M13C7C phage has a better affinity to AuNBs than M13KE.

In Chapter 3, the efficiency of the reaction between metallic nanoparticles and M13 viruses is explored with an initial molar excess $\alpha = [\text{AuNB}]_0/[\text{M13}]_0$ more than 1. As a result, the AB type ($n = 1$, A: metallic nanoparticle, B: M13 virus) colloidal molecules are always preferable. Here we investigate the aspects that influence valency at a low $\alpha < \frac{1}{n_{max}}$, where n_{max} is the maximum number of viruses that can bind to an AuNB of a given diameter. It means that we always apply a large initial excess of viruses compared to AuNBs, i.e., $1/\alpha = [\text{M13}]_0/[\text{AuNB}]_0 > n_{max}$. In this case, valency of the obtained colloidal molecules is found to be influenced by two key parameters, effective diameter of filamentous viruses and AuNB surface area. Experimentally, ionic strength defines the effective diameter of viral particles by changing the range of electrostatic interactions between viruses. On the other hand, diameter of AuNBs determines the binding surface available for the proximal tips of viruses. Thanks to mature skills to synthesize relatively monodisperse Au nanoparticles of defined sizes and shapes [1]–[4], valency of the colloidal molecules can be easily tuned solely by varying the diameter of AuNBs (Figure 1). A quantitative model is then proposed to describe the valency dependence on the diameter of AuNBs and ionic strength. Since the valency of obtained virus based colloidal molecules always shows a distribution, the yield of the produced structures of a fixed valency decreases with increasing the valency. Therefore, we choose to produce in large scale the simplest multivalent colloidal molecules, i.e., AB₂ types, to obtain highest yield.

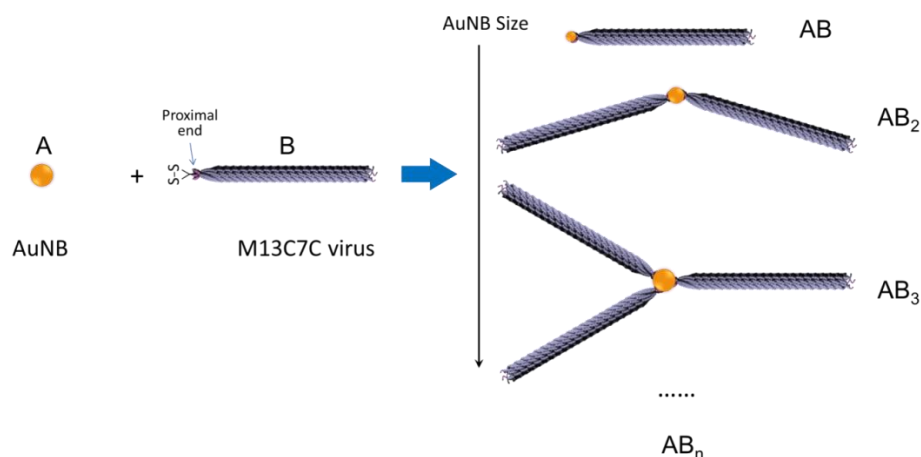


Figure 1: Schematic representation of the reaction between AuNB (Au nanobead) and M13C7C viruses. Colloidal molecules with various valencies, such as AB, AB₂, and AB₃ types, are obtained by varying the diameter of AuNBs in presence of a large excess of viruses.

4.2 Materials and Methods

The tannic acid stabilized AuNBs of diameter 4.3, 11.1, 17.3, and 52.0 nm were purchased from NanoComposix. Diameters of the AuNBs were characterized by transmission electron microscopy (TEM) (Figure 2), and their concentrations are determined based on the UV-Vis absorption (Figure 3, measured by Nanodrop one, Thermo) at 400 [5] and 520 nm, respectively (Example of the calculation of a particle concentration is shown in Chapter 3).

The reactions between AuNBs and proximal tips of the M13C7C viruses (disulfides) are separated into 4 batches, with each batch using the AuNBs of same diameter but four different ionic strengths, $I = 10, 40, 80$ (or 110), and 200 mM. To perform one set of reactions, the AuNB suspension was first dialyzed against $I = 10$ mM buffer, and then mixed with corresponding amount of viruses according to the initial molar excess $1/\alpha = [\text{M13C7C}]_0/[\text{AuNB}]_0$ presented in Table 1. These initial molar excesses are confirmed much larger than the corresponding obtained valencies: for all the AuNBs of different sizes, we have $1/\alpha > 4n$ (Table 1). The volume of virus suspension is very small comparing to AuNB suspension, so its influence on the ionic strength can be neglected. The reaction at this ionic strength ($I = 10$ mM) was conducted overnight (14 hours), with stirring at 300 rpm, room temperature. The ionic strength of the given sample was then increased stepwise to $I = 40, 80$ (or 110), 200 mM by dialysis, followed by reactions (stirring at 300 rpm, room temperature for 14 hours) at each ionic strength. In this way,

we also avoid the aggregation of AuNBs caused by directly increasing the ionic strength to high value (80 and 200 mM). Note that for 52.0 nm AuNBs, ionic strength $I = 110$ mM was applied instead of 80 mM. After each reaction, only structures containing AuNBs, including free AuNBs, were counted, ignoring therefore the big excess of free viruses in the statistics.

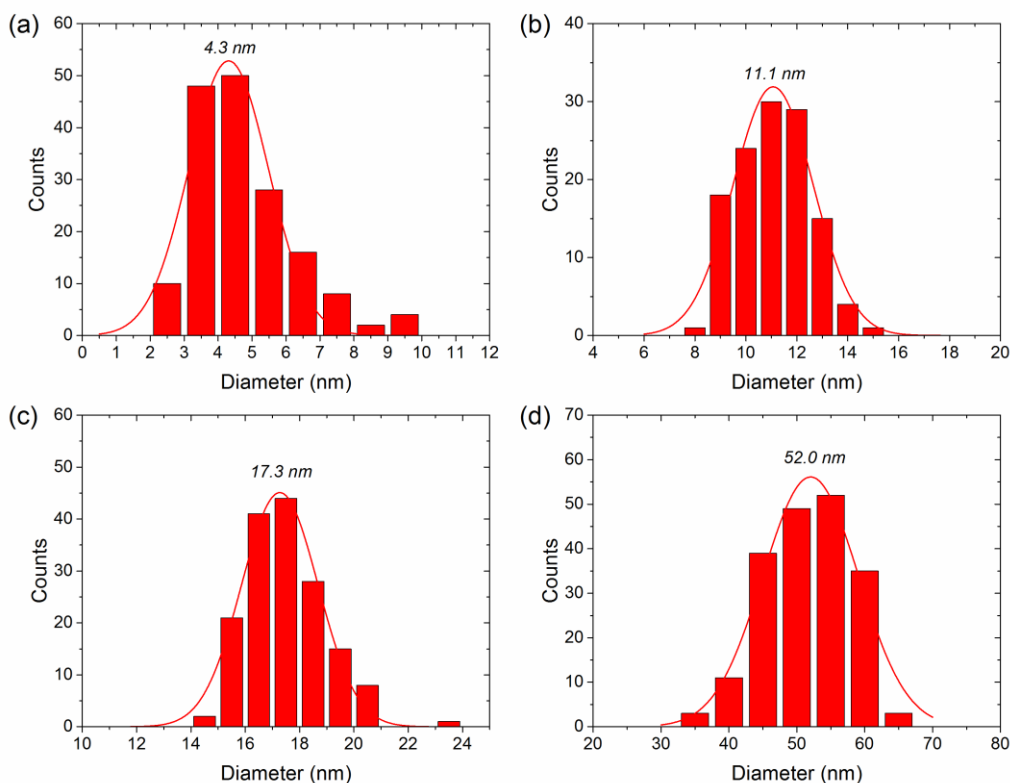


Figure 2: Diameter distributions of tannic acid capped AuNBs (measured by TEM) used in this chapter. Average diameters are obtained by Gaussians fits (red lines).

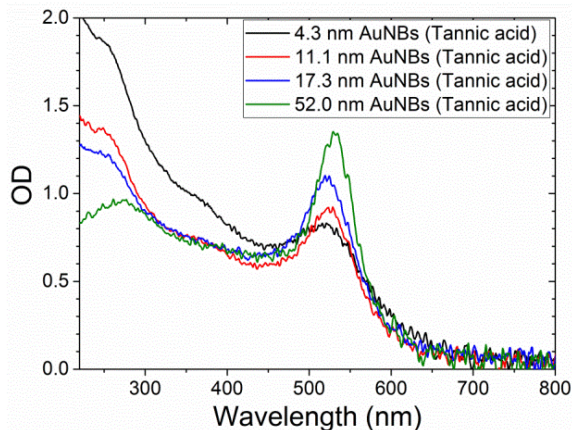


Figure 3: UV-Vis spectra for stock suspensions of AuNBs used in this chapter.

Table 1: Summary of the experimental conditions used for reactions between AuNBs and M13C7C viruses, and the corresponding average valencies after reaction.

Au diameter D_{Au} (nm)	Surface area ^a S (nm ²)	Initial molar excess ^b $1/\alpha$	Average valency at different ionic strengths				
			10 mM	40 mM	80 mM	110 mM	200 mM
4.3	58	5.4	1.02	1.28	1.31	--	1.25
11.1	387	23	1.18	1.51	1.72	--	1.72
17.3	940	78	1.32	1.82	2.18	--	2.66
52.0	8495	100	3.8	12.0	--	17.1	20.2

^aSurface area of AuNB $S = \pi D_{Au}^2$; ^bInitial molar excess $1/\alpha = [M13C7C]_0/[AuNB]_0$. These initial molar excesses are confirmed much large than the corresponding final valencies.

All the samples were characterized by TEM on a Hitachi H-600 microscope operating at 75 kV, and images were recorded with an AMT CCD camera. The diluted virus suspension (typically 10^{-3} mg/mL) was settled onto freshly O₂ plasma treated (Harrick Plasma, PDC-001) 200-mesh Formvar/carbon-coated grids (Agar), and stained with 2% (w/w) uranyl acetate.

4.3 Results and Discussion

4.3.1 Influence of ionic strength on the valency of self-assembled colloidal molecules

For a given size of AuNB, the valency of resulted colloidal molecules is related to the effective diameter of the virus that binds to the bead surface. Therefore, ionic strength is an important parameter to tune the valency of the obtained colloidal molecules, because it determines the effective diameter of the rod-like viruses through the range of their electrostatic repulsions. M13C7C viruses are mixed with AuNBs of various sizes (4.3, 11.1, 17.3 and 50 nm), and the reactions are performed at various ionic strengths $I = 10, 40, 80$ (or 110) and 200 mM. Because valency always shows as a distribution, as presented in Figure 4, the average valency, $\langle n \rangle$, calculated by the arithmetic mean from the distribution, is used to characterize the variation of the valency of the resulting colloidal molecules.

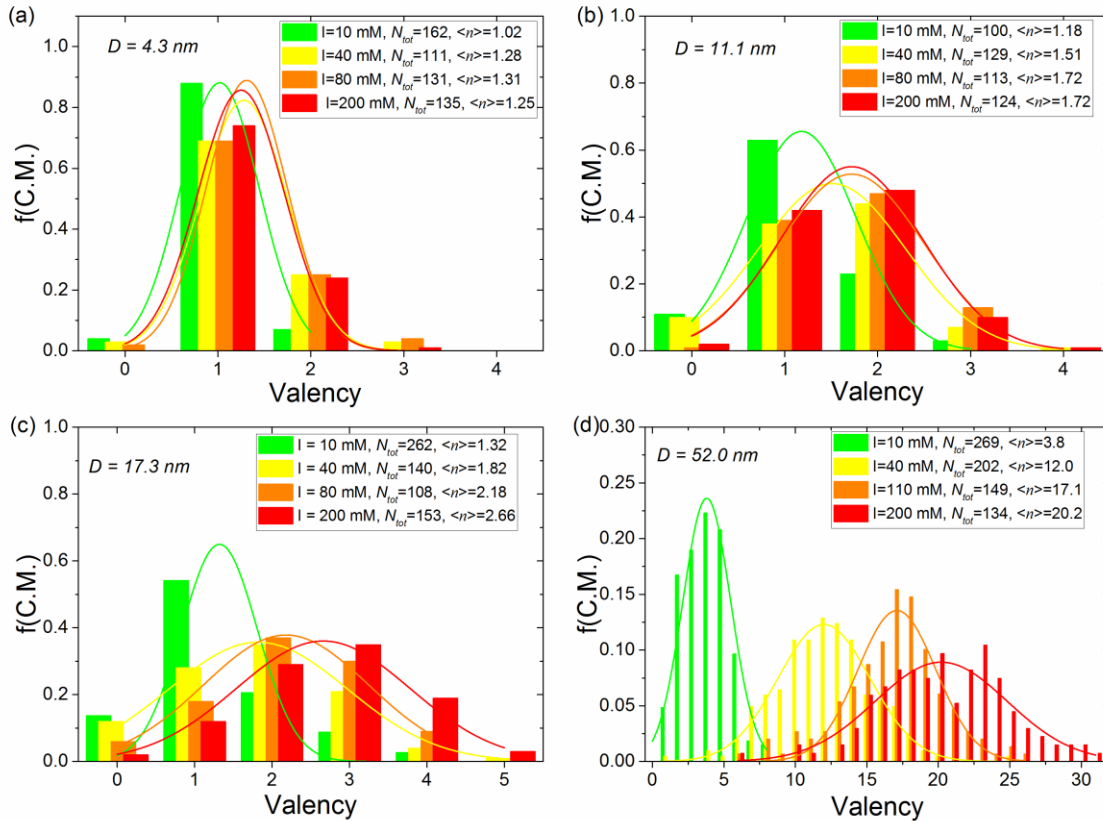


Figure 4: Valency distributions the colloidal molecules at various ionic strengths for AuNBs of diameter (a) 4.3, (b) 11.1, (c) 17.3 and (d) 50 nm. The fraction of colloidal molecules with a given valency is defined by $f(\text{C.M.}) = \frac{N}{N_{\text{tot}}}$, where N is the number of this colloidal molecules and N_{tot} is total number of counted colloidal molecules including the free AuNBs (i.e. valency 0). Average valencies, $\langle n \rangle$, are calculated by the arithmetic mean from the distributions. The width of each distribution is determined by a Gaussian fit.

For the AuNBs of small size (4.3 nm), the ionic strength has weak influence on the resulting valency of colloidal molecules. As shown in the Figure 4a, the average valency is 1.0 at low ionic strength ($I = 10$ mM) and increases slightly to around 1.3 at high ionic strength. Since this AuNB has a diameter even smaller than M13C7C viruses (7 nm), geometrically only one virus is able to bind to it. The experimental results actually show slightly higher valency (around 1.3) at high ionic strength range (40 to 200 mM), which could be attributed to the not perfectly uniform size of AuNBs (diameter distribution is shown in Figure 2a). The small percentage of larger AuNBs can react with two M13C7C viruses which therefore increases the average valency.

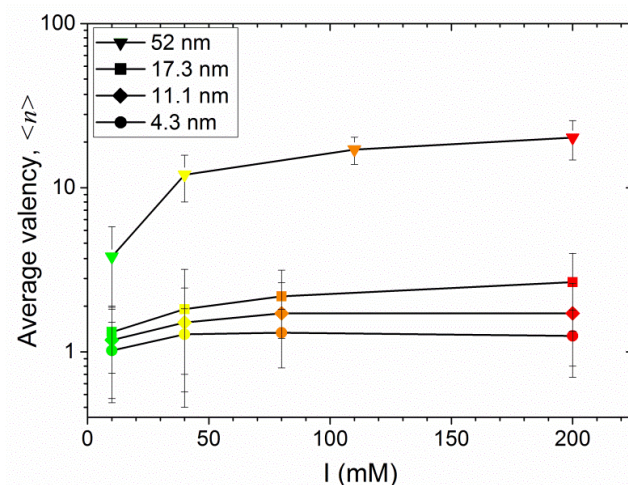


Figure 5: Average valencies of colloidal molecules formed by reacting AuNBs of diameter 4.3, 11.1, 17.3 and 50 nm with excess of viruses at various ionic strengths. The average valency, $\langle n \rangle$, increases with ionic strength and reaches a plateau when ionic strength is higher than 80 mM. The error bars are the standard deviations obtained from Gaussian fits of distributions shown in Figure 4.

For the AuNBs of 11.1, 17.3, and 50 nm, their surface areas are big enough to react with more than one virus. An increase of valency with ionic strength is observed, as shown in the Figure 4(b-d) and Figure 5. For a given size of AuNBs, the average valency $\langle n \rangle$ increases rapidly in the low ionic strength range and reaches a plateau at high ionic strength. As described, the M13C7C viruses are highly negatively charged (average linear charge density $7 e^-/\text{nm}$), and the AuNBs are also slightly negatively charged due to the tannic acid capping reagent at the experimental pH 8.2 (pK_a of tannic acid is between 7 and 8, depending on the extent of its dissociation [6]). That means a weak electrostatic repulsion between AuNBs and viruses but a strong repulsion between viruses themselves. So electrostatics is not a strong barrier to impede binding one M13C7C virus to AuNB. As a result, high overall reaction efficiency between M13C7C and AuNB is achieved (there are always more than 85% AuNBs reacted with viruses, as shown in Figure 4, i.e., very small amount of free AuNBs.).

However, in order to form AB_n ($n \geq 2$) type colloidal molecules, M13C7C viruses have to approach each other. As we mentioned, the electrostatic repulsion between viruses themselves is strong due to their high charge density. The range of this repulsion is related to the Debye screening length which is given by $\kappa^{-1} = \frac{1}{\sqrt{8\pi l_B N_A I}}$, where l_B is the Bjerrum length (of about 0.71 nm in water at room temperature), and N_A is Avogadro's number. The ionic strength, I ,

determines the effective diameter of the viruses which depends on the range of repulsion. By increasing the ionic strength, the Debye screening length reduces, resulting in a decrease of the effective diameter of the viruses, thus more viruses are allowed to bind to one AuNB. Consequently, colloidal molecules with higher valency than 1, like AB_2 , AB_3 types, are formed. The valency of the obtained colloidal molecules always displays a distribution, and its width broadens with increasing the valency. When high ionic strength ($I = 200$ mM) is used, the Debye screening length decreases to $\kappa^{-1} = 0.68$ nm which is much less than AuNB diameter, i.e. $\kappa^{-1} \ll D_{Au}$. In this case, only steric effects dominate the valency of obtained colloidal molecules.

4.3.2 Influence of AuNB surface area on the valency of self-assembled colloidal molecules

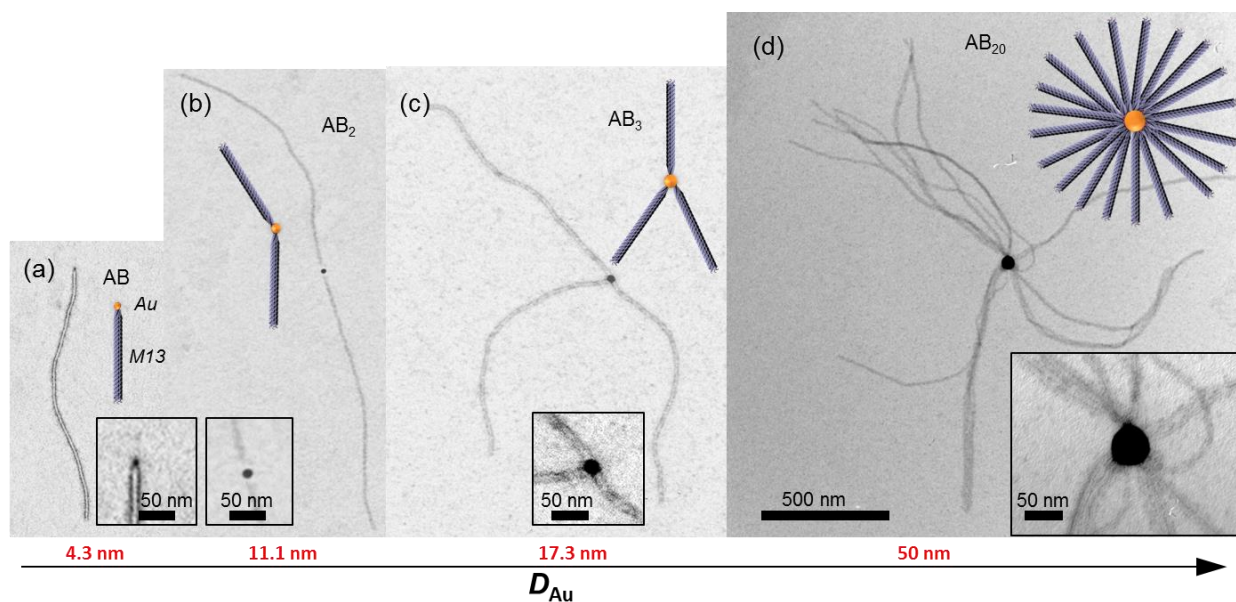


Figure 6: TEM images and corresponding schemes of the colloidal molecules with valency tuned by varying the diameter of AuNBs at ionic strength of $I = 200$ mM. Mean values of the valencies, $\langle n \rangle$, are found to be 1.3, 1.7, 2.7, and 20.2 for AuNBs of diameter 4.3, 11.1, 17.3, and 50 nm, respectively.

Due to the steric effects, a distinct dependence of valency on the surface area of AuNBs at a fixed ionic strength is revealed, as illustrated in Figure 6. With diameter of 4.3 nm, most AuNBs react with only one virus, forming AB type colloidal molecules, because surface area of this AuNB is not big enough for a second virus to bind regardless of the ionic strength. When the diameter of AuNBs increases to 11.1 or 17.3 nm, still mainly AB type colloidal molecules (> 50%) are formed at low ionic strength ($I = 10$ mM, $\kappa^{-1} = 3.0$ nm), because of the high

electrostatic repulsion between two viruses. But when a higher ionic strength is used ($I \geq 40$ mM, $\kappa^{-1} \leq 1.52$ nm), the range of repulsion decreases so that two or three M13C7C viruses are able to react with one AuNB. Therefore, at $I = 200$ mM ($\kappa^{-1} = 0.68$ nm), AB₂ type colloidal molecules are mainly produced using 11.1 nm AuNBs (Figure 6b, yield of 48%), and the average valency of about 3 is obtained with 17.3 nm AuNBs. With 50 nm AuNBs, a similar trend is found, except that a high valency is already obtained at low ionic strength ($I = 10$ mM). Because the size of these AuNBs ($D_{Au} = 50$ nm) is much bigger than the Debye length ($D_{Au} \gg \kappa^{-1}$) even at $I = 10$ mM, several viruses are able to bind to one AuNB. As a result, average valency of 3.8 is found for 50 nm AuNB at ionic strength $I = 10$ mM, as shown in Figure 4d. With increasing the ionic strength, a final valency of about 20 is obtained at $I = 200$ mM. The valency distribution also broadens with increasing the AuNB size, meaning yield of the main product decreases.

4.3.3 Quantitative Model for the valency of colloidal molecules

We have shown that the average valency of the virus based colloidal molecules increases with both the size of AuNBs and the ionic strength. In this section, a simple model is proposed to quantitatively describe the relation between them.

In this model, we consider the M13C7C virus as an elongated cylinder that can bind to the surface of spherical AuNBs by their proximal ends (due to the Au—sulfur bond). In the ionic aqueous solution, the charged viruses and AuNBs are both considered to have electrostatically effective sizes that are functions of the ionic strength. Therefore, the number of viruses bonded to one AuNB, i.e., valency n , is a function of the effective surface area of AuNBs and the effective tip area of M13 viruses:

$$n = f(S_{Au}^{eff}(I), S_{M13}^{eff}(I)), \quad (1)$$

where $S_{Au}^{eff}(I)$ and $S_{M13}^{eff}(I)$ are effective areas of AuNB surface and M13 proximal tip.

Since the AuNBs are weakly charged compared to viruses, the effective surface area of an AuNB can be approximated as its geometrically bare surface area, which means $S_{Au}^{eff}(I) \approx S_{Au}$. Then, the valency of resulting colloidal molecules, is proportional to the surface area of AuNBs at a given ionic strength:

$$n \propto S_{Au} \quad (2)$$

The effective area of the virus tip, $S_{M13}^{eff}(I)$, can be described as the area it occupies on the surface of AuNB (the total available binding area is S_{Au}). As there is always at least one virus bound to AuNB (valency $n \geq 1$) even when the size of AuNBs tends to be infinitely small, the valency of the obtained colloidal molecules is presumed to be written as

$$n = 1 + \frac{S_{Au}}{S_{M13}^{eff}(I)}. \quad (3)$$

Equation (3) is tested by plotting and linearly fitting the experimental average valency $\langle n \rangle$ as a function of surface area, S_{Au} , at different ionic strengths, as shown in Figure 7. Surprisingly, a good linear dependence of valency on the AuNB surface area is found. It confirms our approximation ($S_{Au}^{eff}(I) \approx S_{Au}$) and indicates the electrostatic effects on the size of AuNB can be neglected. The slope of the fits, $1/S_{M13}^{eff}$, increasing with the ionic strength, are derived correspondingly (Figure 7).

On the other hand, the ionic strength still has an influence on the electrostatically effective size of the highly charged viruses. For example, it has been reported that the phase diagram of filamentous viruses in suspension depends strongly on the ionic strength. Here the effective area of proximal tip of viruses, S_{M13}^{eff} , are also determined by the ionic strength. The radius of this effective area, R_{M13}^{eff} , can be considered as the effective range of repulsive interactions between the proximal ends, which is a function of the Debye screen length (κ^{-1}). Inspired by Onsager, who mentioned “the effective range of the electrostatic repulsion (between charged colloidal particles) will be a modest multiple of the screening distance κ^{-1} ” [7], we can describe this effective radius as

$$R_{M13}^{eff} = r_0 + A \cdot \kappa^{-1}, \quad (4)$$

where, $r_0 = 3.5$ nm, is the bare radius of M13C7C virus, $\kappa^{-1} = \frac{1}{\sqrt{8\pi l_B N_A I}}$ is Debye screening length associated with ionic strength, and A is a numerical factor.

Therefore, S_{M13}^{eff} can be written as:

$$S_{M13}^{eff} = \pi \cdot (R_{M13}^{eff})^2 = \pi \cdot (r_0 + A \cdot \kappa^{-1})^2. \quad (5)$$

Substitute κ^{-1} in Equation (5), we obtain

$$S_{M13}^{eff} = \pi \cdot \left(r_0 + A \cdot \frac{1}{\sqrt{8\pi l_B N_A I}} \right)^2. \quad (6)$$

Then substitute Equation (6) in Equation (3), we can deduce the expression for valency as

$$n = 1 + \frac{S_{Au}}{\pi \cdot \left(r_0 + A \cdot \frac{1}{\sqrt{8\pi l_B N_A I}} \right)^2}. \quad (7)$$

From Equation (7), we can see clearly that the AuNB surface area and ionic strength are two independent variables to tune the valency of the resulted colloidal molecules.

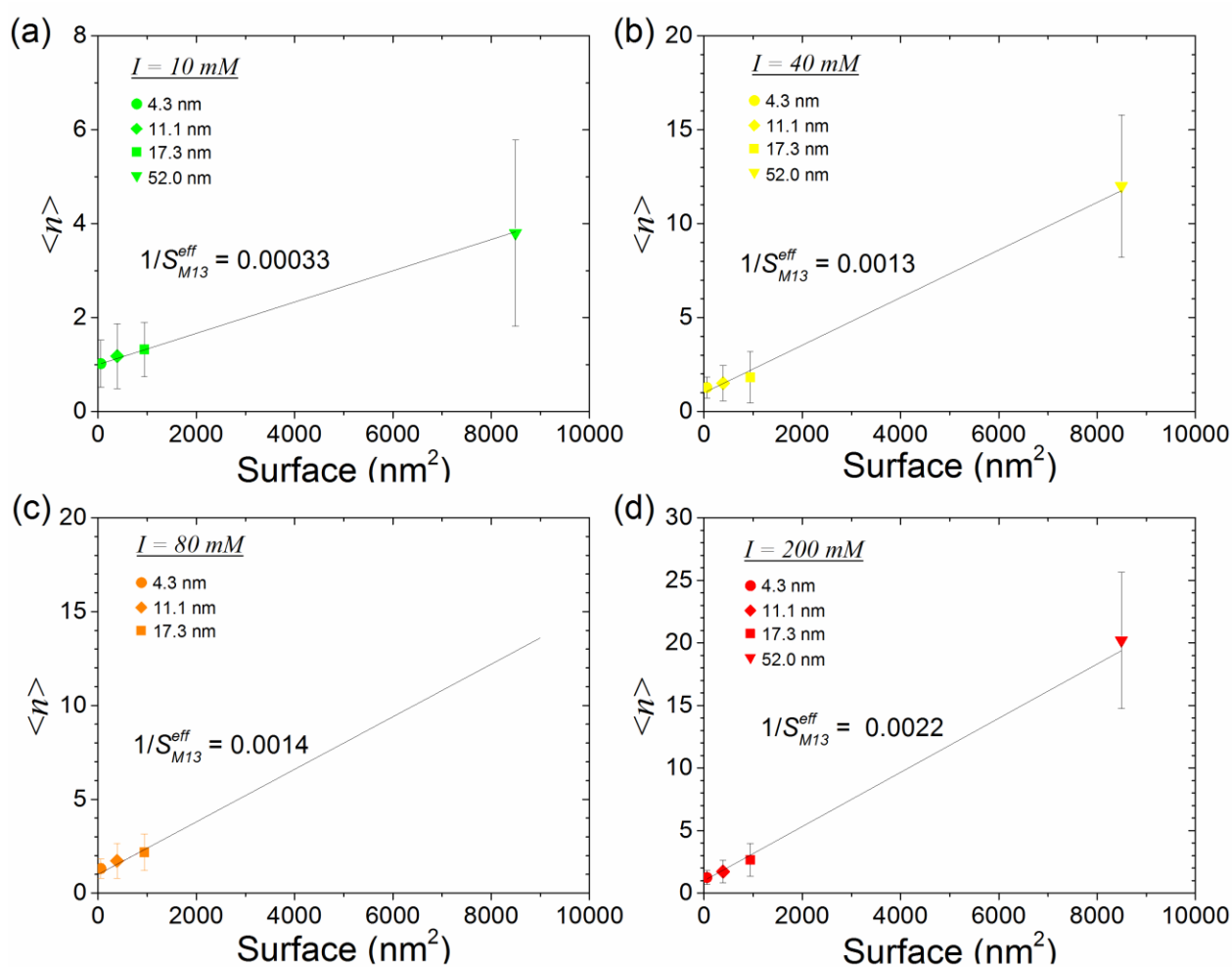


Figure 7: The average valency, $\langle n \rangle$, determined by the arithmetic mean from Figure 4, increases linearly with the surface area of AuNB at a given ionic strength. The corresponding lines are fittings by Equation 3 with a fixed intercept at $n = 1$. Slope for the fitting, $1/S_{M13}^{eff}$, increases with ionic strength. The error bars are the standard deviations obtained from Gaussian fits of distributions in Figure 4.

If only the highly charged viruses have an electrostatic dependence, then according to Equation (6), we can deduce the value of free parameter A . The effective area S_{M13}^{eff} at each ionic strength are obtained from the slope of fits in Figure 7, they are calculated to be 3004, 787, 714 and 463 nm² at ionic strength $I = 10, 40, 80$ and 200 mM, respectively. We then plot the effective area of proximal tip, S_{M13}^{eff} , as a function of ionic strength and fit it with Equation (6), as shown in Figure 8. The S_{M13}^{eff} decreases strongly in low ionic strength region (from $I = 10$ mM to 40 mM), and reaches plateau at high ionic strength ($I = 40, 80, 200$ mM). Even though the fit does not perfectly describe the effective area of proximal end, it still shows properly the variation of S_{M13}^{eff} with ionic strength. The numerical factor A is then obtained from the fit, which is $A = 8.9$.

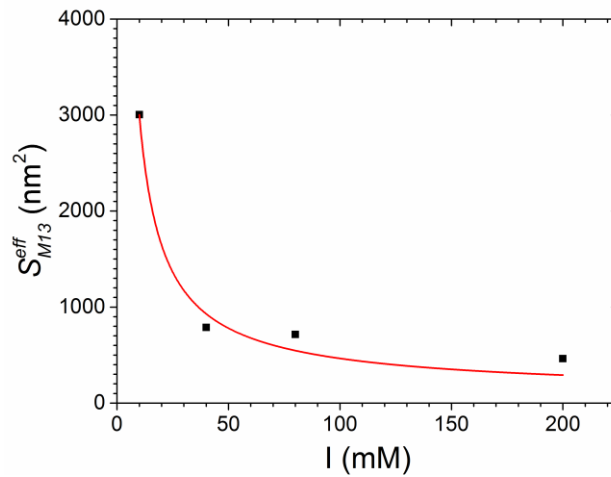


Figure 8: The free parameter A is obtained as 8.9 by fitting effective area, S_{M13}^{eff} , as a function of ionic strength, I , with Equation (6). The value of S_{M13}^{eff} is derived from the linear fits in Figure 7.

As shown in Equation 4, the factor A defines the effective size of proximal end of M13 viruses. This effective radius is larger than the bare radius of M13 virus (3.5 nm) even at a high ionic strength ($I = 200$ mM, $R_{M13}^{eff} = 9.6$ nm) where electrostatic interaction is strongly screened. It could be explained by the lateral extension at proximal end of the virus: the p3 proteins located at the proximal end of the viruses have a different size than the body, which makes this end has a bigger diameter than the body.

4.3.4 Mass production of AB₂ type colloidal molecules

The quantitative model we developed in previous section can be used for the mass production of colloidal molecules with a specific valency. Since the valency always shows a distribution, and the selectivity of the main obtained colloidal molecules decreases with increasing the valency, we choose to produce the simplest multivalent colloidal molecules, i.e., AB₂ types, to obtain highest yield. According to the model we have built, AuNBs of diameter 11.1 nm and 17.6 nm are both feasible to produce colloidal molecules of an average valency $\langle n \rangle = 2$. However, the width of valency distribution broadens with increasing the AuNB diameter, which means a decrease of selectivity of AB₂ types. Therefore, AuNBs of diameter 11.1 nm are chosen and we apply directly stoichiometric ratio ($1/\alpha = [M13C7C]_0/[AuNB]_0 = 2$).

For this mass production, the AuNB suspension of 25 mL was mixed with M13 viruses to a final virus concentration of 0.22 mg/mL. The reaction was conducted under stirring of 300 rpm at room temperature for 14 h. In order to avoid any aggregation of AuNBs, ionic strength of the mixture for the reaction was first chosen at $I = 10$ mM, and then increased to $I = 40$ mM. In order to improve the reaction efficiency, 2 mM TCEP was added as the last reaction step by dialysis. The obtained structures are then dialyzed against $I = 2$ mM Tris-HCl buffer for storage.

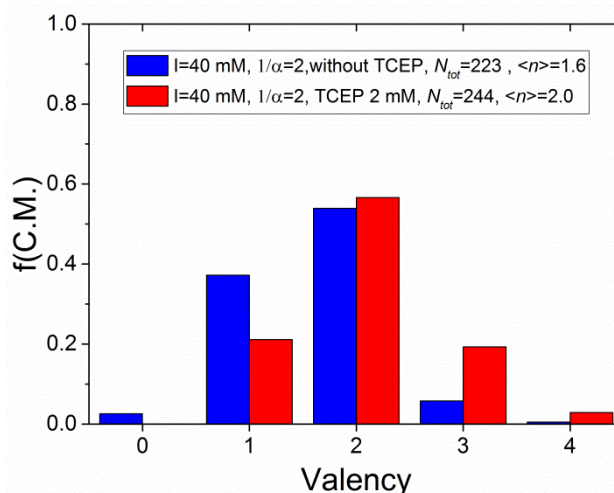


Figure 9: Mass production of AB₂ type colloidal molecules using 11.1 nm AuNBs with initial molar excess $1/\alpha = [M13C7C]_0/[AuNB]_0 = 2$ (stoichiometric ratio). The reaction is performed at $I = 40$ mM buffer and enhanced by adding 2 mM TCEP, yielding a majority of 57% AB₂ types. The fractions of colloidal molecules with a given valency is defined by $f(C.M.) = N/N_{tot}$, where N is the number of specific colloidal molecules and N_{tot} is total number of colloidal molecules including the free AuNBs.

The reaction shows a very high overall reaction efficiency between AuNBs and M13C7C viruses (Figure 9 blue columns), yielding a majority of AB_2 ($n = 2$) type colloidal molecules. Still, there exists free viruses and 37% AB type ($n = 1$) in the suspension. The average valency is 1.62, which is consistent with the theoretical value (1.42) within the error bar. We then improve the reaction by adding 2 mM TCEP. TCEP can efficiently break disulfide bridges, which makes the sulfur more exposed to AuNBs. Results (Figure 9, red column, and Figure 10) show significant decrease of fraction of AB types, indicating the improvement of the reaction between AuNBs and M13C7C by adding TCEP. Correspondingly, the average valency increases to $\langle n \rangle = 2$. However, the enhancement only shifts the distribution of obtained colloidal molecules to higher valency: yield of AB_2 type is only increased slightly, but fraction of AB_3 types grows significantly (6% to 19%).

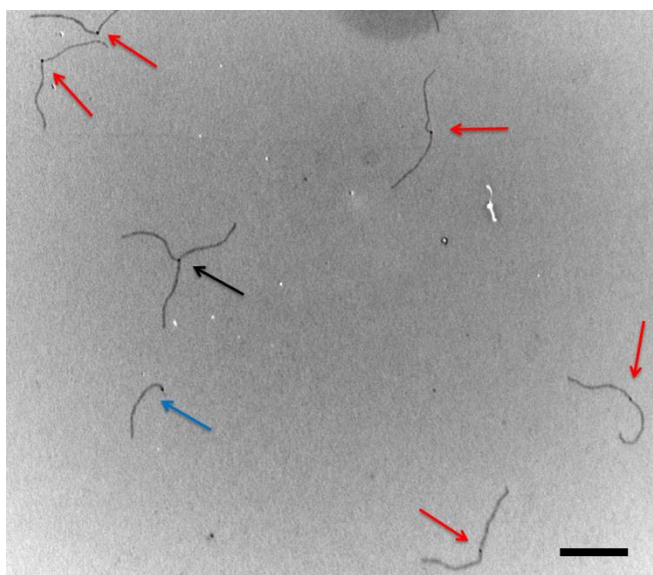


Figure 10: Transmission electron microscopy (TEM) image of the obtained colloidal molecules, including five AB_2 types (indicated by red arrows), one AB type (blue arrow) and one AB_3 type (black arrow). Scale bar is $1 \mu\text{m}$.

Finally, we achieved mass production of AB_2 type ($>10^{13}$ colloidal molecules) with a yield of 57% after adding 2 mM TCEP. In total, about 6 mg colloidal molecules are obtained, corresponding to 1×10^{14} objects, which is 1000 times more than the amount we produced for developing the model. It is enough to explore the bulk phase transitions and dynamics of colloidal diblocks with this big amount of AB_2 type colloidal molecules.

4.4 Conclusions

In this chapter, rod based colloidal molecules are created by assembling filamentous viruses with AuNB (Au nanobead), thanks to the covalent bond formed between Au and disulfides at the proximal end of M13C7Cviruses. Under the condition of a big initial excess of viruses, valency of the resulting colloidal molecules can be tuned by varying the diameter of AuNBs and the ionic strength.

The effect of surface area of AuNBs on valency is studied by using AuNB of diameter 4.3, 11.1, 17.3 and 50 nm. A linear dependence of valency on surface area of the AuNBs is found at a given ionic strength. Then influence of the effective area of proximal tip of M13 viruses is investigated. This effective area indicates the range of electrostatic repulsion between the virus proximal ends, which can be regulated by ionic strength through Debye length. A quantitative model is then built using surface area of AuNBs and ionic strength as variables, which accounts for assembling colloidal molecules with desired valency. Even though this model is quite simple to describe the factors that influence the valency, it still fits properly the experimental results. Using this model, we produce AB_2 type colloidal molecules of mass amount, which can be used for study of phase transitions and dynamics (see Chapter 5).

Overall, we present a simple and efficient method to create robust rod based multivalent colloidal molecules whose valency can be continuously tuned. This method can be used for assembling not only molecules analogs, but also bulk colloidal phases of fundamental and practical interest.

4.5 References

- [1] J. Turkevich, P. C. Stevenson, and J. Hiller. A Study of the Nucleation and Growth Processes in the Synthesis of Colloidal Gold. *Discuss. Faraday Soc.*, 1951, 11: 55–75.
- [2] C. Ziegler and A. Eychmüller. Seeded growth synthesis of uniform gold nanoparticles with diameters of 15-300 nm. *J. Phys. Chem. C*, 2011, 115: 4502–4506.
- [3] N. G. Bastús, J. Comenge, and V. Puntes. Kinetically controlled seeded growth synthesis of citrate-stabilized gold nanoparticles of up to 200 nm: Size focusing versus ostwald ripening. *Langmuir*, 2011, 27: 11098–11105.
- [4] S. K. Sivaraman, S. Kumar, and V. Santhanam. Room-temperature synthesis of gold nanoparticles - Size-control by slow addition. *Gold Bull.*, 2010, 43: 275–286.
- [5] T. Hendel, M. Wuithschick, F. Kettemann, A. Birnbaum, K. Rademann, and J. Polte. In Situ

Determination of Colloidal Gold Concentrations with UV–Vis Spectroscopy: Limitations and Perspectives. *Anal. Chem.*, 2014, 86: 11115–11124.

- [6] T. Ahmad. Reviewing the tannic acid mediated synthesis of metal nanoparticles. *J. Nanotechnol.*, 2014, 2014: 1–11.
- [7] L. Onsager. The Effects of Shape on the Interaction of Colloidal Particles. *Ann. N. Y. Acad. Sci.*, 1949, 51: 627–659.

Chapter 5

Heterobifunctional colloidal diblocks from directional self-assembly of rod-shaped viruses

Contents

5.1	Introduction	108
5.2	Materials and Methods.....	110
5.2.1	Labeling of M13C7C viruses with red and green fluorescent dyes	111
5.2.2	Preparation of Scepter-like r-M13–AuNB colloidal molecules	111
5.2.3	Self-assembly of bicolored virus based diblocks.....	112
5.2.4	Diffusion coefficients and angle fluctuations of the diblocks	113
5.3	Results and Discussion.....	114
5.4	Conclusions	123
5.5	References	124

5.1 Introduction

As described in the general introduction of the thesis, the M13 viruses can be used as building blocks for colloidal molecules and functional materials. In previous chapters, we have already discussed the methodologies to assemble M13 viruses into colloidal molecules and the tuning of their valency. In this chapter, we address the second usage of the filamentous viruses to synthesize functional nanomaterials.

The M13 viruses have been utilized as building blocks to synthesize functional materials mainly through grafting either on their bodies or at their tips. Prior studies have succeeded in grafting different kinds of materials on the body of fd/M13 viruses, including Au, ZnS, CdS, etc., [1]–[5], by phage display on p8 proteins. The alternative chemical functionalization of p8 protein with cysteines or DNA also serves as an efficient pathway to graft nanomaterials on virus surface [6], [7]. Consequently, metallic or conductive nanowires are obtained, which can be used as battery electrodes [4], [5], [8]. Meanwhile, binding on p3 protein at the tip of viruses has been explored and employed in binding semi-conductive nanocrystal and quantum dots. Then, nanofilms of these materials can be prepared after the self-organization of M13 viruses into smectic layers [9]–[11]. Thanks to the selective binding of various nanomaterials, M13 viruses have been used as building blocks in different research fields, such as optoelectronics, drug-carrying, energy storage, etc.

In this chapter, we combine the grafting of M13 viruses both on their body and at their tip, to assemble heterobifunctional diblocks. Specifically, two different functional groups or materials are grafted on the virus bodies, respectively, and then linked via Au nanobead (AuNBs). As a proof-of-concept experiment, red and green fluorescent dyes are chosen to be labeled on the body of M13C7C viruses separately. Consequently, bicolored diblocks are synthesized, as shown in Figure 1. The detailed procedures and experimental conditions will be presented in this chapter. Since the obtained bicolored diblocks can be visualized by fluorescence microscopy, we will also show their dynamics in isotropic and nematic phases, by tracking each block (red and green viruses) simultaneously. Moreover, the influence of the flexible linking point (due to the flexible p3 proteins) is studied by characterization of fluctuations of the angle between red and green blocks.

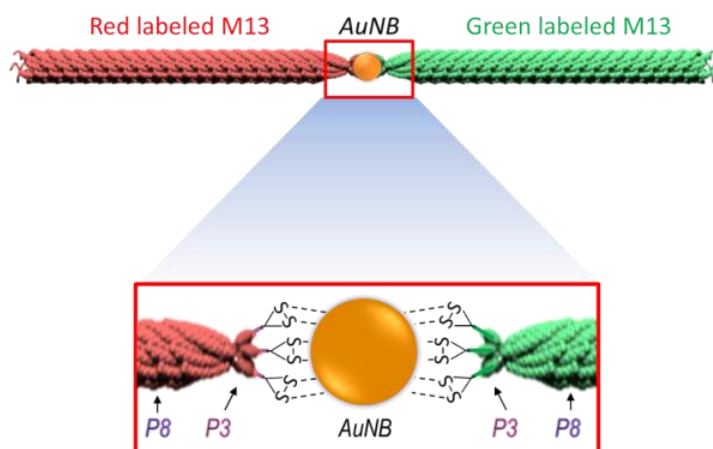


Figure 1: Illustration of bicolored colloidal diblocks based on M13C7C viruses. This heterobifunctional diblock is synthesized by linking two independently labeled M13C7C viruses via an Au nanobead (AuNB).

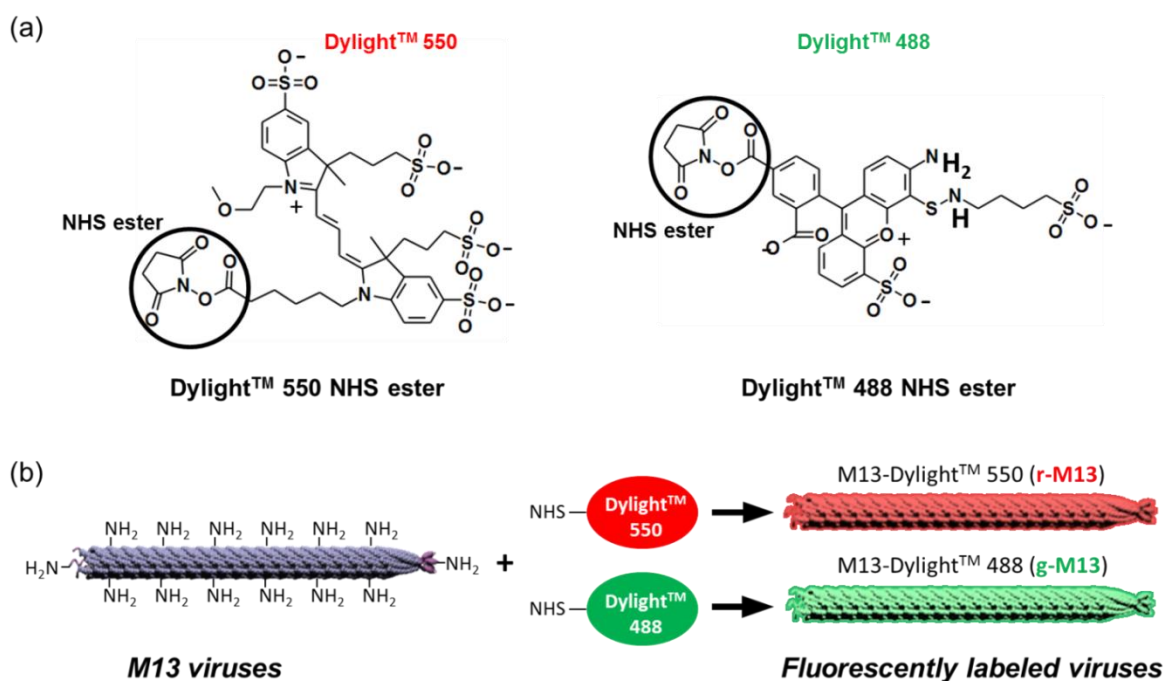


Figure 2: (a) Chemical structures of red and green fluorescent dyes: Dylight™ 550 NHS ester and Dylight™ 488 NHS ester. The active group N-Hydroxysuccinimide ester (NHS ester) is indicated by a circle. Both fluorescent dyes are negatively charged, and they can increase the charge density when grafted on the virus surface. (b) Schematic representation of labeling steps. The NHS groups of the dyes can react with amines on the surface of viruses, resulting in red or green fluorescently labeled viruses.

5.2 Materials and Methods

M13C7C viruses and 11.1 nm tannic acid capped AuNB are used for the synthesis of bicolored diblocks. Viruses are produced by standard biological method [12], and AuNBs are purchased from nanoComposix. Characterizations of the size and concentration of the AuNBs have been shown in Chapter 4. The Red fluorescent dyes (Dylight™ 550 NHS ester) and the green fluorescent dyes (Dylight™ 488 NHS ester) are purchased from ThermoFisher Scientific. Chemical structures of both fluorescent dyes are presented in Figure 2a.

The process to create the bicolored diblocks consists of three steps (Figure 3), which are labeling of the M13 viruses separately with red and green fluorescent dyes, conjugation of the red labeled viruses with AuNB at their proximal end, and assembly with green labeled viruses. Detailed methods are described as below:

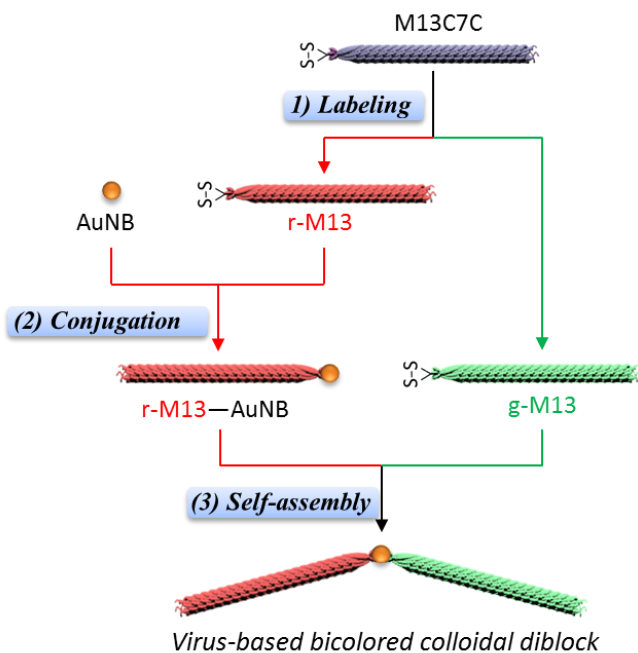


Figure 3: Schematic representation of the key steps to produce bicolored virus-based diblocks, including: (1) full body labeling of M13C7C with red and green fluorescent dyes, respectively, obtaining the correspondingly r-M13 and g-M13; (2) conjugation between r-M13 and an 11.1 nm AuNB at the proximal end, forming a AB type Scepter-like r-M13–AuNB particle; (3) Self-assembly of r-M13–AuNB with one g-M13 virus into a bicolored colloidal diblock.

5.2.1 Labeling of M13C7C viruses with red and green fluorescent dyes

Two batches of M13C7C viruses were fully labeled on their surfaces with red dyes (Dylight™ 550 NHS ester) and green dyes (Dylight™ 488 NHS ester) respectively (Figure 2b), through the $-NH_2$ group of terminal amino acids and Lysine of p8 proteins [13]. Specifically, M13C7C viruses at 2 mg/mL (6.5×10^{13} particles/mL) were dialyzed against PBS buffer (I = 200 mM, pH 7.8), and then mixed with red or green fluorescent dyes which were predissolved in Dimethylformamide (DMF). The excess of fluorescent dyes is 3 per protein with particular care that volume of DMF has to be less than 20% to avoid any damage of viruses. Reaction was conducted under stirring at 300 rpm for 2 hours at room temperature. The resulted suspensions of red labeled M13C7C (r-M13) and green labeled M13C7C (g-M13) were then dialyzed extensively against Tris·HCl buffer (I = 10 mM, pH 8.2) to remove free dyes, and stored at 4 °C.

5.2.2 Preparation of Scepter-like r-M13–AuNB colloidal molecules

The preparation of Scepter-like r-M13–AuNB structures is performed by mixing r-M13 viruses with 11.1 nm tannic acid capped AuNB in a Tris buffer. In order to obtain a high yield of AB types and avoid formation of AB₂ types (two viruses bind to one AuNB), an initial molar ratio $\alpha = [AuNB]_0/[M13]_0 = 3$ was applied (excess of AuNBs). Besides, virus concentration in this conjugation should be less than the overlapping concentration of M13 viruses, C^* , which is the concentration when two viruses start to overlap with each other. The C^* of M13 viruses is calculated by assuming close packing spheres (having a volume fraction of 0.74) of diameter corresponding to one virus length, given by $C^* = \frac{0.74 \cdot M_w}{\frac{4}{3} l^3 \cdot N_A}$, where M_w and l are molecule weight and length of filamentous virus, respectively. For M13 virus, $M_w = 1.85 \times 10^{10}$ mg/mol, $l = 1 \mu\text{m}$, then overlapping concentration is calculated to be $C^* = 0.043$ mg/mL. Experimentally, the virus concentration is settled slightly smaller than C^* , at 0.040 mg/mL.

The ionic strength of the buffer is chosen at I = 40 mM to favor this reaction and avoid aggregation of AuNBs, according the charge properties of labeled viruses and colloidal stability of AuNBs. In principle, the higher the ionic strength is, the better we favor the reaction between AuNBs and M13 viruses, until AuNBs lose their colloidal stability (aggregation at I = 80 mM). For reaction between bare M13 viruses and tannic acid capped AuNBs, high efficiency could be achieved using an ionic strength I = 10 mM with a molar excess of 3 (details discussed in

Chapter 3). However, a higher ionic strength ($I = 40$ mM) has to be used for these body labeled M13. Because the negatively charged fluorescent dyes (Figure 2a) on the body of M13 viruses increase the overall charge density, so higher ionic strength is needed to screen the electrostatic repulsion between r-M13 and the negative charged tannic acid stabilized AuNBs.

Before mixing, The AuNB (11.1 nm, stabilized with tannic acid, 3.9×10^{12} particles/mL, nanoCompsix) suspension was first dialyzed against Tris·HCl ($I = 40$ mM, pH 8.2) buffer, and then mixed with r-M13 (Figure 3, step 2). Because the volume of virus dispersion is very small compared to AuNB suspension (volume ratio $V_{\text{AuNB}}/V_{\text{M13}} \sim 40$), final ionic condition of the mixture is mainly given by suspension of AuNBs, which is $I = 40$ mM.

Then, this one-step conjugation between AuNB and r-M13 virus was performed under stirring at 300 rpm for 14 hours at room temperature, resulting in Scepter-like colloidal molecules (Figure 4). Afterwards, centrifugations were used to purify (remove free AuNBs) and concentrate the Scepter-like colloidal molecules. In order to avoid aggregation of AuNBs during the centrifugation steps, ionic strength of the resulted suspension was decreased by dialysis against deionized water. Conditions for centrifugation (acceleration, time) are chosen according to the theoretical calculations which are presented in *Appendix II*. Specifically, the unreacted 11.1 nm AuNBs were removed by performing 5 rounds of centrifugation at 12,000 g for 45 min. Scepter-like colloidal particles in the supernatant were collected and then concentrated by ultracentrifugation at 250,000 g for 1 hour. Pellet of Scepter-like colloidal particles after ultracentrifugation was redispersed completely in deionized H₂O to virus concentration of about 1.5 mg/mL. This concentration was estimated by assuming that we maintain the mass of viruses. (Spectrophotometry cannot be used to determine the concentration of Scepter-like r-M13–AuNB, because big errors arise from the overlay of UV-Vis absorption of AuNBs, M13 viruses and fluorescent dyes at 269 nm.)

5.2.3 Self-assembly of bicolored virus based diblocks

Bicolored virus based diblocks were obtained by assembling Scepter-like colloidal particles (r-M13–AuNB) with green dyes labeled M13 viruses (g-M13) in solution, as shown in Figure 3, step 3. Virus concentration used in this step should be higher than overlapping concentration of M13 viruses. Therefore, practically virus concentration of about 1 mg/mL is used. Since the

spectrophotometry is not able to determine precisely concentration of the Scepter-like colloidal particles, stoichiometric ratio between r-M13–AuNB and g-M13 was achieved by mixing step by step the 2 blocks with quantitative checking (particles counting) by fluorescence microscopy. The experimental conditions of the self-assembly were optimized (Figure 6), specifically by increasing ionic strength to $I = 60$ mM to screen electrostatic repulsion between AuNB and viruses, and adding 2 mM TCEP to break the disulfide group that makes the sulfur more exposed. Reactions were conducted by stirring at 300 rpm at room temperature for 14 hours. The obtained were dialyzed against $I = 2$ mM Tris·HCl buffer for storage.

5.2.4 Diffusion coefficients and angle fluctuations of the diblocks

The diffusion coefficient of the diblocks is measured in three different conditions: in deep isotropic phase (dilute regime; virus concentration of $C_v = 5.0 \times 10^{-4}$ mg/mL); in nematic matrix of M13KE ($C_v = 12$ mg/mL); in nematic phase of mixture consisting mainly of similar structures AB_2 types (57%) (but having also AB types (20%), and AB_3 types (19%); $C_v = 12$ mg/mL, from the mass production in Chapter 4). For the analysis in nematic phase, only tracer amount of bicolored diblocks are added (ratio $\sim 1:10^5$).

Cells for optical observations were prepared with glass slide and coverslip which were cleaned beforehand with sulfochromic acid and rinsed with large amount of deionized water. Double stretched parafilm is used as spacer to control the thickness at around 10 μ m. The fluorescent labeled viruses are visualized via an inverted microscope (IX-71, Olympus) equipped with 100 \times objective (numerical aperture 1.4, Olympus) and a Neo SCMOS camera. To simultaneously record green and red fluorescence images, an optical splitter setup (Optosplit II, Cairn Research) was used to divide each image into two channels, thanks to an appropriate dichroic beamsplitter and band pass filters. The respective images were then overlaid manually with a precision of one pixel. Movies that are used for the analysis of diffusion coefficients are recorded at a frame rate of 333 fps (exposure time plus readout time is 3 ms) in isotropic phase and 50 fps (exposure time plus readout time is 20 ms) in nematic phase. The corresponding time duration of the movies for isotropic phase is 1.5 s and for nematic phase is 10 s. The particle tracking, mean square displacement (MSD) and mean square angular displacement (MSA) analysis were done with a Matlab algorithm [14].

5.3 Results and Discussion

The conjugation between r-M13 and tannic acid capped AuNBs is efficient. As expected, the highly regio-selective binding only occurred at one tip of M13, forming Scepter-like r-M13–AuNB colloidal particles, as shown in the scheme and TEM images in Figure 4. Fractions of M13 viruses in different structures, $f(M13C7C) = N_v/N_{tot}$, are presented in Figure 5. N_v is number of viruses involved in given structure and N_{tot} is total virus number. A high overall yield is obtained, with 95% of viruses are bound to AuNBs, including 89% of viruses involved in the AB type Scepter-like r-M13–AuNB structures and 6% of viruses in AB₂ types. This overall yield is similar to what we obtained using 17.3 nm AuNBs (93%) with similar ionic strength and molar excess (Chapter 3, Figure 16). Nevertheless, a higher selectivity of AB type structure (89%) is achieved, compared to 76% when 17.3 nm AuNBs is used. This improvement is due to the decrease of the AuNB diameter, which reduces the possibility of two viruses reacting with same AuNB. This high yield of AB type structures (red blocks, 89%) provides a suitable precondition for self-assembly with the green blocks (g-M13).

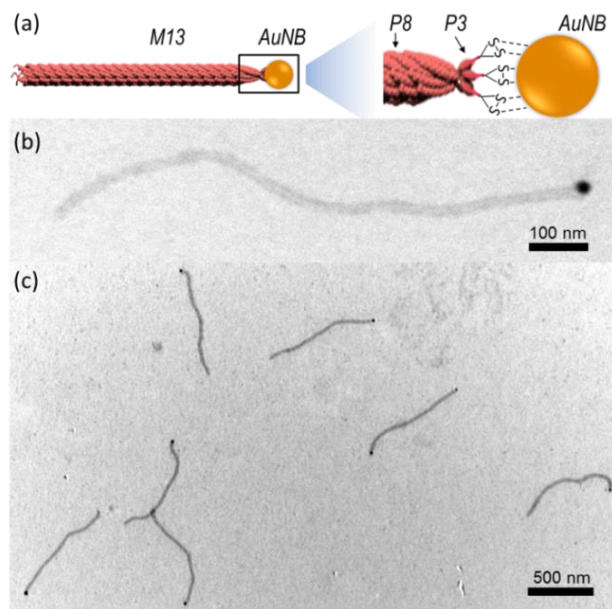


Figure 4: Scepter-like r-M13–AuNB colloidal particles formed by grafting AuNB to one end of fluorescently labeled M13 viruses. (a) Scheme of the Scepter-like r-M13–AuNB particle. The exposed disulfide groups at one end of the virus can form weak covalent bond with AuNBs, resulting in very stable colloidal molecules. TEM images of a Scepter-like colloidal molecule (b) and large field of view image where 7 Scepter-like r-M13–AuNB particles (c) are also shown.

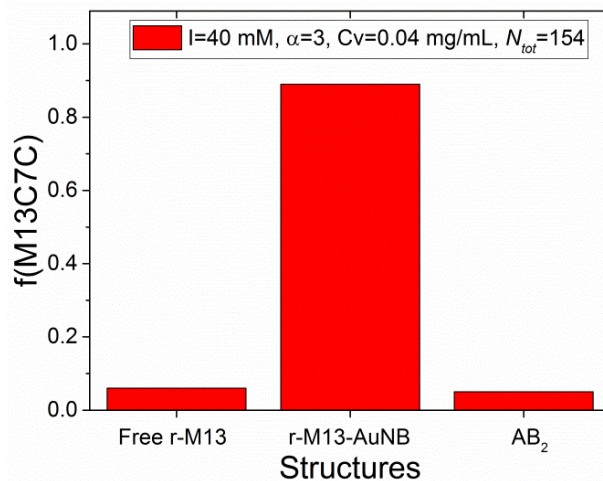


Figure 5: Conjugation between r-M13viruses and AuNBs under conditions of ionic strength $I = 40$ mM, molar excess $\alpha = 3$, and viruses concentration $C_v = 0.04$ mg/mL. A high yield of 89% AB type r-M13–AuNB structures is obtained. The yield is characterized by the fraction of viruses involved in each structure, $f(\text{M13C7C}) = N_v/N_{\text{tot}}$, where N_v is number of viruses involved in this structure and N_{tot} is total virus number.

The assembly between r-M13–AuNB colloidal particles and g-M13 is performed at stoichiometric molar ratio. Except for the desired bicolored diblocks, other kinds of byproducts can also be formed, like homocolored diblocks and star-like structures, especially when we increase the ionic strength too much that causes the partial aggregation of AuNBs.

This self-assembly is less efficient than the formation of AB₂ type structures. As shown in Figure 9 of Chapter 3, under the conditions of excess of 2 viruses per AuNB, ionic strength $I = 40$ mM, about 50% AB₂ type colloidal molecules are obtained. But for the self-assembly between r-M13–AuNB colloidal particles and g-M13 at same conditions, more than 70% viruses are not assembled, including 38% r-M13–AuNB structures and 34% g-M13 viruses (Figure 6a). The low efficiency (19% bicolored diblocks) could be attributed to electrostatic reasons. The labeled viruses are more negatively charged than raw viruses, so the electrostatic repulsion is certainly bigger, which impedes the assembly. Note that small fractions of byproducts have already formed (5% of homocolored diblocks and 4% of star-like structures).

In order to improve the efficiency of the self-assembly step, we optimize the reaction buffer by adding TCEP and increase slightly the ionic strength (too high ionic strength may cause aggregation of AuNBs).

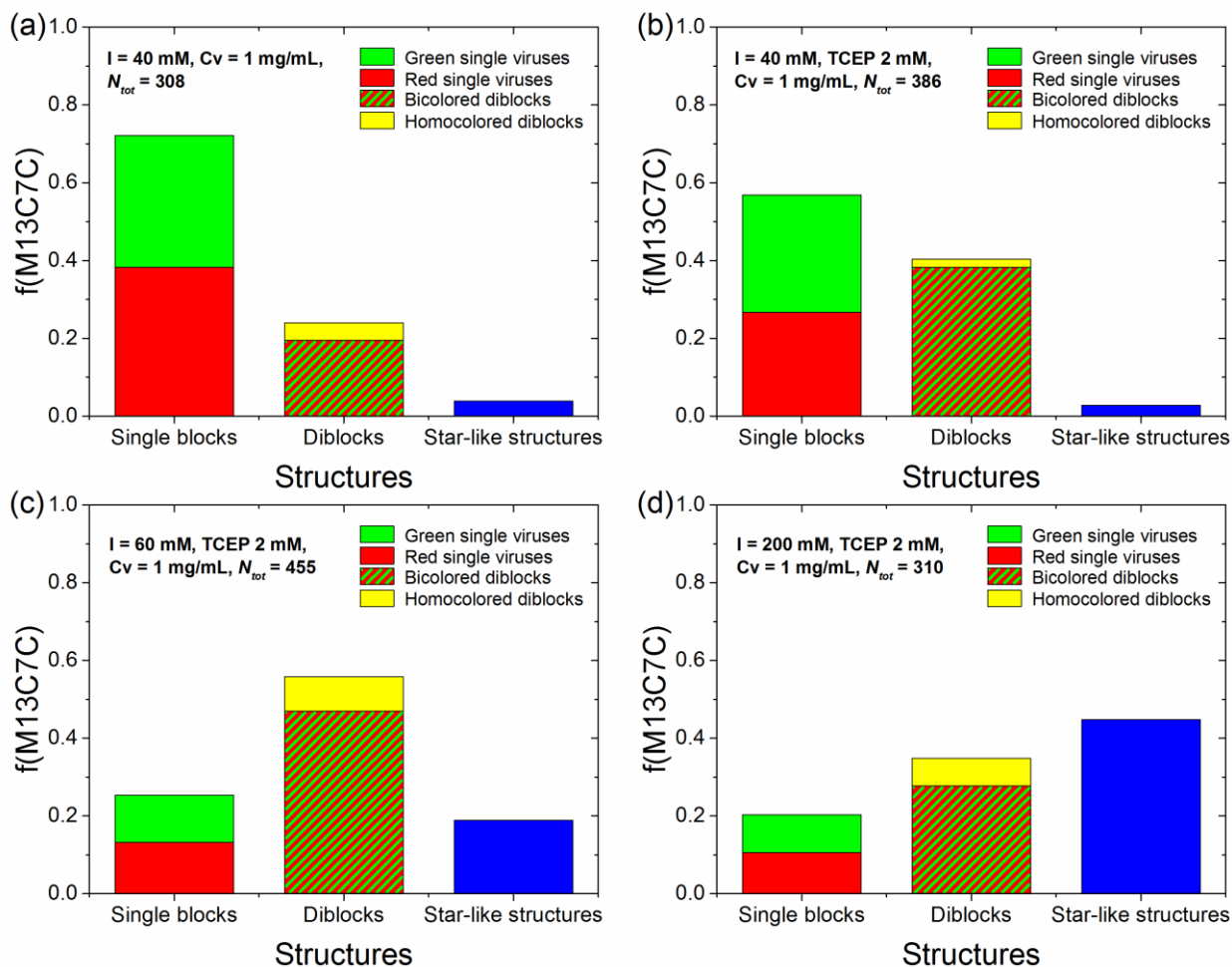


Figure 6: Optimization of the ionic conditions for self-assembly of bicolored diblocks. The yield for each condition is presented by the fractions of different structures (single blocks, diblocks and star-like structures (≥ 3 viruses tip linked)), and the fraction is calculated by $f(M13C7C) = N_v/N_{tot}$, where N_v is number of viruses involved in this structure and N_{tot} is total virus number. A highest yield of bicolored diblocks is obtained under the condition of $I = 60 \text{ mM}$ and with TCEP (2 mM) in presence, which yields 47% bicolored diblocks. Virus concentration is fixed at $C_v = 1.0 \text{ mg/mL}$ for all conditions. Fractions are calculated based on the counts by fluorescence microscopy.

It is reported the disulfides and thiols are both able to form weak covalent bond with Au [15]–[17]. The adding of TCEP could reduce the disulfide groups at the proximal tip of g-M13 virus into thiols that make the sulfurs more exposed to the environment, therefore increasing the binding efficiency to AuNBs. The results of self-assembly in presence of 2 mM TCEP is shown in Figure 6b. Compared with the assembly without TCEP, efficiency after adding TCEP improves. Specifically, the yield of diblocks increases from 24% to 40% with bicolored ones rising from

19% to 38%. Since ionic strength is not increased in this case, the fraction of byproducts doesn't grow. But there still exist a big amount of unreacted g-M13 viruses (30%) and r-M13–AuNB structures (27%) in the sample, so we continue to optimize the self-assembly by increasing slightly the ionic strength.

Ionic strength of the buffer for the self-assembly is first increased to 60 mM and then to 200 mM, still keeping 2 mM TCEP in presence. Results after ionic strength is increased to 60 mM are shown in Figure 6c. The efficiency of the assembly is further improved at this ionic strength. The unreacted r-M13–AuNB structures and g-M13 decrease to 13% and 12%, respectively. As a result, fraction of bicolored diblocks increases to 47%. However, the fractions of byproducts also increase. In this condition, we obtain 9% of homocolored dimers and 18% of star-like structures, which is much higher than ionic strength $I = 40$ mM (less than 10%).

At ionic strength $I = 60$ mM, partial aggregation of AB type r-M13–AuNB structures already occurs in the suspension, leading to an increase of the byproducts. Therefore, experimentally the ionic strength should not exceed this value. This is proved by the results obtained at $I = 200$ mM (Figure 6d). At this ionic strength, more than half viruses are involved in the aggregated byproducts, with a yield of bicolored diblocks less than 30%.

In summary, the ionic conditions for the assembly between r-M13–AuNB structures and g-M13 have been optimized to $I = 60$ mM, with 2 mM TCEP in presence. And the corresponding yield of bicolored diblocks we obtained is 47%.

These bicolored diblocks composed of one red and one green blocks (M13C7C viruses) can be visualized at single particle level by fluorescence microscopy, as shown in Figure 7a-b. The linker between two blocks, AuNB, even though cannot be visualized by fluorescence microscopy, is easily observed by TEM, as indicated by red arrows in Figure 7c-d. Tracer amount of these bicolored diblocks can be used for the investigation of phase transitions and dynamics of AB_2 types in the bulk phase. Furthermore, we can explore not only the dynamics of red and green blocks at the same time, but also the fluctuations of angle between them.

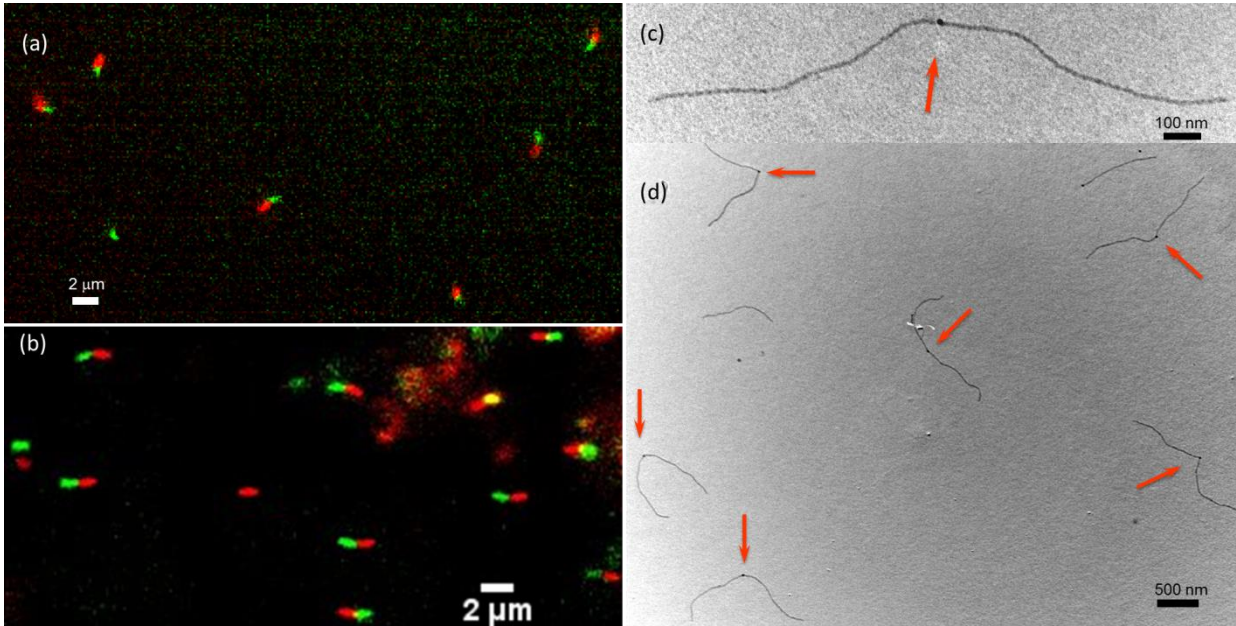


Figure 7: Virus based bicolored diblocks observed by optical fluorescence microscopy and transmission electron microscopy (TEM). Fluorescence images of large field of view display the dual labeling of several bicolored diblocks in isotropic phase (a) and nematic matrix of M13KE viruses (b). The contrast of the diblocks is lower in isotropic phase than nematic phase due to their stronger Brownian diffusion. In the matrix of M13KE viruses, the bicolored diblocks are mixed at a ratio of $1: 10^5$. AuNBs, indicated by red arrow in TEM images (c) and (d), are observed as linker of the diblocks. (d) Overall TEM images containing 6 diblocks.

The relationship between translational diffusion coefficient (D) of colloidal rods and the corresponding mean square displacement (MSD) is described as

$$MSD_{\parallel,\perp}(t) = 2 \cdot D_{\parallel,\perp} \cdot t^\gamma \quad (1)$$

Therefore, in the following part, we analyze the MSD of the green and red blocks of the diblocks, respectively, and then use them to deduce the corresponding diffusion coefficients, in both isotropic and nematic phases. Because we didn't separate the diblocks (~50%), the r-M13-AuNB (~13%) and the single g-M13 (~13%) from the obtained products, diffusion coefficients of all these structures are analyzed and compared at the same time under exactly the same experimental conditions.

The bicolored diblocks are characterized by both red and green blocks. Since they are linked, they should show the same MSD and diffusion coefficient. Also, in isotropic phase, the

diffusion coefficients of the diblocks parallel and perpendicular to the director of the viruses are supposed to be equal, $D_{\parallel} = D_{\perp}$. These theoretical predictions are confirmed by the experimental results. The parallel and perpendicular MSD of red and green blocks in the isotropic phase are presented in Figure 8; corresponding diffusion coefficients are calculated from the fits of MSD (Table 1). As shown, both red and green blocks parallel and perpendicular to the director of viruses have the same diffusion coefficient within the error bar, which are about $D_{\parallel,\perp} = 1 \mu\text{m}^2/\text{s}$. As comparison, the single viruses (g-M13) that have length half of the diblocks show a diffusion coefficient of $D_{\parallel,\perp} \approx 2 \mu\text{m}^2/\text{s}$. This value is about twice compared to the diblocks.

In the ideal infinitely dilute solution, the diffusion coefficient of colloidal stiff rods equals to

$$D = \frac{k_B T \ln(L/d)}{3\pi\eta L} \quad (2)$$

where k_B is Boltzmann constant; T is temperature; η is viscosity of the solution; L and d are length and diameter of the rod, respectively. From the expression, we see that the diffusion coefficient is proportional to the logarithm of the aspect ratio of the rod over its length, which is

$$D \propto \frac{\ln(L/d)}{L} \quad (3)$$

For our system, the diameter of viruses is 7 nm; the lengths of diblocks and single viruses are 2 and 1 μm , respectively. The contribution of AuNBs to the length of diblocks can be neglected. Theoretically, the diffusion coefficient of single viruses is 1.75 times higher than the diblocks according to Equation (3). This is approximately consistent to our experimental results, with slight discrepancy probably from the flexible linking point (due to the flexibility of p3 proteins). Meanwhile, the r-M13–AuNB structures show slightly lower diffusion coefficients than green single viruses, which could be due to the AuNBs at their proximal ends that slow down the kinetics. Besides, the diffusion exponents we obtained are always about $\gamma = 1$, which indicates a diffusive behavior of the particles.

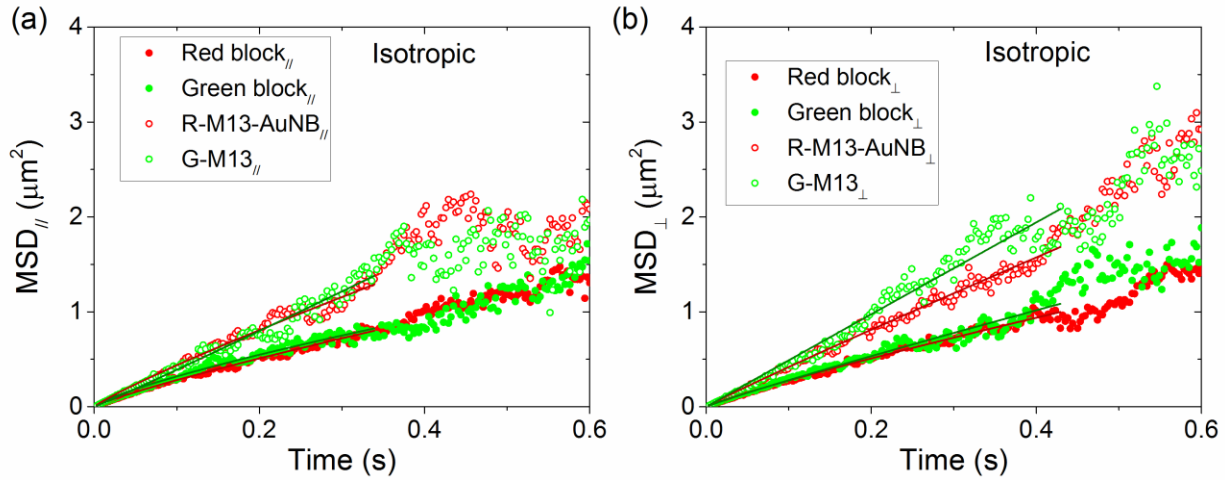


Figure 8: Mean square displacement (MSD) of virus-based bicolored diblocks in dilute isotropic phases parallel (a) and perpendicular (b) to the director of the viruses. Virus concentration is $C_v = 5 \times 10^{-4}$ mg/mL. Both red and green blocks are tracked and analyzed (full symbols), and their MSDs show similar value. For a comparison, the MSD of single viruses (g-M13) and AB types (r-M13–AuNB) in the same conditions are also presented (empty symbols). In order to obtain the diffusion coefficients, the MSDs are fitted with allometric function according to Equation (1).

Table 1: Diffusion coefficients and corresponding diffusion exponents for diblocks, single viruses and AB types in isotropic phase. They are obtained from the fits of MSD in Figure 8.

		Parallel		Perpendicular	
		$D_{ }$	γ	D_{\perp}	γ
Diblocks	Red	1.01	0.86	1.05	0.88
	Green	0.96	0.78	1.19	0.93
	r-M13–AuNB	1.68	0.88	1.89	0.96
	g-M13	2.11	1.03	2.42	0.99

Compared to isotropic phase, the kinetics in the nematic phase is much slower. And diffusion coefficient in the parallel direction is much higher than the perpendicular direction. For the diblocks in the matrix of M13KE viruses, we obtain a diffusion coefficients of $D_{||} = 0.53 \mu\text{m}^2/\text{s}$, $D_{\perp} = 0.069 \mu\text{m}^2/\text{s}$ (Figure 9, Table 2) at virus concentration of 12 mg/mL. The anisotropy in diffusion of diblocks in nematic matrix is $D_{||}/D_{\perp} \approx 7$. Being the same as in isotropic phase, the single viruses (g-M13) show about twice higher diffusion coefficients than diblocks in both parallel and perpendicular directions (Table 2). Also, the r-M13–AuNB structures have slightly

smaller diffusion coefficients than single viruses (g-M13). The anisotropy in diffusion of single viruses and M13–AuNB show the same value as diblocks, which is $D_{\parallel}/D_{\perp} \approx 7$.

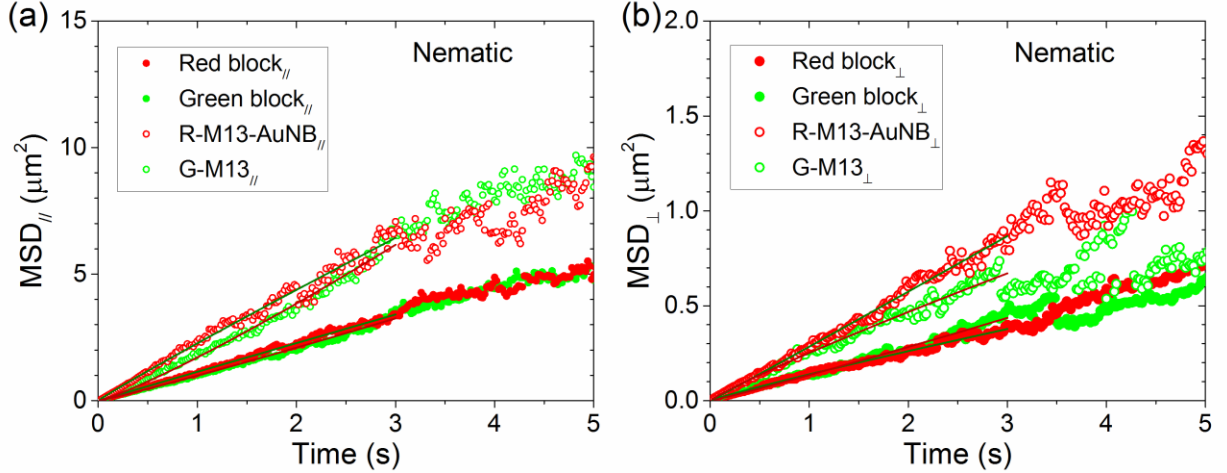


Figure 9: Mean square displacement (MSD) of virus-based bicolored diblocks in nematic matrix of M13KE parallel (a) and perpendicular (b) to the director of the viruses. Virus concentration is $C_v = 12$ mg/mL. Both red and green blocks are tracked and analyzed (full symbols), and their MSDs show similar value. For a comparison, the MSD of single viruses (g-M13) and AB types (r-M13–AuNB) in the same condition are also presented (empty symbols). In order to obtain the diffusion coefficients, the MSDs are fitted with allometric function according to Equation (1).

Table 2: Diffusion coefficients and corresponding diffusion exponents for diblocks, single viruses and AB types in nematic matrix of M13KE. They are obtained from the fits of MSD in Figure 9.

		Parallel		Perpendicular	
		D_{\parallel}	γ	D_{\perp}	γ
Diblocks	Red	0.49	1.08	0.068	1.06
	Green	0.57	1.00	0.070	0.91
	r-M13–AuNB	0.86	1.17	0.126	0.89
	g-M13	1.13	0.95	0.142	1.01

For a nematic phase of mixture of AB types (20%), AB₂ types (57%), and AB₃ types (19%), (which is from the mass production in Chapter 4), the parallel diffusion coefficient of diblocks is similar to diblocks in nematic matrix of single M13KE viruses ($D_{\parallel} = 0.5 \mu\text{m}^2/\text{s}$). But the perpendicular diffusion are more hindered, for which a coefficient of $D_{\perp} = 0.035 \mu\text{m}^2/\text{s}$ is found. Therefore, the anisotropy in the diffusion increases to $D_{\parallel}/D_{\perp} \approx 14$. However, we didn't observe a

big difference between r-M13–AuNB and single green viruses (the perpendicular diffusion coefficient of r-M13–AuNB is even slightly higher than g-M13).

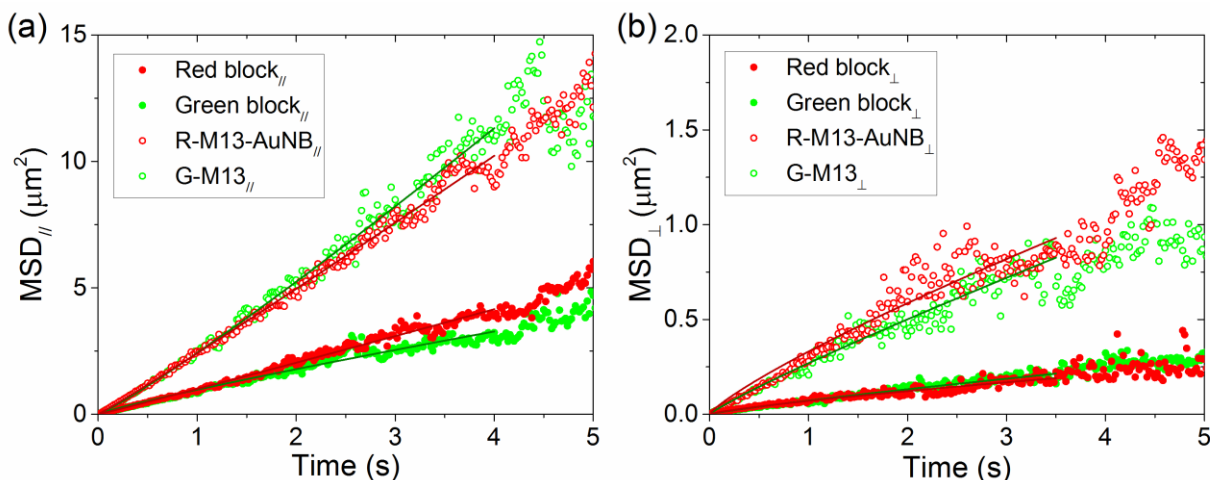


Figure 10: Mean square displacement (MSD) of virus-based bicolored diblocks in nematic phase of mixture of AB types (20%), AB₂ types (57%), and AB₃ types (19%). Virus concentration is $C_v = 12$ mg/mL. MSD parallel and perpendicular to the director of the viruses are presented in (a) and (b), respectively. Both red and green blocks are tracked and analyzed (full symbols), and their MSDs show similar value. For a comparison, the MSD of single viruses (g-M13) and AB types (r-M13–AuNB) in the same condition are also presented (empty symbols). In order to obtain the diffusion coefficient, the MSDs are fitted with allometric function according to Equation (1).

Table 3 Diffusion coefficients and corresponding diffusion exponents for diblocks, single viruses and AB types in nematic phase. They obtained from the fits of MSD in Figure 10.

		Parallel		Perpendicular	
		$D_{ }$	γ	D_{\perp}	γ
Diblocks	Red	0.5	1.02	0.035	0.79
	Green	0.49	0.88	0.036	0.86
r-M13–AuNB		1.20	1.04	0.166	0.82
g-M13		1.21	1.11	0.135	0.89

By plotting the mean square angles (MSA) of bicolored diblocks, we can analyze the angle fluctuation between red and green blocks. The flexibility of the diblocks thus can be characterized in different phases. In the isotropic phase, the MSA increases drastically in within 0.1 s, meaning the angular displacement varies quickly in a very short time. But in a long time

range, the angular displacement reaches a maximum of around 1.45 rad (83°), corresponding to the plateau of MSA at 2.1 rad^2 . In the nematic phase, the MSA also increase rapidly in short time and also reaches plateau afterwards, which is same as isotropic phase. But due to the confinement in nematic phase, the angle fluctuation is strongly suppressed. Therefore, the plateau of MSA (0.063 rad^2) in nematic is much lower than in isotropic phase. Correspondingly, a maximum angular displacement of about 0.25 rad (14.4°) is obtained in long time range.

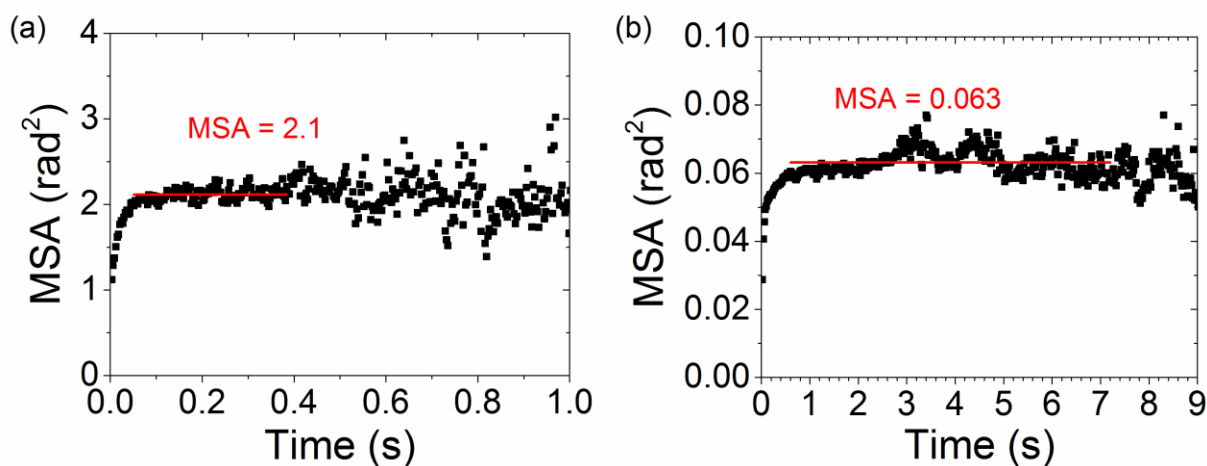


Figure 11: Mean square angular displacements (MSA) of diblocks in isotropic (a) and nematic (b) phases indicate the angle fluctuation between red and green blocks.

5.4 Conclusions

In this chapter, we present a method to synthesize heterobifunctional diblocks using M13C7C viruses as elementary building blocks. The specific position of cysteines (sulfurs) allows the regio-selective conjugation with AuNBs to form hybrid colloidal molecules. Thus, the heterobifunctional diblocks can be achieved by tip-linking two independently functionalized M13 viruses via one AuNB. As an example, M13 viruses are separately labelled with red or green fluorescent dyes and then self-assembled into bicolored diblocks. A final yield of about 50% M13 viruses associated in bicolored diblocks is obtained.

The fluorescent labeling allows for visualization of individual M13 virus by optical microscopy, which is extremely useful for the investigation of dynamics at the single particle level. Using this technique, we investigated dynamics of diblocks in different phases. In addition, each block of the bicolored diblocks can be analyzed separately due to the dual

labeling. Moreover, the influence of the flexible linking point between two blocks was discussed. The fluctuations of angle between the red and green blocks, which indicate the flexibility of the linking point, were characterized. The mean square angular displacement in isotropic and nematic phases were then analyzed and compared, which indicates a strong confinement of the angle fluctuation in the nematic phase.

5.5 References

- [1] C. Mao *et al.* Virus-Based Toolkit for the Directed Synthesis of Magnetic and Semiconducting Nanowires. *Science*, 2004, 303: 213–217.
- [2] Y. Huang *et al.* Programmable Assembly of Nanoarchitectures Using Genetically Engineered Viruses. *Nano Lett.*, 2005, 5: 1429–34.
- [3] Y. S. Nam *et al.* Virus-templated assembly of porphyrins into light-harvesting nanoantennae. *J. Am. Chem. Soc.*, 2010, 132: 1462–1463.
- [4] K. T. Nam *et al.* Virus-Enabled Synthesis and Assembly of Nanowires for Lithium Ion Battery Electrodes. *Science*, 2006, 312: 885–888.
- [5] D. Oh, J. Qi, Y. C. Lu, Y. Zhang, Y. Shao-Horn, and A. M. Belcher. Biologically enhanced cathode design for improved capacity and cycle life for lithium-oxygen batteries. *Nat. Commun.*, 2013, 4: 1–8.
- [6] D. Montalvan-Sorrosa, J. L. González-Solis, J. Mas-Oliva, and R. Castillo. Filamentous virus decoration with gold nanoparticles: global fingerprints of bionanocomposites acquired with SERS. *RSC Adv.*, 2014, 4: 57329–57336.
- [7] Z. Ruff *et al.* Designing disordered materials using DNA-coated colloids of bacteriophage fd and gold. *Faraday Discuss.*, 2016, 186: 473–488.
- [8] M. Moradi *et al.* Improving the capacity of sodium ion battery using a virus-templated nanostructured composite cathode. *Nano Lett.*, 2015, 15: 2917–2921.
- [9] S.-W. Lee, C. Mao, C. E. Flynn, and A. M. Belcher. Ordering of Quantum Dots Using Genetically Engineered Viruses. *Science*, 2002, 296: 892–895.
- [10] S. W. Lee, S. K. Lee, and A. M. Belcher. Virus-based alignment of inorganic, organic, and biological nanosized materials. *Adv. Mater.*, 2003, 15: 689–692.
- [11] S. R. Whaley, D. S. English, E. L. Hu, P. F. Barbara, and A. M. Belcher. Selection of peptides with semiconductor binding specificity for directed nanocrystal assembly. *Nature*, 2000, 405: 665–8.
- [12] J. Sambrook and W. D. Russell. *Molecular Cloning A Laboratory Manual*, 4th Ed. Cold Spring Harbor Laboratory Press: New-York, 2012.
- [13] Q. Wang *et al.* Chemical modification of M13 bacteriophage and its application in cancer cell imaging. *Bioconjug. Chem.*, 2010, 21: 1369–77.
- [14] L. A. Frances. Single particle dynamics in liquid crystalline phases formed by filamentous viruses. *Univ. Bordeaux*, 2017.
- [15] W. Andreoni, W. Andreoni, A. Curioni, A. Curioni, H. Grönbeck, and H. Grönbeck. Density

- functional theory approach to thiols and disulfides on gold: Au (111) surface and clusters. *Int. J. Quant. Chem.*, 2000, 80: 598–608.
- [16] H. Grönbeck, A. Curioni, and W. Andreoni. Thiols and disulfides on the Au(111) surface: The headgroup-gold interaction. *J. Am. Chem. Soc.*, 2000, 122: 3839–3842.
- [17] R. Bott. Fundamental Studies of the Chemisorption of Organosulfur Compounds on Au(111). Implications for Molecular Self-Assembly on Gold Surfaces. *J. Am. Chem. Soc.*, 1987, 109: 733–740.

Conclusion and perspectives

In this thesis, we focus on the self-assembly of colloidal molecules using rod-like viruses as building blocks. To achieve this purpose, we need to introduce linkers between virus tips. Therefore, two main strategies are proposed, using streptavidin—biotin interaction and metal—sulfur bond, respectively, to link together the proximal end of M13 viruses. Colloidal molecules are then assembled, whose valency (n , number of reacted viruses) can be controlled by specific experimental parameters.

The first method we used is based on the non-covalent streptavidin—biotin interaction. This interaction is one of the most frequently used strategies in bioconjugate techniques, due to its high affinity and specificity ($K_d \sim 10^{-15}$ M). In our case, we introduce biotin to the proximal tip of M13C7C viruses by chemical reaction and then link these tip-functionalized viruses with streptavidin coated nanoparticles. The key step for this method is the regio-selective grafting of biotin to the tip of M13C7C viruses, which is called biotinylation. Experimentally, it was achieved by reducing the exposed disulfide groups only present on p3 proteins (at the proximal tip), forming thiols, and then reacting with maleimide activated biotins. With an optimized biotinylation step, a highly efficient binding of streptavidin activated nanoparticles only to the proximal tip of viruses ($> 90\%$) is realized. As a comparison, the mutant M13-AS bacteriophages displaying Step-tag histidine-proline-glutamine (HPQ) at their proximal ends are also used to bind to streptavidin coated nanoparticles. The affinity of this Step-tag to streptavidin was experimentally determined, which shows a K_d of $6 (\pm 3) \times 10^{-6}$ M. Compared to this value, the K_d of streptavidin—biotin interaction is much smaller, indicating a much higher binding efficiency between biotinylated M13C7C viruses and streptavidin coated nanoparticles than M13-AS viruses. Therefore, the biotinylated M13C7C are more favorable for the self-assembly of colloidal molecules. A quantitative model of the self-assembly was then developed based on the reaction between modified viruses and streptavidin activated compounds, which accurately accounts for the assembly of colloidal molecules. Consequently, the colloidal molecules were created, whose valency can be solely tuned by the initial molar excess of the reactants.

The regio-selective chemical reaction between thiols and maleimide based compounds presented above can be extended to other functional groups or materials, like fluorescent dyes (as shown in Chapter 2), bound to the proximal end of M13 viruses. Thanks to these dyes, better contrast and resolution in smectic phase of these tip-labeled filamentous viruses are realized by fluorescence microscopy. An interesting perspective of this chemical reaction is to introduce patches to the proximal end of the viruses. For example, a thermo-responsive patch can be achieved by grafting poly(*N*-isopropylacrylamide) (PNIPAM) polymer. By increasing the temperature to more than the lower critical solution temperature (LCST), PNIPAM becomes hydrophobic, which results in a hydrophobic patch at the tip of viruses. Therefore, the directional attractive interaction induced by PNIPAM patch could be reversibly regulated by heating the suspension above or below LCST.

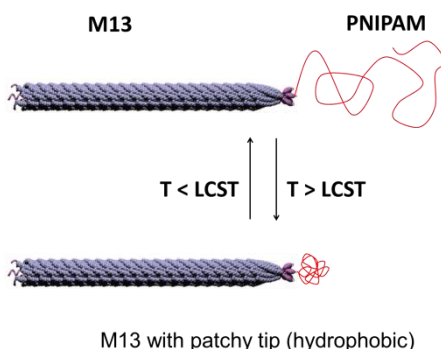


*Figure 1: The scheme of thermo-responsive an end-patchy M13 virus by grafting poly(*N*-isopropylacrylamide) (PNIPAM) polymer to the proximal end. The directional attractive interaction could be achieved by heating the suspension above lower critical solution temperature (LCST).*

Even though the self-assembly of colloidal molecules based on biotinylated M13 viruses is efficient, the whole process is complicated and intricate (reduction, biotinylation and assembly). Another drawback of this method is that the obtained colloidal molecules are not stable due to the aging and release of streptavidin from the surface of nanoparticles. Experimentally, we observed the decrease of the valency of colloidal molecules after a few weeks. Therefore, we established another more stable linker between virus tips in Chapter 3, by employing noble metal—sulfur reaction. The metal—sulfur bond is described as a weak covalent bond [1], [2] that is stronger than any non-covalent bond including streptavidin-biotin interaction. Moreover, the sulfurs already exist and are exposed at the proximal end of the viruses, so the self-assembly

of colloidal molecules can be realized in one simple step: mixing in suspension metallic nanoparticles and viruses. Experimentally, we explored the generic feature of this method by using different metallic nanoparticles (Au, Pt, Ag) and two strains of viruses (M13KE, M13C7C). Results show that the order of binding efficiency for nanoparticles is $\text{Au} > \text{Pt} > \text{Ag}$; for viruses is $\text{M13C7C} > \text{M13KE}$. We also investigated the influence of capping reagent of metallic nanoparticles (tannic acid and sodium citrate), ionic strength, molar excess and introduction of TCEP in self-assembly process. Specifically, tannic acid is a better stabilizer than sodium citrate, especially at high ionic strength; increasing ionic strength promotes the binding between metallic nanoparticles and viruses until metallic nanoparticles lose their stability; adding TCEP favors the binding between metal and viruses, because it breaks the disulfide bridge and makes the sulfur more exposed.

Here we point out that this method could also be applied to synthesize self-propelled (or active) particles when PtNPs are grafted to the tip of virus and hydrogen peroxide is used as fuel [3]–[5]. By extending this method, we can also introduce magnetic nanoparticles or quantum dots to one tip of M13 viruses. For example, the Au coated magnetic nanoparticles could be grafted to the proximal end of M13 viruses, then we would obtain AB type colloidal molecules with magneto-responsive tips. The dynamics of these hybrid particles could be driven by the external magnetic field. As a result, new phases, like polar smectic phase, could be formed (Figure 2).

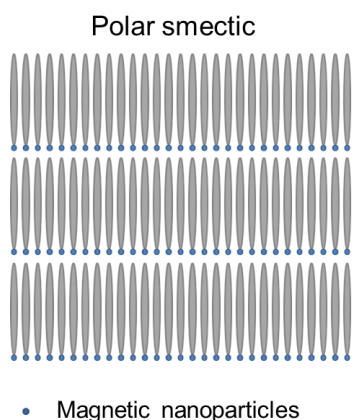


Figure 2: Scheme of a polar smectic phase, composed of filamentous viruses with magnetic nanoparticles at one end.

On the other hand, we found that it is also possible to graft the metallic nanoparticles at the distal end of M13 viruses, even though this binding has not yet been controlled so far. Actually, preliminary experiments have shown that increasing the virus concentration to the dense phase (smectic) could improve the binding of metallic nanoparticles on distal ends. As a future project, we could also use genetic modification on p9 or p7 proteins to display sulfur on the distal end, in order to bind metallic nanoparticles at this end conveniently and efficiently. With metallic nanoparticles as linkers at both ends of the viruses, we can assemble the viruses into linear colloidal polymers (Figure 3a). In addition, when two different reactive groups are introduced to two ends, respectively, we could achieve hetero-bifunctionalization of the viruses. For example, with unnatural amino acid selenocysteine (selenium) displayed on one end of the viruses and cysteine (sulfur) on the other end, we may realize the binding of two different metallic nanoparticles to two ends, respectively (Figure 3b), by varying the pH (cysteine $pK_a = 8.1$; selenocysteine $pK_a = 5.2$).

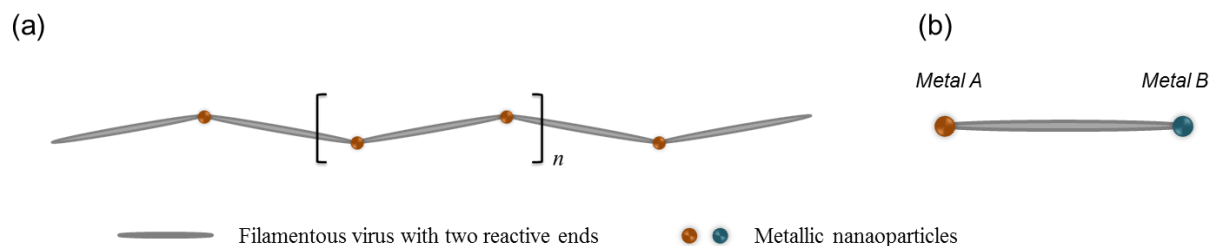


Figure 3: Scheme of (a) virus based linear colloidal polymers and (b) hetero-bifunctionalized viruses. The linear colloidal polymers could be achieved by display cysteine (sulfur) on the distal end of the viruses and binding with metallic nanoparticles; with selenocysteine (selenium) displayed on one end of the viruses and cysteine (sulfur) on the other end, hetero-bifunctionalized viruses with two different metallic nanoparticles at two ends could be realized.

Following the simple metal—sulfur interaction method that has been established in Chapter 3, we then applied it in the self-assembly of virus based colloidal molecules with tunable valency. The optimal system, which uses tannic acid capped AuNBs and M13C7C viruses as building blocks, is chosen for this purpose. The diameter of nanoparticles and ionic strength are two parameters that tune the valency of the assembled colloidal molecules (under the condition of a high initial molar excess of viruses). Therefore, we built a quantitative model using diameter of AuNBs and ionic strength as variables. In this model, the viruses are considered as

cylindrical rods that can bind to the surface of spherical AuNBs with their ends. Therefore, the valency, n (i.e., the number of viruses reacted on the surface of AuNB), is determined by the ratio of the surface area of AuNB (through the diameter) over the effective diameter of M13 virus (through the ionic strength). This model was then employed to produce colloidal molecules of desired valency in large scale. Since the valency of obtained colloidal molecules always shows a distribution, and the yield of the produced structures of a fixed valency decreases with increasing the valency, we choose to produce the simplest multivalent colloidal molecules, i.e., AB_2 types. The experimental average valency ($\langle n \rangle = 1.62$) shows a good consistence with the model (the theoretical prediction is $\langle n \rangle = 1.42$) within the error bar. In order to improve the reaction between AuNBs and M13C7C viruses, and reach average valency $\langle n \rangle = 2$, TCEP (2 mM) was added. As a result, an average valency of virus based colloidal molecules of $\langle n \rangle = 2$ was achieved, with a yield of 57% AB_2 types. In total, we produced about 6 mg of AB_2 type colloidal molecules, enabling the investigation of their properties in the bulk phase, including dynamics and phase transitions.

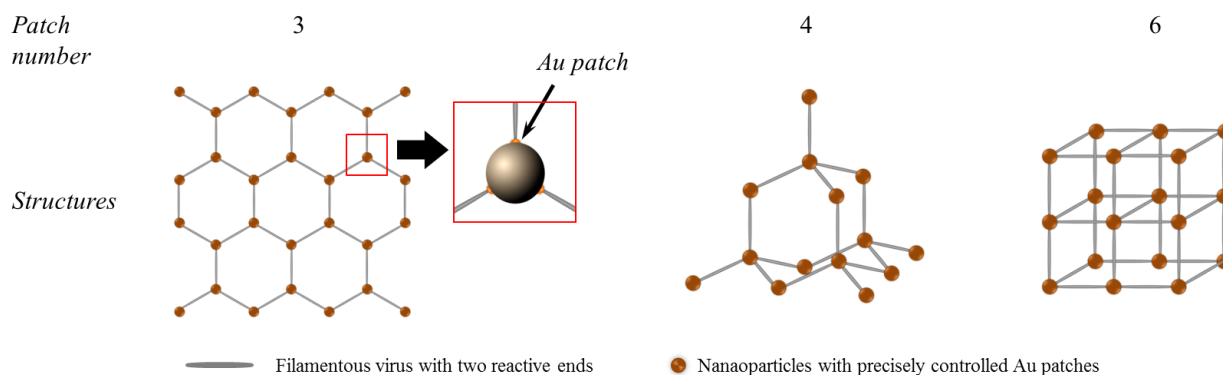


Figure 4: The Schematic representations of structures composed of nanoparticles with precisely controlled Au patches and two-ends-reactive filamentous viruses. With different number of patches, different symmetries could be formed.

However, with increasing the valency, the selectivity for a colloidal molecules of given valency decreases. To improve the selectivity, a promising method is to use nanoparticles with fixed number of small gold patches. When the gold patch is small enough (< 5 nm), only one viruses is able to react to one patch. In this way, we could precisely control the valency of obtained colloidal molecules. Furthermore, combined with the possible grafting on distal end of

the viruses, we could create two or three dimensional hybrid structures with different symmetries (Figure 4). In this case, the nanoparticles and viruses could serve as units for the colloidal ball-and-stick model in the micro-scale.

As the last part of the thesis, we further develop the sulfur—metal interaction to assemble heterobifunctional diblocks using M13 viruses as building blocks. The idea is to graft two different functionalities on the body of M13 viruses, respectively, and then linking them via an AuNB. Meanwhile, a flexible linking point between two viral blocks is realized due to the flexibility of p3 proteins. As a proof-of-concept experiment, we succeeded in synthesis of bicolored diblocks. This bicolored diblocks are a new generation of hybrid colloidal particles that could be used for different purposes in soft matter. For example, the dynamics of virus based diblocks in the isotropic and nematic phases were studied by mixing tracer amount of these particles in a matrix of non-labeled viruses. Especially, the influence of the flexible linking point between two blocks was discussed. Specifically, the diffusion coefficient of the bicolored diblocks was determined, which is about half smaller than single viruses. Also, the fluctuations of angle between the red and green blocks, which determines the flexibility of the linking point, were characterized. The mean square angles in isotropic and nematic phases were then analyzed and compared, which indicates a strong confinement of the angle fluctuation in the nematic phase.

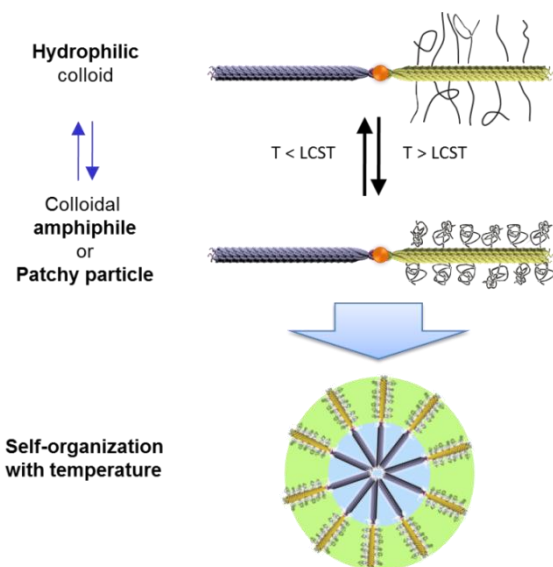


Figure 5: Schematic representation of the thermo-responsive amphiphilic diblocks and their self-organization into micelles.

Another possible example of heterobifunctional diblocks could be amphiphilic diblocks. One simple way to achieve this goal is to graft one block with PNIPAM (hydrophobic when temperature is above LCST), as shown in the scheme in Figure 5. Knowing that the viruses themselves are hydrophilic, amphiphilic diblocks could be obtained by linking the PNIPAM grafted viruses with non-grafted ones. Investigations of the amphiphilic diblock self-organization in suspension are of great interest, since they could be used for revisiting amphiphilic liquid crystal science at the colloidal scale. For example, these amphiphilic diblocks could organize into bilayered or micellar structures by changing temperature and varying polymer molar weight. When the concentration of amphiphilic diblocks increases to high value, liquid crystalline phases could form.

References

- [1] P. Kohli, K. K. Taylor, J. J. Harris, and G. J. Blanchard. Assembly of covalently-coupled disulfide multilayers on gold. *J. Am. Chem. Soc.*, 1998, 120: 11962–11968.
- [2] Y. Xue, X. Li, H. Li, and W. Zhang. Quantifying thiol-gold interactions towards the efficient strength control. *Nat. Commun.*, 2014, 5: 4348.
- [3] W. Wang, W. Duan, S. Ahmed, A. Sen, and T. E. Mallouk. From one to many: Dynamic assembly and collective behavior of self-propelled colloidal motors. *Acc. Chem. Res.*, 2015, 48: 1938–1946.
- [4] S. Sanchez, L. Soler, and J. Katuri. Chemically powered micro- and nanomotors. *Angew. Chem. Int. Ed.*, 2015, 54: 1414–1444.
- [5] W. F. Paxton, P. T. Baker, T. R. Kline, Y. Wang, T. E. Mallouk, and A. Sen. Catalytically induced electrokinetics for motors and micropumps. *J. Am. Chem. Soc.*, 2006, 128: 14881–14888.

Appendix I

Charge properties of proteins of fd, M13 and M13C7C

Bacteriophage fd/M13 particles are 7 nm in diameter and about 1 μm in length. The viral particle is composed of a single-stranded circular DNA molecule that is encapsulated in a long cylindrical protein coat. The protein coat is composed of about 3000 copies of the major coat protein (p8). At both termini there are five copies of each of the two minor coat proteins, p3 and p6 at one end (proximal end) and p7 and p9 at the other end (distal end), as shown below:

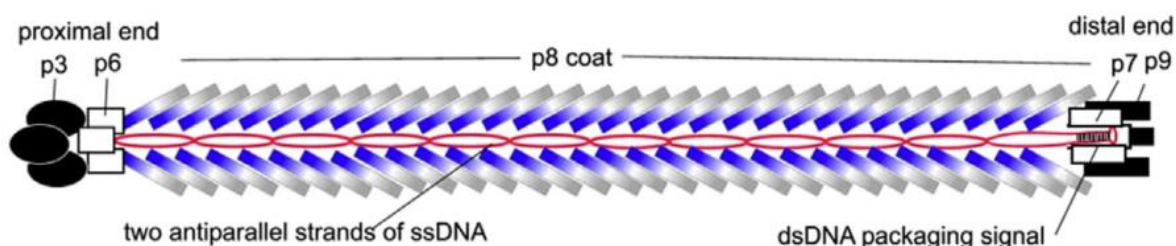


Figure 1: Schematic illustration of a bacteriophage fd/M13 [1].

Because of the specific feature of p3 protein, chemical or physical modifications can be performed selectively on it. For example, p3 proteins possess cysteines that form disulfide bridges at their N-terminals. These disulfides are the only exposed ones on the viruses, which can be used for regio-selective functionalization, like reacting with maleimide activated compounds, on virus proximal end. Likewise, charge properties of these proteins can also be used for modification when electrostatic interaction is introduced. Therefore, in this appendix, we focus on the theoretical study on charge properties of fd/M13 viruses which depend on the constructed amino acids and pH of the suspension. According to Endemann [2], p6 and p7 proteins are buried and shielded from the environment, so we only focus the charge proteins of p8 protein, p3 protein and p9 protein. Two methods are used to determine the overall charge number and isoelectric point (pI) of these proteins.

Method 1: use the calculator provided by *GenScript* [3], which only gives the results at physiological pH (7.4).

Method 2: calculate by hand the summary of total charge of each protein at different pH (All the hand calculated resulted are summarized in tables).

In the following sections, charge properties of each protein are calculated by these two ways.

A. Charge properties of protein p8

Both fd and M13 viruses have 50 amino acids on p8 protein, the only difference between them is the 12th amino acid, as following:

<i>fd wt:</i>	H₂N-<u>AEGDDPA</u> <u>KA</u>A<u>F</u>DSLQAS	ATE YIGYAWA	MVVVIVGATI	GIKLF	KKFTS	KAS (OEt)
<i>M13:</i>	H₂N-<u>AEGDDPA</u> <u>KA</u>A<u>F</u>DSLQAS	ATE YIGYAWA	MVVVIVGATI	GIKLF	KKFTS	KAS (OEt)

Red: acidic residues; Blue: basic residues; Bold: exposed amino acids

Figure 2: Amino acids of P8 protein for fdwt and M13 viruses. The only difference in amino acid is indicated in red rectangular. The red acidic residues and blue basic residues exhibit negative and positive charges, respectively, at physiological pH.

However, only the first 20 first amino acids (**in bold**, Figure 2) of the p8 protein are exposed to the solvent according to Marvin's paper [4]. So we only take into account the first 20 amino acids when calculating the overall charge number. Specific calculations are shown as:

Method 1

Note that, when calculating the overall charges, GenScript doesn't count the terminal charges, only side chain are taken into account. And pKa of the amino acid used by GenScript is the value in H₂O which actually differs depending on the environment.

Fdwt: Total charges -4 at pH 7.4; Isoelectric point 3.8

M13: Total charges -3 at pH 7.4; Isoelectric point 4.0

Method 2

Charged amino acids in p8 protein are summarized as:

fdwt: H₂N-AEDDKDE(OEt)
M13: H₂N-AEDDKKE(OEt)
Red: acidic residues, *Blue*: basic residues

Figure 3: Charged amino acids of P8 protein exposed to the solvent for *fdwt* and *M13* viruses which is extracted from Figure 2. The red acidic residues and blue basic residues exhibit negative and positive charges, respectively, at physiological pH.

Number and pKa [5] of charged amino acid in p8 protein of *fdwt* and *M13* are summarized in the following Table 1 and Table 2. Also the overall charge numbers of p8 protein are calculated.

So, pI of p8 protein of *fdwt* is between pH 3.5 and 4.5, charge number at physiological pH is -3; pI of p8 protein of *M13* is pH 4.5, charge number at physiological pH is -2. This results is consistent with Zimmerman's paper [5], as the pI of fd virus (mainly consisting of p8 protein) is reported to be 4.2.

We find that there is one charge difference between the charge number calculated by method 1 and method 2. The reason is that the charge of terminal amine (+1 at pH 7.4) for Alanine is not calculated by the software of GenScript.

Table 1: Calculation of charge properties for p8 protein of *fdwt*.

	pKa	Number	Charge properties at different pH				
			pH < 3.5	3.5 < pH < 4.5	4.5 < pH < 5.5	5.5 < pH < 8	Physiological pH 7.4
NH ₂ -terminal	7.9	1	+1	+1	+1	(+1) to (+0.5)	+1
Lys(K)	10.1	1	+1	+1	+1	+1	+1
Glu(E)	4.5	2	0	0 to (-0.5)	(-0.5) to (-1)	-1	-1
Asp(D)	4.5	3	0	0 to (-0.5)	(-0.5) to (-1)	-1	-1
Total Charges			+2	(+2) to (-0.5)	(-0.5) to (-3)	(-3) to (-3.5)	-3

Table 2: Calculation of charge properties for p8 protein of M13.

	pKa	Number	Charge properties at different pH				
			pH < 3.5	3.5 < pH < 4.5	4.5 < pH < 5.5	5.5 < pH < 8	Physiological pH 7.4
NH ₂ -terminal	7.9	1	+1	+1	+1	(+1) to (+0.5)	+1
Lys(K)	10.1	1	+1	+1	+1	+1	+1
Glu(E)	4.5	2	0	0 to (-0.5)	(-0.5) to (-1)	-1	-1
Asp(D)	4.5	2	0	0 to (-0.5)	(-0.5) to (-1)	-1	-1
Total Charges			+2	(+2) to (0)	(0) to (-2)	(-2) to (-2.5)	-2

B. Charge properties of protein p3

Amino acids of the whole p3 protein for fdwt and M13 are the same. As for M13C7C, a peptide is fused at the end of N-terminal, as the italic part in bracket shown in Figure 4:

<i>fdwt/M13</i> : H ₂ N-AE				
<i>M13C7C</i> : H ₂ N-A<CDPVREATCGGG>E				
TVESCLAKPH	TENSFTNVWK	DDKTLDRYAN	YEGCLWNATG	VVVCTGDETQ
CYGTWVPIGL	AIPENE GGGS	EGGGSE GGGS	EGGGTKPPEY	GDTPIPGYTY INPLDGTYP
GTEQNPANPN	PSLEESQPLN	TFMFQNNRFR	NRQGALTVYT	GTVTQGTDPV
KTYQYTPVS	SKAMYDAYWN	GKFRDCAFHS	GFNE DPFVCE	YQGQSSDLPQ
PPVNAGGGSG	GGSGGGSEGG	GSEGGGSEGG	GSEGGGSGGG	S(GSGDFDYEK
MANANKGAMT	ENADENALQS	DAKGKLDVA	TDYGAAIDGF	IGDVSGLANG
NGATGDFAGS	NSQMAQVGDG	DNSPLMNNFR	QYLPSPQSV	ECRPYVFGAG
KPYEFSIDCD	KINLFRGVFA	FLLYVATFMY	VFSTFANILR	NKES)
<i>Red: acidic residues; Blue: basic residues; Bold: exposed amino acids</i>				

Figure 4: Amino acids of P8 protein for fdwt/M13 and M13C7C viruses. P8 protein is identical for fdwt and M13. In contrast, M13C7C has a fused peptide at N-terminal. Exposed amino acids are indicated in bold. The red acidic residues and blue basic residues exhibit negative and positive charges, respectively, at physiological pH.

According to Marvin's paper [4], the first 253 amino acids (**in bold**, Figure 4) of the p3 protein are exposed to the solvent, which are used for calculating the isoelectric point and overall charge number. Charged amino acids are extracted and shown as follows:

fdwt/M13: H₂N-A**EEKHEKDDKDREDEEEEEEEKEDDEEERRRDKKDKRDHEDEDEEEE** (OEt)
M13C7C: H₂N-A<DRE>**EEKHEKDDKDREDEEEEEEEKEDDEEERRRDKKDKRDHEDEDEEEE** (OEt)
Red: acidic residues, Blue: basic residues

Figure 5: Charged amino acids of P3 protein for fdwt/M13 and M13C7C viruses, which is extracted from Figure 4. The red acidic residues and blue basic residues exhibit negative and positive charges, respectively, at physiological pH.

Method 1

For fdwt/M13, charged amino acids are extracted and shown as follows:

Total charges: -17 at pH 7.4; Isoelectric point: 4.00

For M13C7C, we have inserted amino acids <CDPV**RE**ATCGGG> at N-terminal of p3 protein, thus overall charge is changed:

Total charges: -18 at pH 7.4; Isoelectric point: 4.00

Method 2

Calculations of the overall charges and pI are summarized in Table 3 and Table 4.

Table 3: Calculation of charge properties for p3 protein of fdwt and M13.

	pKa	Number	Charge properties at different pH				
			pH < 3.5	3.5 < pH < 4.5	4.5 < pH < 5.5	5.5 < pH < 8	Physiological pH 7.4
NH ₂ -terminal	7.9	1	+1	+1	+1	(+1) to (+0.5)	+1
Arg(R)	12	6	+1	+1	+1	+1	+1
Lys(K)	10.1	7	+1	+1	+1	+1	+1
His(H)	6.0	2	+1	+1	(+1) to (+0.5)	(+0.5) to 0	0
Glu(E)	4.5	20	0	0 to (-0.5)	(-0.5) to (-1)	-1	-1
Asp(D)	4.5	11	0	0 to (-0.5)	(-0.5) to (-1)	-1	-1
Total Charges			+16	(+16) to (+0.5)	(+0.5) to (-16)	(-16) to (-17.5)	-17

Table 4: Calculation of charge properties for p3 protein of M13C7C.

	pKa	Number	Charge properties at different pH				
			pH < 3.5	3.5 < pH < 4.5	4.5 < pH < 5.5	5.5 < pH < 8	Physiological pH 7.4
NH ₂ -terminal	7.9	1	+1	+1	+1	(+1) to (+0.5)	+1
Arg(R)	12	6	+1	+1	+1	+1	+1
Lys(K)	10.1	7	+1	+1	+1	+1	+1
His(H)	6.0	2	+1	+1	(+1) to (+0.5)	(+0.5) to 0	0
Glu(E)	4.5	21	0	0 to (-0.5)	(-0.5) to (-1)	-1	-1
Asp(D)	4.5	12	0	0 to (-0.5)	(-0.5) to (-1)	-1	-1
Total Charges			+16	(+16) to (-0.5)	(-0.5) to (-18)	(-18) to (-19.5)	-19

So, according to Table 3, pI of p3 protein for fd and M13 viruses is between pH 4.5 and 5.5, and the charge number at pH 7.4 is -17. For M13C7C, the inserted amino acids have same influence on the charge number and pI, shifting pI to pH between 3.5 to 4.5 and overall charge number to -19.

C. Charge properties of protein p9

Amino acids of the whole p9 protein are shown as:



Figure 6: Amino acids of p9 protein. The red acidic residues and blue basic residues exhibit negative and positive charges, respectively, at physiological pH.

Endemann et al. [2] reported that the p9 proteins is exposed to the environment, but it is still unclear that exact which part of the protein is exposed. Thus, we calculated the charge properties of p9 protein under two different assumptions.

First, we assume all the amino acids are exposed to solvent, the charge properties for p9 protein are calculated as follows:

Method 1

Total charges: ± 1 at pH 7.4; Isoelectric point: 8.51.

Method 2

Number and pKa of charged amino acid in p9 protein of M13C7C virus are summarized in the following Table 5, where the number of charges is also calculated.

So, pI of p9 protein should be between pH 9 and 11. Charge number at pH 7.4 is +1. Calculation between software and hand counting is consistent.

Table 5: Calculation of charge properties for p9 protein.

	pKa	Number	Charge properties at different pH				
			3.4 < pH < 4.5	4.5 < pH < 7	7 < pH < 9	9 < pH < 11	Physiological pH 7.4
NH ₂ -terminal	7.9	1	+1	+1	(+1) to 0	0	+1
Arg(R)	12	2	+1	+1	+1	+1	+1
Glu(E)	4.5	1	0 to (-0.5)	(-0.5) to (-1)	-1	-1	-1
COOH-terminal	3.4	1	-0.5 to (-1)	-1	-1	-1	-1
Total Charges			(+2.5) to (+1.5)	(+1.5) to (+1)	(+1) to 0	0	+1

Nevertheless, according to Marvin's paper, the N-terminal portion of p9 protein is hydrophobic [4]. So most part of the p9 protein is probably not exposed to the solvent (water). Therefore, we assume another condition that only the terminal -NH₂ (of methionine) is exposed, which gives +0.5 charge at physiological pH 7.4. No pI exists for p9 protein in this case.

References

- [1] D. A. Marvin, M. F. Symmons, and S. K. Straus. Structure and assembly of filamentous bacteriophages. *Prog. Biophys. Mol. Biol.*, 2014, 114: 80–122.
- [2] H. Endemann and P. Model. Location of filamentous phage minor coat proteins in phage and in infected cells. *J. Mol. Biol.*, 1995, 250: 496–506.
- [3] Peptide Property Calculator. , <https://www.genscript.com/tools/peptide-property-calculator>.
- [4] D. Marvin. Filamentous phage structure, infection and assembly. *Curr. Opin. Struct. Biol.*, 1998, 8: 150–158.

- [5] K. Zimmermann, H. Hagedorn, C. C. Heuck, M. Hirichsen, and H. Ludwig. The ionic properties of the filamentous bacteriophages Pf1 and *\textit{fd}*. *J. Bio. Chem.*, 1986, 261: 1653–1655.

Appendix II

Calculation of sedimentation coefficient of sphere and rod particles to determine centrifugation acceleration

Symbols in the calculations refer to

v_t ($\text{m}\cdot\text{s}^{-1}$): terminal velocity of the particle;

a ($\text{m}\cdot\text{s}^{-2}$): applied acceleration;

m (kg): mass of the nanoparticle or colloidal structure;

S (s): sedimentation coefficient;

l (m): length of centrifugation tube;

t (s): centrifugation duration;

ρ_N (kg/m^3): density of spherical nanoparticles, Au: 19.4×10^3 kg/m^3 , Pt: 21.45×10^3 kg/m^3 ;

ρ_s (kg/m^3): density of the solvent, 1.0×10^3 kg/m^3 for water ;

D (m): diameter of a spherical nanoparticle;

η (P·s): dynamic viscosity of the solution, 0.001 Pa·s for water;

L (m): rod length, 1 μm for M13C7C;

d (m): diameter of the rod, 7 nm for M13C7C;

V_N (m^3): volume of a spherical nanoparticle;

V_M (m^3): volume of a M13C7C virus;

ρ_M (kg/m^3): density a of M13C7C virus, 1.285×10^3 kg/m^3 [1].

Centrifugation is one of the most widely used methods for separation, purification, and concentration. In this thesis, centrifugations are used for different steps, including concentrating viruses, removing free nanoparticles (Au or Pt). For these purposes, different accelerations have to be applied. Thus the aim of this appendix is to determine the expected acceleration by theoretical prediction.

During the centrifugation step, particles reach terminal velocity v_t in a very short time (compare to the centrifugation time), and this velocity is given by

$$v_t = S \cdot a \quad (1)$$

where, a is the applied acceleration; S is the sedimentation coefficient, an inherent property of a particle in a suspension.

By the time centrifugation was finished, particles at the top move through the height of the suspension (l) during a time t , therefore, we have

$$l = v_t \cdot t = S \cdot a \cdot t,$$

Thus, expression for acceleration is

$$a = \frac{l}{S \cdot t} \quad (2)$$

So, to determine the necessary experimental accelerations, and as for the suspension height and time (for practical reasons, about 1 hour for structure with Au or Pt nanoparticles and 3 hours for bare viruses) are experimentally fixed, **the main task is to calculate sedimentation coefficient of the particle suspension.**

As mentioned, sedimentation coefficient, S , is an inherent property of a particle in a suspension. For infinite dilute aqueous dispersion, S depends only on the density and shape of particles.

In this thesis, our system consists of rod shaped viruses and spherical nanoparticles, so we focus on the calculation of rod and spherical particles.

A. Spherical particles

When centrifugation is performed on a spherical particle, there is a centrifugal force and a drag force acting on it (gravity of the particle is negligible compare to others).

The centrifugal force is described as

$$F_c = m \cdot a - \rho_s \cdot V_M \cdot a = (m - \rho_s \cdot V_N) \cdot a \quad (3)$$

$$= (\rho_N - \rho_s) \cdot V_N \cdot a = \frac{\pi(\rho_N - \rho_s)D^3}{6} \cdot a \quad (4)$$

Meanwhile, the drag force on a spherical particle is described as

$$F_D = 3\pi\eta D \cdot v_t = 3\pi\eta D \cdot S \cdot a \quad (5)$$

After short time, when a nanoparticle reaches its terminal velocity, the total forces on the particle are equilibrated, which means $F_c = F_D$, that is

$$\frac{\pi(\rho_N - \rho_s)D^3}{6} \cdot a = 3\pi\eta D \cdot S \cdot a,$$

from which we could deduce the sedimentation coefficient to be

$$S = \frac{m - \rho_s \cdot V_N}{3\pi\eta D} = \frac{(\rho_N - \rho_s)}{18\eta} \cdot D^2 \quad (6)$$

For an aqueous suspension of $D = 11\text{nm}$ Au nanoparticles ($\rho_N = 19.4 \times 10^3 \text{ kg/m}^3$, $\eta = 0.001 \text{ Pa}\cdot\text{s}$, $\rho_s = 1.0 \times 10^3 \text{ kg/m}^3$), using Equation (6), sedimentation coefficient is calculated to be $S = 1.24 \times 10^{-10} \text{ s}$. The acceleration needed to sediment these Au nanospheres in an ultracentrifuge tube (8 cm) in 90 mins duration is calculated using Equation (2), $a = 12 \text{ k}\times\text{g}$. Experimentally, the centrifugations were done at $10 \text{ k}\times\text{g}$ for 45 min 3 time and then $15 \text{ k}\times\text{g}$ for 45 min 2 times, until the supernatant contained less than 10% of free Au nanospheres, which was checked by transmission electron microscope.

B. Rod shaped particles

The terminal velocity of a rod-like particle during sedimentation (by gravity or centrifugation) has been described by Dogic et al. [1], which is

$$v_t = \frac{\ln\left(\frac{L}{d}\right)}{3\pi\eta L} \cdot F^{ext} \quad (7)$$

where, F^{ext} is the external force applied on the rod particles, in this case, centrifugation force F_c .

As mentioned in his paper, the second term in the bracket vanishes relative to the first term for very long rods [1], which could be applied to M13 viruses (it has aspect ratio $L/d = 1 \mu\text{m} / 7 \text{ nm} = 143$). Additionally, during the centrifugation process, the external force is the centrifugal force (see Equation (3)),



Scheme 1: Rod with length L and diameter d .

Substituting Equation (7) with Equation (1) and (3), gives

$$S = \frac{v_t}{a} = \frac{\ln\left(\frac{L}{d}\right)}{3\pi\eta L} \cdot (m - \rho_s \cdot V_M) \quad (8)$$

$$= \frac{\ln\left(\frac{L}{d}\right)}{3\pi\eta L} \cdot \frac{\pi(\rho_M - \rho_S)d^2L}{4} \quad (9)$$

For an aqueous suspension of M13C7C viruses, the parameters of the system are: length $L = 1 \mu\text{m}$, diameter $d = 7 \text{ nm}$, density of M13C7C viruses $\rho_M = 1.285 \times 10^3 \text{ kg/m}^3$, density of solvent (water) $\rho_S = 1 \times 10^3 \text{ kg/m}^3$, dynamic viscosity of the solvent η (water) = $0.001 \text{ Pa}\cdot\text{s}$.

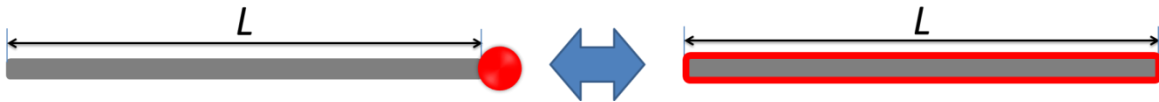
Using Equation (9), the sedimentation coefficient of M13 viruses is calculated to be $S = 5.2 \times 10^{-12} \text{ s}$.

Acceleration needed to sediment these viruses in an ultracentrifuge tube (8 cm) in 3 hours is calculated using Equation (2), $a = 145 \text{ k}\times\text{g}$.

Experimentally, the ultracentrifuge can run at acceleration up to $250 \text{ k}\times\text{g}$. In order to make sure we collect as many viruses as we can, when we concentrate the M13 viruses from a dilute state, acceleration of $250 \text{ k}\times\text{g}$ is applied.

C. Scepter-like particles

There is no model in the current literature to calculate the sedimentation coefficient of this scepter-like rod-sphere particle, thus we did an approximation by assuming the Au nanosphere at the tip of rod spreads homogenously on the surface of rod, and the resulted coated rod keeps the same length as original one, as shown below:



Scheme 2: Scepter-like virus-AuNB structure and virus covered homogenously by Au layer. We assume these two structures have the same sedimentation coefficients when the Au mass is equal.

In this case, we assume the Scepter-like particle as a rod with the AuNB homogenously spreads in the surface of viruses, then, Equation (8) could be applied to calculate the sedimentation coefficient.

So the approximated coated rod has the same volume and mass as the Scepter-like Rod-sphere particle, which are:

$$\text{Volume of the colloidal complex is } V = V_N + V_M = \frac{\pi D^3}{6} + \frac{\pi L d^2}{4}$$

$$\text{Mass is } m = \frac{\pi D^3}{6} \rho_N + \frac{\pi L d^2}{4} \rho_M$$

Therefore, the effective diameter of the approximated rod is calculated as:

$$d_{\text{eff}} = \sqrt{\frac{4V}{\pi L}} = \sqrt{\frac{D^3}{3L} + d^2}$$

By substituting mass, volume and diameter of rod in Equation (8) with the mass, volume and effective diameter of the Scepter-like AB type structure, the sedimentation coefficient is rewritten as

$$\begin{aligned} S &= \frac{\ln\left(\frac{L}{\sqrt{\frac{D^3}{3L} + d^2}}\right)}{3\pi\eta L} \cdot \left[\left(\frac{\pi D^3}{6} \rho_N + \frac{\pi L d^2}{4} \rho_M\right) - \rho_s \cdot \left(\frac{\pi D^3}{6} + \frac{\pi L d^2}{4}\right) \right] \\ &= \frac{\ln\frac{3L^3}{D^3 + 3Ld^2}}{6\pi\eta L} \cdot \left[\frac{\pi D^3}{6} (\rho_N - \rho_s) + \frac{\pi L d^2}{4} (\rho_M - \rho_s) \right] \end{aligned} \quad (10)$$

When Equation (10) is applied for the AB type colloidal molecule—one Au nanobead of diameter 11 nm bound at the end of M13 viruse, the corresponding sedimentation coefficient is $S = 1.20 \times 10^{-11}$ s.

Comparing to the sedimentation coefficient of a rare virus, which is 5.2×10^{-12} s, the scepter-like AB type has a twice higher coefficient. If we apply the same time and suspension height for centrifuging AB type colloidal molecules as raw viruses (3 hours, 8 cm), the acceleration needed is 63 k×g. However, long time centrifugation could cause the aggregation of AuNBs, short time is thus preferable. Experimentally, we choose centrifugation time 1 hour. In this case, the acceleration needed to fully sediment these AB types in an ultracentrifuge tube (8 cm) is calculated using Equation (2), $a = 190$ k×g.

Experimentally, 250 k×g centrifugation for 1 hour is performed to make sure we collect all the AB type colloidal molecules.

Lastly, we summary all the calculated theoretical conditions and experimental conditions we applied in Table 1.

Appendix II: Calculation of sedimentation coefficient of sphere and rod particles to determine centrifugation acceleration

Table 1: Summary of calculated and applied centrifugation conditions for a suspension of height 8 cm.

Objects	Sedimentation coefficient (s)	Theoretical	Experimental
		Time \times acceleration	Time \times acceleration \times rounds
M13 viruses	5.19×10^{-12}	145 k \times g \times 3 hours	250 k \times g \times 3 hours \times 1
11 nm AuNB	1.25×10^{-10}	12 k \times g \times 90 min	12 k \times g \times 45 min \times 5
M13-AuNB (11 nm)	1.22×10^{-11}	190 k \times g \times 1 hour	250 k \times g \times 1 hour
30 nm PtNP	1.01×10^{-9}	2.2 k \times g \times 1 hour	800 g \times 30 min \times 5

References

- [1] Z. Dogic, A. P. Philipse, S. Fraden, and J. K. G. Dhont. Concentration-dependent sedimentation of colloidal rods. *J. Chem. Phys.*, 2000, 113: 8368–8380.